General Disclaimer

One or more of the Following Statements may affect this Document

Final Report
Contract No. NAS 9-7030

DETAILED ANALYSIS OF RADIATION DATA FROM
THE GEMINI IV AND GEMINI VII PROTON-
ELECTRON SPECTROMETER EXPERIMENTS

by

J. B. Reagan
M. A. Heinemann *
J. C. Bakke
W. L. Imhof

. * Presently at the
Massachusetts Institute of Technology

30 December 1968

FOREWORD

This final report is submitted to the National Aeronautics and Space Administration, Manned Spacecraft Center, covering work performed under Contract NAS 9-7030, Detailed Analysis of Radiation Data from the Gemini IV and Gemini VII Proton-Electron Spectrometer Experiments.

The work was performed during the period 13 June 1967 to 30 December 1968 at the Lockheed Palo Alto Research Laboratory, Palo Alto, California

ABSTRACT

This report describes the results of the data analysis performed on information obtained from two radiation spectrometer experiments conducted on the Gemini IV and Gemini VII spacecraft in June and December 1965, respectively. Omnidirectional fluxes and spectra of electrons in the 0.45-6.0 MeV energy range and of protons in the 23.5-80 MeV energy range as well as the omnidirectional proton flux greater than approximately 64 MeV were measured by scintillation spectrometers employing 16-channel pulse-height analyzers. Omnidirectional fluxes of both electrons and protons as a function of the magnetic field intensity, B, for specific L shells are presented along with the resulting flux contours in B,L space. Detailed electron and proton spectra as a function of L shell are also presented. Comparison of the present results with both theoretical and other experimental results is included. A direct measurement of the flux and spectra of the East-West asymmetry of trapped protons at low altitudes was performed on the Gemini IV experiment. A discussion of this measurement and its implications on the source and decay of trapped protons in the inner radiation belt is also presented.

ACKNOWLEDGMENTS

TABLE OF CONTENTS

Section I

INTRODUCTION

Two experiments designed by the Space Radiation Group of the Lockheed Palo Alto Research Laboratory were conducted aboard Gemini Spacecraft to measure in detail the proton and electron environment. The flux and spectrum of electrons in the 0.45-6.0 MeV energy range and of protons in the 23.5-80 MeV energy range and the omnidirectional proton flux greater than 64 MeV were measured aboard the Gemini IV spacecraft from 3-7 June 1965 with a scintillation spectrometer employing a 16-channel pulse-height analyzer. From 4-18 December 1965, a similar experiment with somewhat different energy ranges was performed on the Gemini VII spacecraft.

These experiments have provided detailed flux and spectrum measurements in the vicinity of the South Atlantic anomaly, where the population, lifetime, and behavior of particles trapped on low magnetic shells are greatly influenced by the earth's atmosphere. Therefore, it is possible to study loss and redistribution mechanisms as well as the overall time variations encountered in the inner radiation belt by means of detailed comparisons between experimental data and atmospheric scattering theory. Previous comparisons of this sort have been limited by the number of detailed experimental measurements (Imhof et al., 1963; Mann et al., 1963; Mozer et al., 1963; Freden and Paulikas, 1964; Imhof and Smith, 1965a,b,c,d; West et al., 1965; Chapman and Farley, 1968). Data acquired from higher altitude satellites are not so directly applicable to the understanding of phenomena in this low-altitude region. Indeed, studies of this low-altitude region have provided many unique opportunities to study phenomena of importance throughout the radiation belts. Since the available data are limited and because the behavior of the trapped radiation is time dependent, frequent updating of the lower inner radiation belt model is required. Experiments performed periodically on low-altitude spacecraft have provided our best source of such information.

Our knowledge of the origin of the natural radiation belts and of the mechanisms involved in their continual losses and regeneration is still rather limited after several years of investigation. At low altitudes, it has been established, however, that the atmosphere encountered by both trapped protons

1

and electrons in their trajectories dominates their behavior (Welch et al., 1963; Lenchek and Singer, 1963; Walt and MacDonald, 1964a). The interaction for electrons is primarily scattering, producing diffusion in both energy and pitch angle. A fraction of those which are scattered toward lower mirror points in the dense atmosphere are permanently lost. The replenishment of these elect...s to maintain the natural belts occurs in a manner which is not clearly understood. Unlike electrons, trapped protons lose their energy primarily through ionization interactions with the atmosphere in their path. The replenishing source of these protons is also not clearly understood although the decay of cosmic-ray albedo neutrons (Lenchek and Singer, 1963) appears to be one of the mechanisms. Difficulty in predicting the behavior of these trapped particles arises from the lack of detailed knowledge of the source term in both cases.

The Starfish high-altitude nuclear detonation of 9 July 1962 provided a unique opportunity to investigate the time behavior of trapped electrons since it created an intense artificial belt of electrons with fission-like energies at low L shells. In this situation, the source term was reasonably well known, and several satellite experiments were performed shortly after the event. Based on these early time data, Walt (1964b) has shown that the predominant loss mechanism for these fission electrons at $L \leq 1.25$ is atmospheric scattering. In particular, the narrow but important anomaly region of the inner radiation belt greatly influenced the lifetime of these electrons. Several experiments have been performed (Mozer et al., 1963; Imhof and Smith, 1965a,b,c,d; West et al., 1965; Beall et al., 1967) to investigate the intensity, spectrum and decay of this radiation belt. The Gemini IV and VII experiments offered a valuable opportunity to measure in detail the intensity, spectrum and decay of this radiation some three to four years after the event. By comparing early time data and the current results with the predictions based on atmospheric scattering, a great deal can be learned about the atmosphere controlling the decay rate and about other mechanisms such as low L-shell diffusion (Imhof and Reagan, 1967) which are also important in establishing the existing radiation environment.

In addition to the two spatial parameters, B and L, it has been shown (Welch et al., 1963; Paulikas and Freden, 1964; Imhof and Smith, 1965b; Vernov et al., 1965) that longitude also becomes an important controlling parameter

for electrons observed at low altitudes on almost any L shell. The fluxes of electrons for L ≲ 1.7 trapped with mirror points at B,L positions for which the minimum altitude is less than 100 km exhibit a strong dependence on longitude. Fluxes just west of the magnetic anomaly region are typically about an order of magnitude greater than those measured just east of the anomaly at comparable values of B and L. In addition, at a given B,L value the spectrum west of the anomaly is softer than that east of the anomaly. This effect has been attributed to large-angle coulomb scattering of trapped electrons resulting in their shift to high B values.

Experimental data (Freden et al., 1964; Heckman and Nakano, 1968) have shown that the equilibrium flux and spectrum of energetic protons in the inner radiation belt are quite stable. Since protons lose their energy primarily through ionization processes with the atmospheric constituents, a change in the flux should be observed as the atmospheric density changes during the solar cycle (Blanchard and Hess, 1964). The present data provide detailed proton fluxes and spectra during solar minimum for comparison with earlier results obtained closer to solar maximum. This comparison, particularly when combined with a similar analysis of electron data obtained from the same spectrometer, should results in an accurate definition of the atmosphere over this period.

Another interesting phenomenon associated with trapped protons at low altitudes is an observable east-west asymmetry in particle fluxes. Lenchek and Singer (1962) predicted that for mirroring protons with gyroradii comparable with the atmospheric scale height, an east-west asymmetry in the trapped flux should be observable. The assumptions in this prediction are that the atmospheric density varies exponentially with altitude and that the average atmospheric density encountered over an orbit is equal or proportional to the average over a circle of gyration at the mirror point. Direct observations of this asymmetry have been reported (Heckman and Nakano, 1963). This phenomenon was also observed in the Gemini IV experiment (Reagan, 1968) and since both the flux and spectra of the protons were measured as a detailed function of B,L space at or near the mirror points of the particles, a good deal can be learned about the influence that the atmosphere exercises in this effect.

3

A detailed knowledge of the fluxes and spectra of both electrons and protons on low L shells is also important from an operational aspect. The capability of predicting and calculating radiation doses to be received by astronauts and equipment on low-altitude, earth-orbiting satellite flights must be based on current and accurate knowledge of the radiation environment. This can only be provided by conducting periodic experiments such as the present ones. The limited quantity of available data on protons and electrons on low L shells is illustrated by Vette's (1966) model of the trapped radiation environment. For magnetic shells of L ≤ 1.7 only three sets of experimental electron data were available to Vette. Many more measurements were available for higher L shells. The situation is identical for protons. The present Gemini data should prove valuable in updating the current environmental model in this region.

Section 2

DESCRIPTION OF THE EXPERIMENTS

2.1 Proton-Electron Spectrometer - Gemini IV

The experiment performed aboard the Gemini IV spacecraft to measure the proton and electron environment utilized a scintillation detector in conjunction with a multichannel pulse-height analyzer. A cross-sectional view of this spectrometer is shown in Figure 1. The basic detector for both protons and electrons was a large plastic scintillator (Pilot-B) 7.87 cm in diameter and 5.08 cm high. The size and shape of the scintillator were chosen to provide high sensitivity and uniform path length over the entire acceptance solid angle of 1.2π steradians for electrons of energy from 0.45-8.0 MeV and protons of energy from 23.5-80 MeV.

Separation of electrons and protons was accomplished by the different ranges of energy deposit in the detector and the known relative intensities of the two types of particles within these ranges. In particular, there are a negligible number of electrons to be expected with energies above 8 MeV (Imhof and Smith, 1965c) compared with the expected proton flux above 23 MeV (Freden et al., 1964). The spectrometer was located at the center of the equipment-adapter module of the spacecraft with an aft view cone of 68.2 degrees half-angle. A thermal curtain which covered the rear of the module in combination with a thin (1 mg/cm^2) aluminized-mylar covering over the entrance aperture of the spectrometer eliminated protons with incident energy in the 0.5-8.0 MeV range.

The light from the detector scintillator was coupled to a ruggedized Type 4439 photomultiplier by a lead-glass light pipe 2.54 cm in diameter by 1.27 cm thick. This also provided approximately 5.1 gm/cm^2 of shielding for the detector scintillator in the backward direction. The lead glass combined with the shielding provided by the photomultiplier, electronics, aluminum containers, and the spacecraft reduced to a negligible quantity the effect of energetic particles entering the detector scintillator from the solid angle defined by the light pipe.

TUNGSTEN

REFLECTIVE PAINT

ANTICOINCIDENCE SCINTILLATOR

LEAD-GLASS LIGHT PIPE

POTTING COMPOUND

1 mg/cm² AL-MYLAR WINDOW

PLASTIC SCINTILLATOR

ALUMINUM

PHOTOMULTIPLIERS
TYPE C70102

TYPE 4439
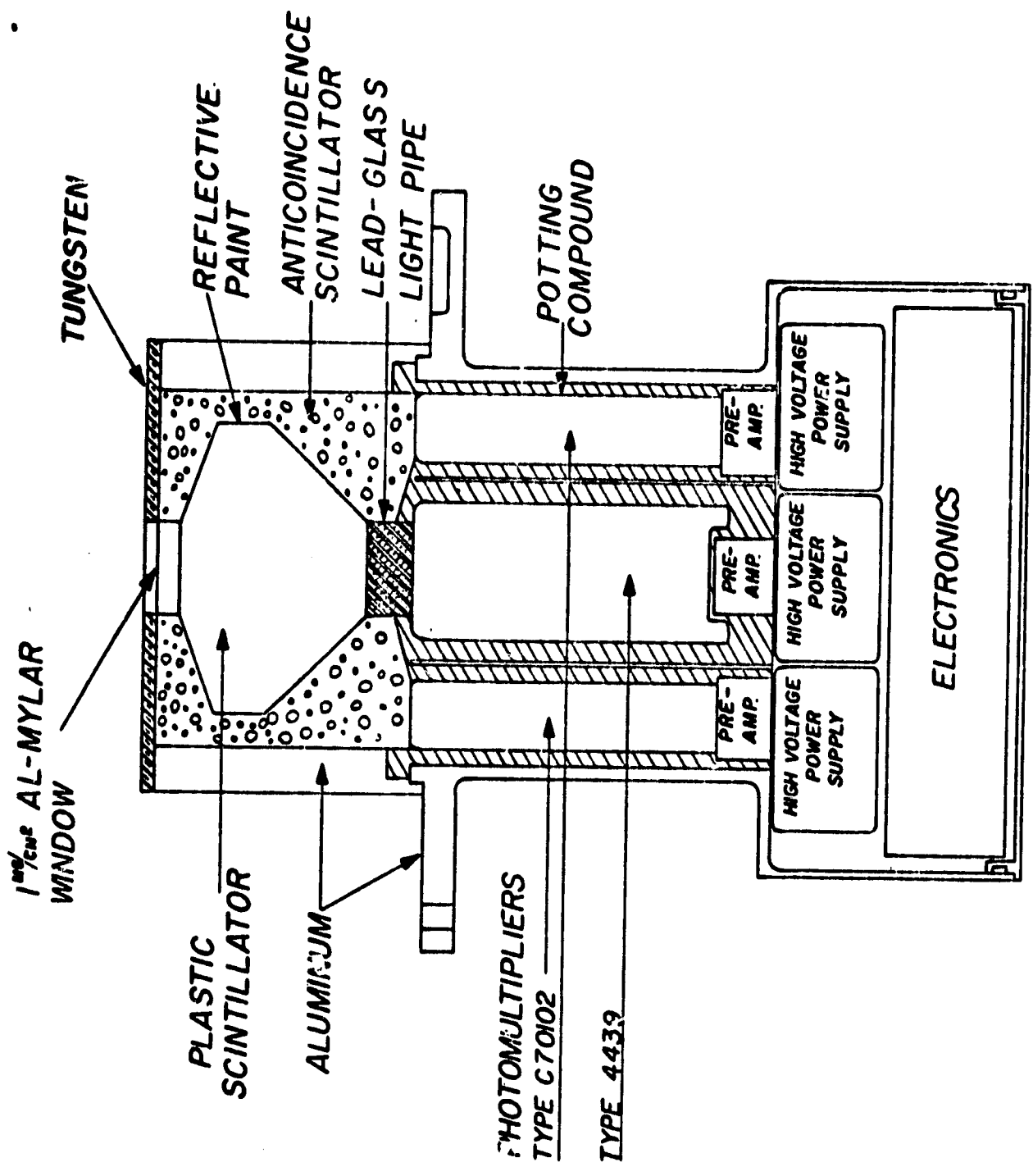
PRE-AMP.

HIGH VOLTAGE POWER SUPPLY

ELECTRONICS

Figure 1   Cross-Section Diagram of Gemini-IV Proton-Electron Spectrometer

The entire detector scintillator except for the acceptance aperture was surrounded by a combination of shielding material and an anticoincidence scintillator. The purpose of the shielding was to prevent the penetration of most of the energetic particles into the detector scintillator from directions other than the acceptance solid angle. The top of the scintillator was protected by a 0.28-cm thickness of tungsten (Fansteel-77) to provide a shielding of 5.41 gm/cm^2, corresponding to the range of an 8.5-MeV electron and a 53-MeV proton. Completely surrounding the main scintillator, except for a 2.54-cm diameter acceptance aperture and the light pipe, was a plastic (Pilot-B) anticoincidence scintillator. This scintillator had an energy threshold of approximately 300 keV and was sufficiently thick to detect all particles above that energy, including minimum ionizing cosmic rays. Thus, all particles not entering through the acceptance solid angle were rejected from further analysis. The aluminum shielding outside the anticoincidence detector was necessary to limit the anticoincidence dead time to a reasonable value by stopping most of the undesired energetic particles. Three photomultipliers, Type C70102, viewed the light from the anticoincidence scintillator to obtain maximum detection sensitivity.

Pulses from the detector-photomultiplier were coupled to the analysis system by a preamplifier stage with two discrete gain steps in order to cover the broad range of energy involved. This gain change was accomplished in flight by means of an internal solid-state timer which allocated alternate time periods of 18 seconds to each of the two energy ranges. An analog voltage from the timer to the telemetry provided a monitor on the range under analysis.

Pulses from the three photomultipliers viewing the anticoincidence scintillator were coupled to a common integral discriminator by three preamplifiers. When the discrimination level was exceeded, an enable signal was applied to an anticoincidence gate which then prevented any detector scintillator signal from being analyzed during the following 3-microsecond period. The enable pulses were also fed to a logarithmic ratemeter to provide the anticoincidence or singles rate to the telemetry. These pulses provided a measure of the omnidirectional proton flux greater than approximately 64 MeV.

Pulses from the detector scintillator which passed through the anticoincidence gate were analyzed by a 16-channel pulse-height analyzer of the analog-

7

to-digital conversion type (Rowland, et al., 1963; Reagan et al., 1965). The channel-address which corresponded to an input pulse-height from the detector was coded in binary format and was sampled in parallel as a four-bit bi-level word by the PCM telemetry system at a 20-sample-per-second rate. In this manner, a random spectrum sampling of the incoming radiation was obtained. Because of this relatively low-sampling-rate limitation, the absolute flux of incoming radiation was determined by a group of ratemeters. Pulses which passed the anticoincidence gate triggered a discriminator having a threshold which was matched to that of the pulse-height analyzer. Two linear ratemeters covered the counting range to about 800 counts per second. A logarithmic ratemeter which overlapped the linear ratemeter extended the counting rate capability to approximately 500,000 counts per second. The outputs of these ratemeters, which were analog voltages between 0 and 5 Vdc, were sampled by the telemetry and converted to an eight-bit binary word at a 1.25-sample-per-second rate.

A dc-to-dc converter was utilized to convert the unregulated input voltage to regulated instrument voltages and to provide the required isolation from the spacecraft. A temperature circuit which was capable of measuring the internal instrument temperature between $-30^\circ C$ and $+75^\circ C$ was also incorporated to permit temperature correction to be made to the data.

2.2 Proton-Electron Spectrometer - Gemini VII

A cross-sectional view of the spectrometer used on the Gemini VII experiment is shown in Figure 2. The basic detector for analyzing both protons and electrons was a cylindrical plastic scintillator (Pilot-B) 5.59 cm in diameter by 2.79 cm in height. These dimensions correspond to a normal incidence energy deposit of 5.0 MeV for electrons, 60 MeV for protons, and 5.7 MeV for minimum ionizing protons. The spectrometer aperture was 2.29 cm in diameter compared to the 2.54 cm diameter of the Gemini IV spectrometer. A "dE/dx" scintillator, which was 0.025 cm thick by 2.29 cm in diameter, was mounted adjacent to the "E" scintillator in a lucite light pipe which coupled the light output to an Amperex XP-1011-02 photomultiplier. The shielding which surrounded the entire detector assembly was similar to that employed in the Gemini IV spectrometer. Therefore, both scintillators were subjected only to those electrons which entered through the opening aperture. Energetic protons greater than approximately 60 MeV could also penetrate the shielding and be detected in the "E"
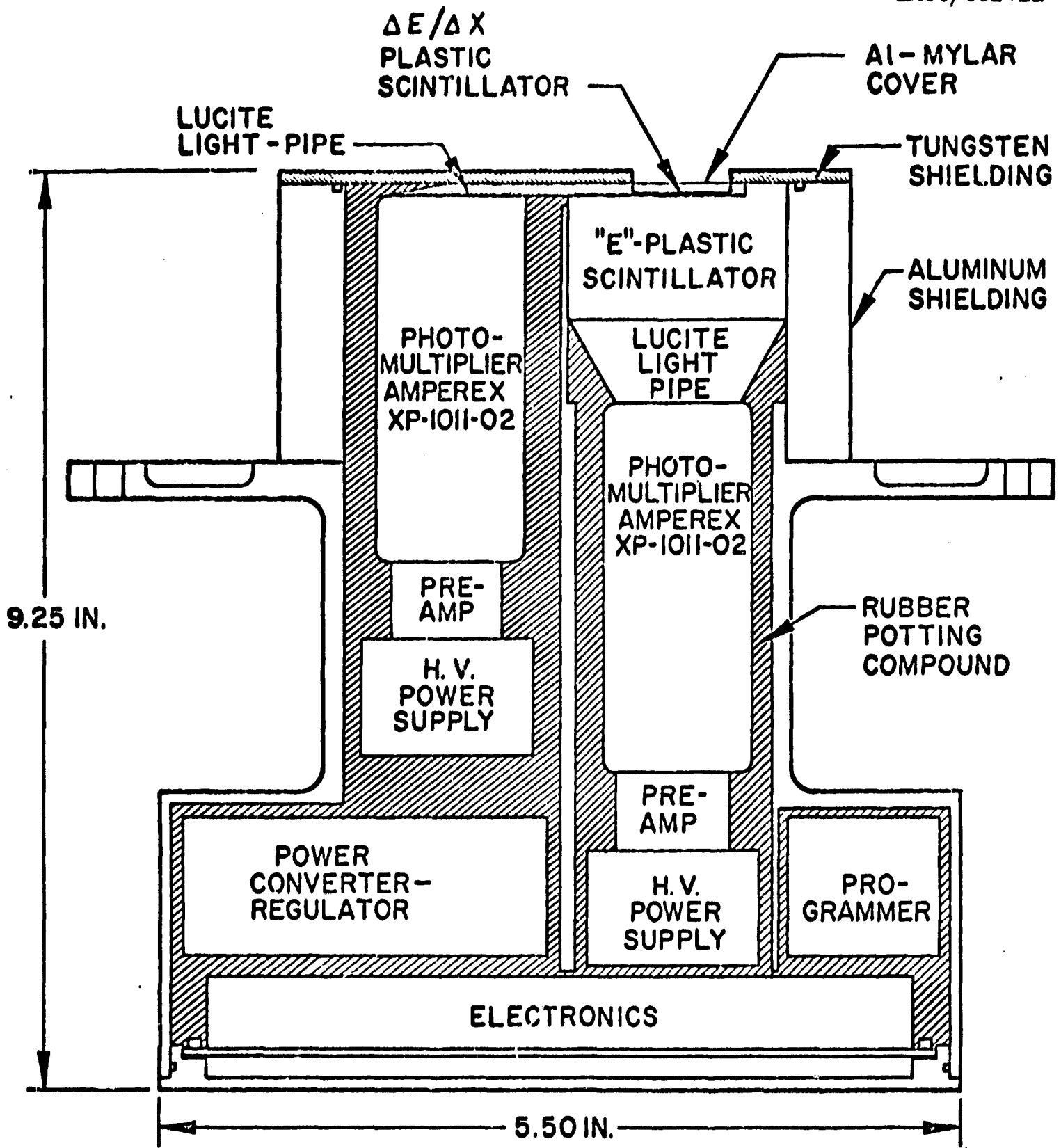
GT-7 PROTON-ELECTRON SPECTROMETER

Figure 2   Cross-Section Diagram of Gemini-7 Proton-Electron Spectrometer.

scintillator in the electron mode of operation. Over most spatial regions, however, this background flux within the electron energy range of interest was small because of the much higher flux of electrons within the acceptance aperture. The details of this penetrating background were measured in flight as the differential flux spectrum obtained when the detector was oriented with respect to the magnetic field such that the electron flux within the acceptance angle vanished. This differential flux as a function of the magnetic shell parameter, L, was then subtracted from the data obtained at other orientations. The spectrum of penetrating protons in the electron mode of operation consisted of a rather flat and small distribution throughout the electron channels of the pulse-height analyzer with a significant contribution in the last or overload channel. This overload channel therefore provided an effective measure of the omnidirectional energetic proton flux.

The light from the "E" and "dE/dx" scintillators was coupled to two ruggedized photomultiplier tubes, Type XP-1011-02. Since the spectrometer was to operate in two modes, an internal programmer was utilized to control and identify the time multiplexing of the modes. In the proton mode, a coincidence gate between the "E" and "dE/dx" signals was enabled for 18 seconds. In the electron mode, the programmer provided a continuous signal to one input of the coincidence circuit such that any signal from the "E" scintillator which exceeded the discrimination level would create a coincidence and open the signal gate.

The signals passing through this gate were analyzed for pulse height by a 16-channel pulse-height analyzer identical to that used in the Gemini IV experiment. Because the sampling of these data by the telemetry was performed at only 20 samples per second, alternate methods of obtaining the absolute counting rates were utilized. To obtain the absolute coincidence rate, two linear ratemeters covering the range from 0 to 2000 counts/sec were used. In the proton mode, this range was adequate to cover the expected proton flux. In the electron mode, these ratemeters functioned essentially as "singles" counters since a coincidence was not demanded. To extend the electron range to approximately 3×10^5 counts/sec, a logarithmic ratemeter was used which continuously monitored the output of the "E" discriminator. A logarithmic ratemeter also continuously monitored the output of the "dE/dx" discriminator. All four ratemeters had an output voltage range of 0-5 Vdc and were sampled

1.25 times per second. A temperature sensor was also included to allow corrections to be made to the data for the effects of temperature. An internal dc-dc converter provided regulated power for the instrument and isolation from the vehicle power system.

Section 3

CALIBRATION PROCEDURE

3.1 Laboratory Calibration

The flight spectrometers were calibrated extensively in the laboratory prior to launch to determine their response to protons and electrons over the energy and intensity range of interest. In addition, calibrations with both electrons and protons were performed on the "backup" spectrometers during the period of this data analysis effort. To accomplish these, a variety of calibration devices, including radioactive sources, a beta-ray spectrometer, and particles obtained from accelerators such as the Lockheed 3.5-MeV Van de Graaff and the Harvard 160-MeV synchrocyclotron accelerators, were used. A description of these additional calibrations follows. The reader is referred to a previous report (Reagan, 1966a) for a description of the pre-launch calibrations.

3.1.1 Post-Calibration with Radioactive Sources

The "backup" spectrometers from both flights were post calibrated with electrons obtained from radioactive sources and a 180-degree beta-ray spectrometer. This spectrometer which employed Sr^{90}-Y^{90} as a source of electrons permitted the selection of monoenergetic electrons up to 2.27 MeV in energy. Detailed spectra as a function of energy and angle of incidence were obtained to measure the effect that backscattered electrons had on the resulting flight spectra. Figure 3 illustrates a typical spectrum obtained from the "E" scintillator in the Gemini VII spectrometer for incident mono-energetic 2-MeV electrons. The backscattered spectrum is relatively flat and the intensity in all lower channels above the flight energy threshold of approximately 0.5 MeV is less than 10 percent of the peak energy.

The energy resolution of the spectrometers as a function of electron energy was also determined with the beta spectrometer. Figure 4 shows the energy resolution of the Gemini IV spectrometer as a function of incident electron energy as obtained in this manner. The measured resolution was 32.5, 27.0 and 21.3 percent FWHM at energies of 1.0, 1.5 and 2.0 MeV, respectively. Because of this rather poor resolution, which is attributed to the large and
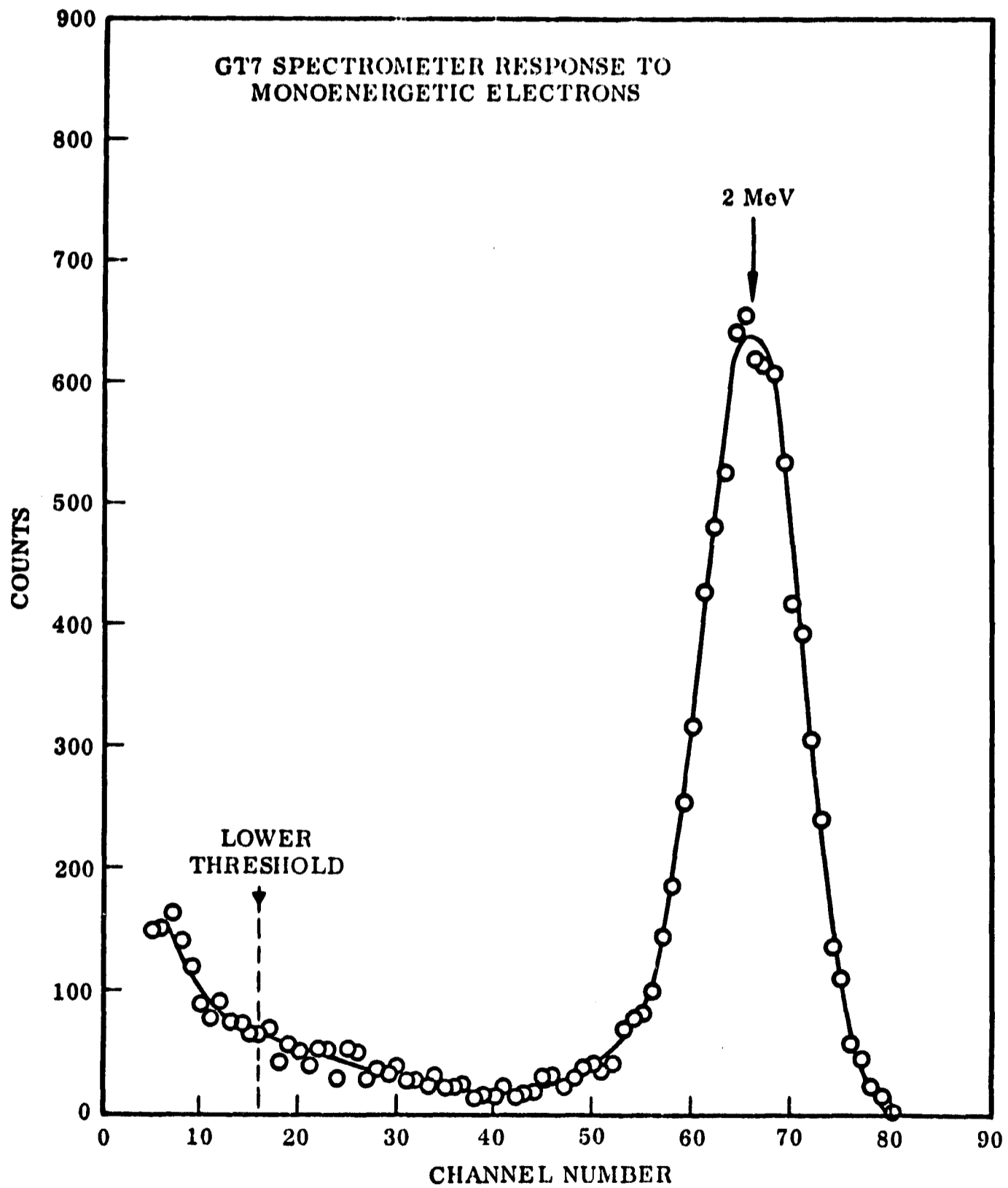
12

Figure 3   Response of the Gemini VII Spectrometer to Monoenergetic 2-MeV Electrons
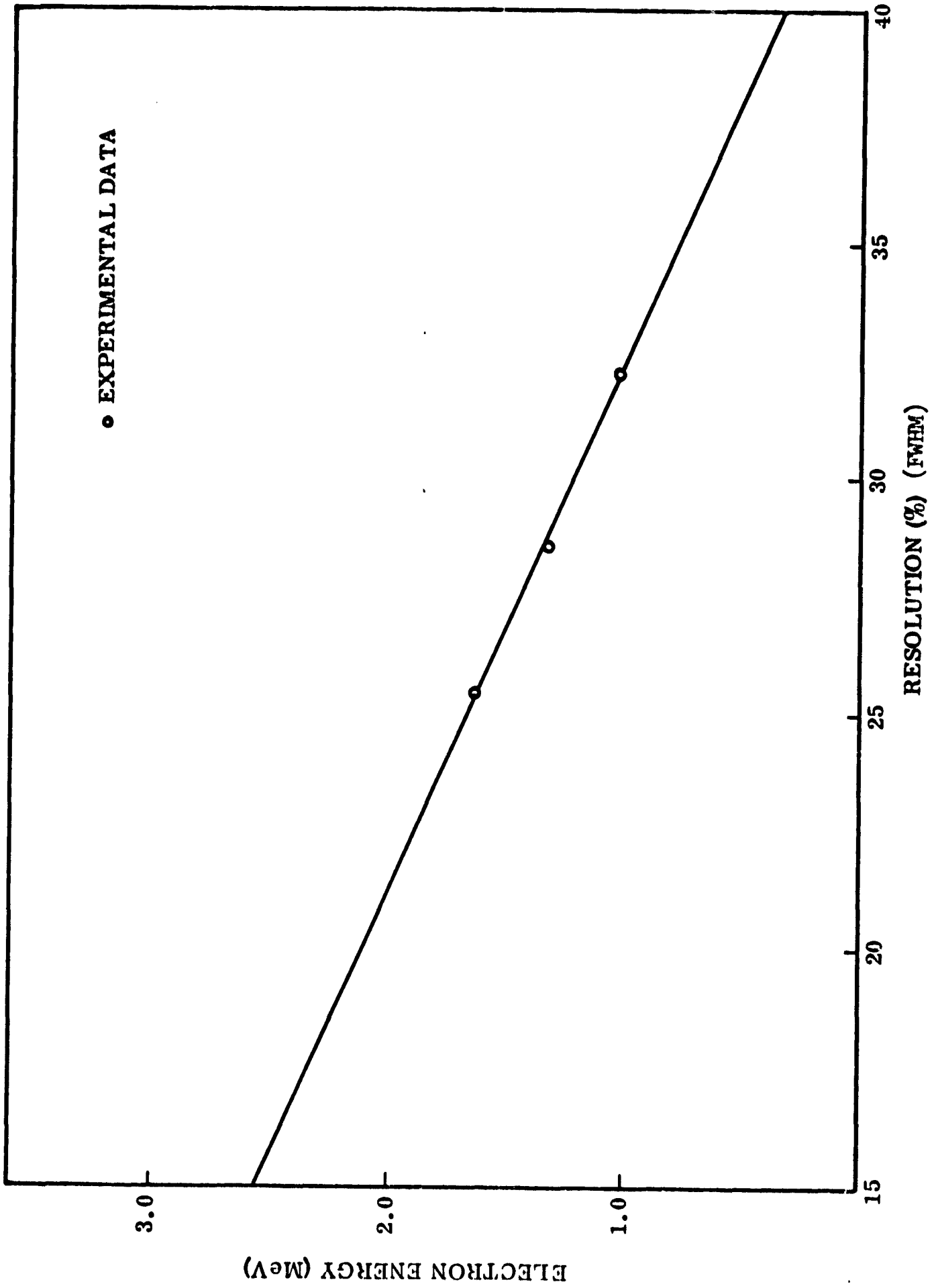
Figure 4 Energy Resolution of the Gemini IV Spectrometer as a Function of Incident Electron
Energy

unusual shape of the scintillator, and since the backscattering effect was small, no correction has been applied to the shape of the flight spectra for either of these effects.

The angular distribution data obtained from the beta spectrometer were also used to verify the calculated geometric factors of the instruments. In Figure 5, the calculated geometric factor consists of the geometrically derived expression relating the counting rate and the omnidirectional flux plus a small, flat, integral contribution to account for scattering and bremsstrahlung which was observed in flight at incident angles greater than the geometrical cutoff angle. These topics are described in greater detail in later sections. The experimental data at energies of 1.0 and 1.5 MeV are in excellent agreement with the calculated curve over most of the acceptance angle range.

Finally, the post calibrations with the beta spectrometer were used to finalize the electron energy calibrations of the flight pulse-height analyzers. The backup spectrometers were adjusted to provide the same output spectra as the flight units for a thorium-C gamma-ray source. This was the same radioactive material present in the spacecraft structure which was used as an in-flight calibration source. The backup units were then subjected to monoenergetic electrons and analyzer calibrations, such as that shown in Figure 6 for the Gemini IV spectrometer, were obtained.

3.1.2 Accelerator Calibrations

The response of the Gemini IV spectrometer to energetic protons was measured with protons obtained from the Harvard 160-MeV synchrocyclotron accelerator. This accelerator is ideal for calibrating large spectrometers such as those used in the two Gemini experiments. A nearly monoenergetic beam of protons with a broad spatial extent of over 40 x 30 cm was available for calibration. The broad characteristics of the beam, which were obtained by scattering the primary accelerator beam off a lead target, closely approximated the proton environment in space and allowed the simultaneous calibration of the central scintillator as well as the effectiveness of the entire anticoincidence detector. Proton energies between approximately 20 MeV and 130 MeV were obtained by inserting calibrated polyethylene and polystyrene absorbers in the beam path. Figure 7 shows the response of the spectrometer to protons with an energy of 55.2 MeV. A beam resolution of 10.76 MeV was

CALCULATED GEOMETRIC FACTOR
EXPERIMENTAL DATA

O E_e = 1.0 MeV
□ E_e = 1.5 MeV

INCIDENT ANGLE, θ_Z (deg)
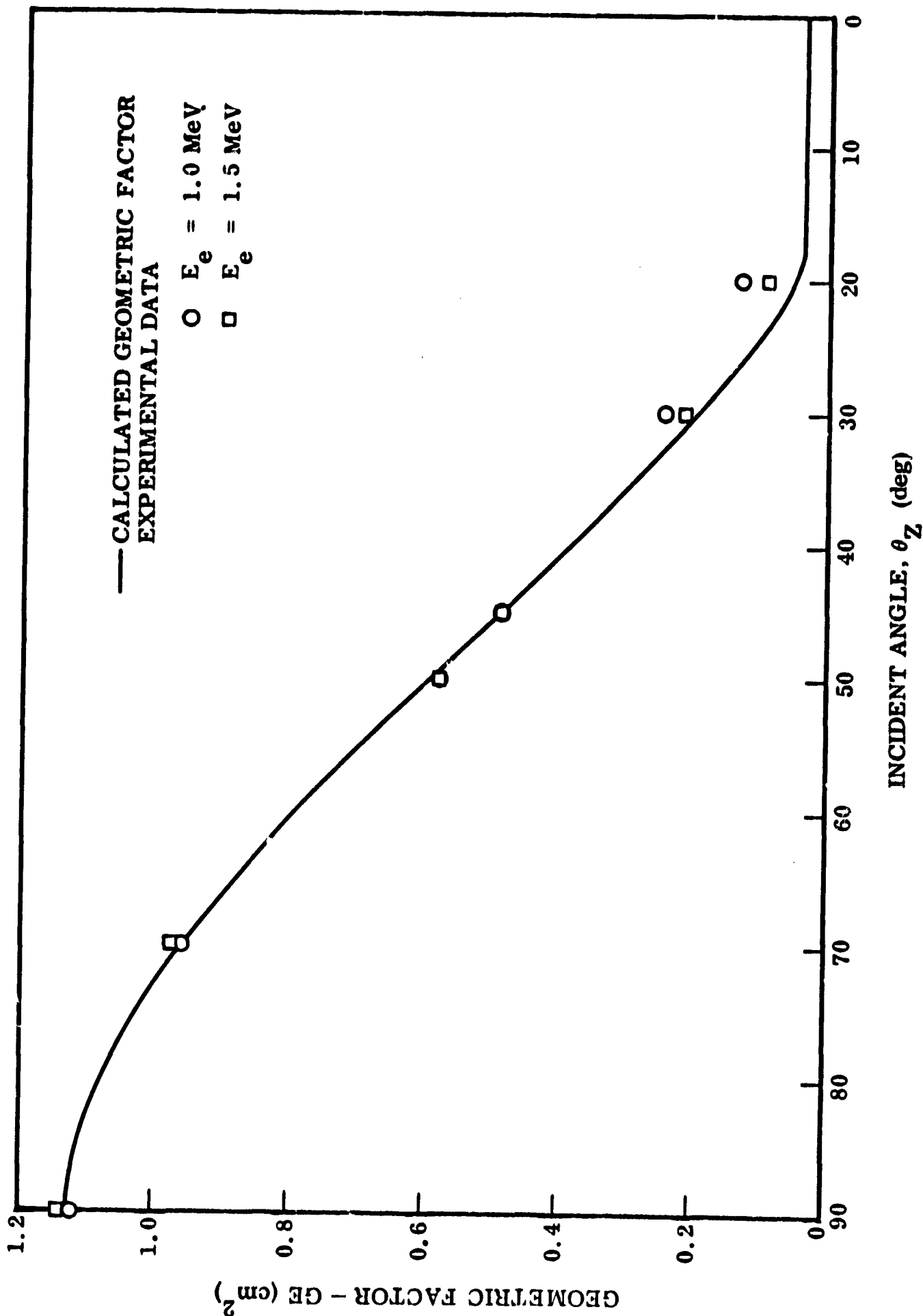
GEOMETRIC FACTOR – GE (cm^2)

Figure 5   Comparison of the Calculated Geometric Factor of the Gemini IV Spectrometer as a Function of Incident Angle with Experimental Data at Electron Energies of 1.0 and 1.5 MeV.
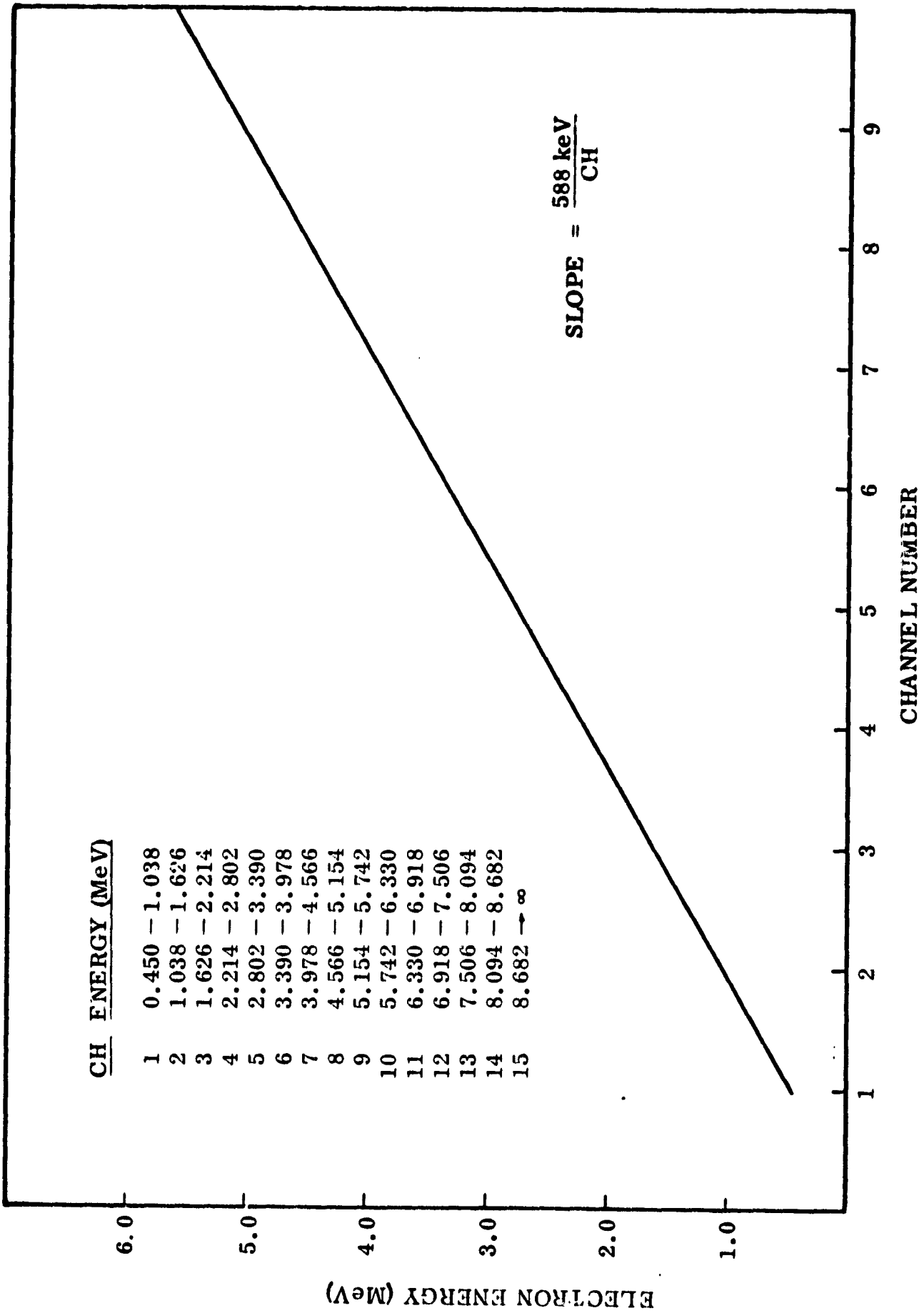
Figure 6   Electron Energy Calibration of the Gemini IV Spectrometer

CH	ENERGY (MeV)
1	0.450 — 1.038
2	1.038 — 1.626
3	1.626 — 2.214
4	2.214 — 2.802
5	2.802 — 3.390
6	3.390 — 3.978
7	3.978 — 4.566
8	4.566 — 5.154
9	5.154 — 5.742
10	5.742 — 6.330
11	6.330 — 6.918
12	6.918 — 7.506
13	7.506 — 8.094
14	8.094 — 8.682
15	8.682 → ∞

$$\text{SLOPE} = \frac{588 \text{ keV}}{\text{CH}}$$

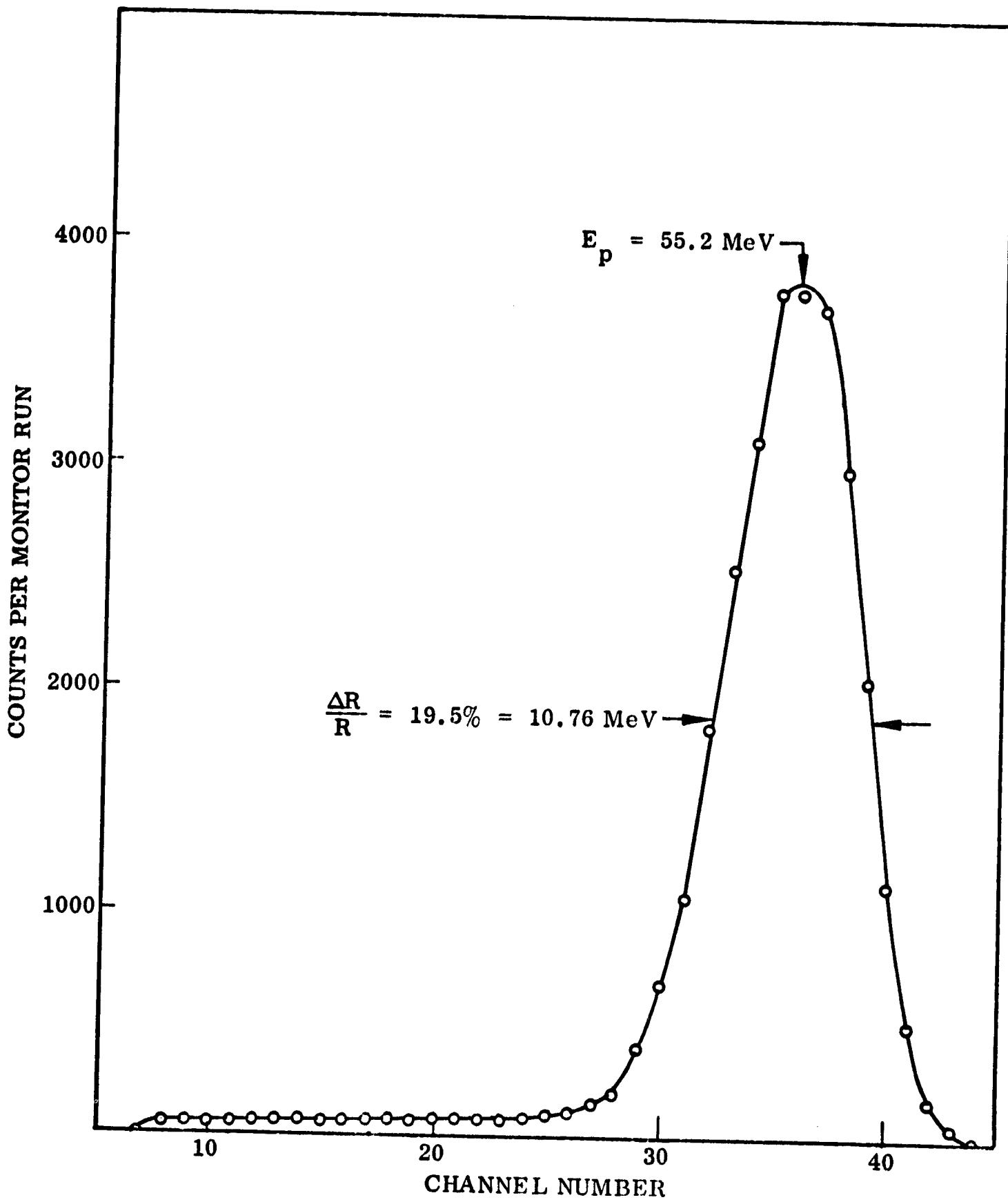CHANNEL NUMBER

ELECTRON ENERGY (MeV)

Figure 7 Response of the Gemini IV Spectrometer to Nearly Monoenergetic
Protons of 55.2 MeV Energy

measured at this energy. It should be noted that this resolution was primarily due to the degraded beam and not to the spectrometer which had considerably better resolution at this energy. This resolution was, however, comparable with the resolution available from the flight pulse-height analyzer and was quite satisfactory for our purpose. The clean, flat response of the spectrometer below the main peak should also be noted. Figure 8 shows the proton energy calibration for the Gemini IV spectrometer that resulted from this accelerator work. The experimental data obtained are in good agreement with the predicted response based on an energy calibration with electrons, and on the known electronic gains of the flight electronics, along with the known difference in light efficiency of plastic scintillator material to protons and electrons. The upper-energy linear cutoff of the spectrometer scintillator at 82 MeV was also substantiated by utilizing the higher energy incident protons and observing the reduced pulse heights in the resulting spectra.

The proton energy threshold of the anticoincidence detector was also experimentally determined during the Harvard accelerator calibration. Protons at several energies near the threshold of the anticoincidence shielding were used at both normal and antinormal incidence to establish the average response of this detector. Figure 9 shows the results of this calibration. The energy at the half-maximum response point for 0° and 90° incidence was 59.3 MeV and 69 MeV, respectively. An "average" response curve was then generated with a half-maximum response energy of 64 MeV. It is this energy that will hereafter be referred to as the proton energy threshold of the anticoincidence detector.

3.2 In-Flight Calibration

The gamma rays emitted from the small amount of radioactive thorium metal present in the adapter section of the spacecraft was used as an in-flight calibration source on both the Gemini IV and VII spectrometers. This background produced a counting rate of approximately 30 counts per second in the electron mode of the spectrometers and provided the spectrum shown in Figure 10 in the Gemini IV spectrometer. The Compton edge at 2.38 MeV associated with the 2.61 MeV gamma ray from the thorium was used as a distinguishing energy point in the spectrum. Since the shape of the pulse-height spectrum near the Compton edge depends in detail on the geometry, the thorium spectrum was cross calibrated with electrons prior to launch to provide an absolute energy point in
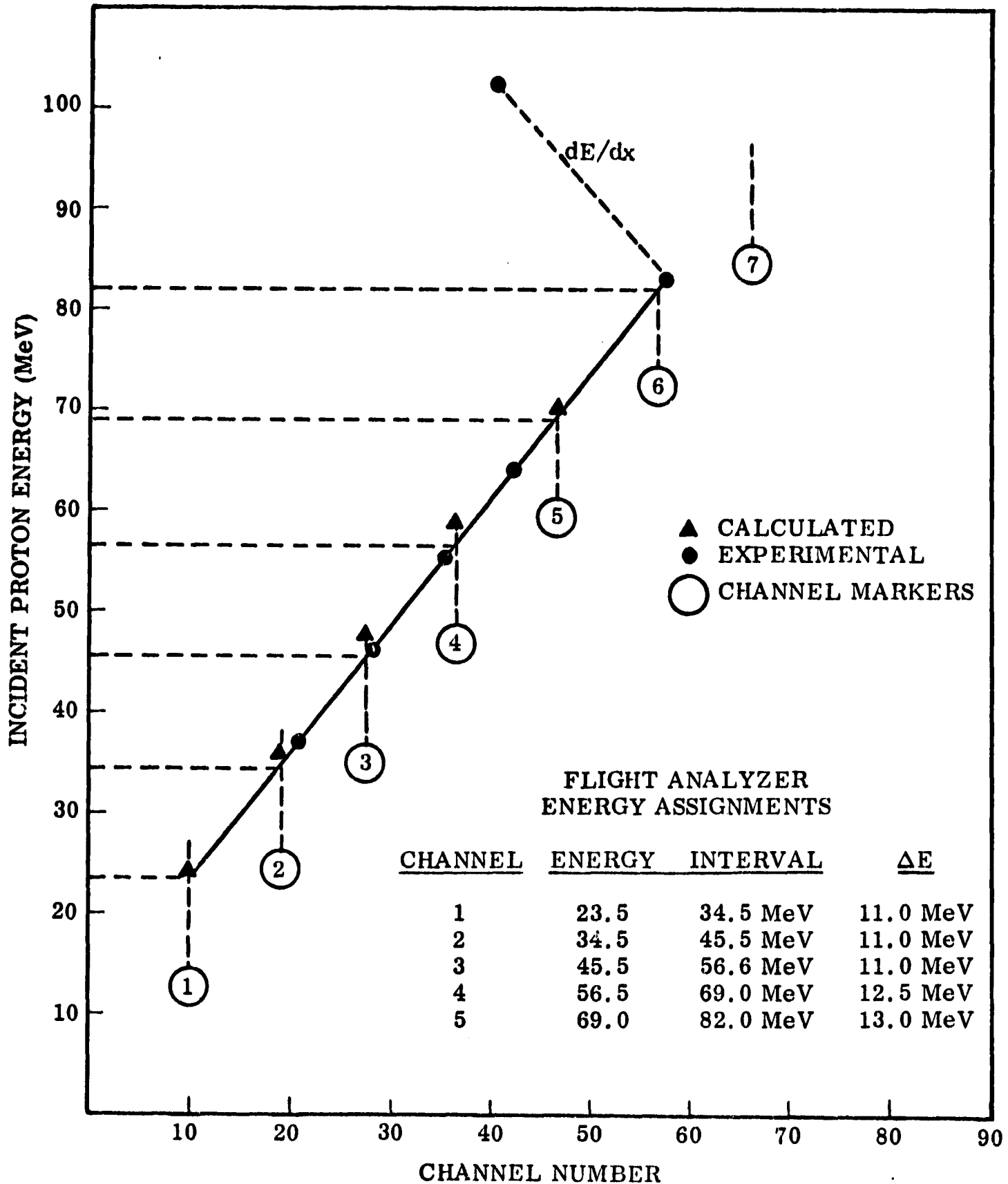
Figure 8 Proton Calibration of the Gemini IV Spectrometer Based on
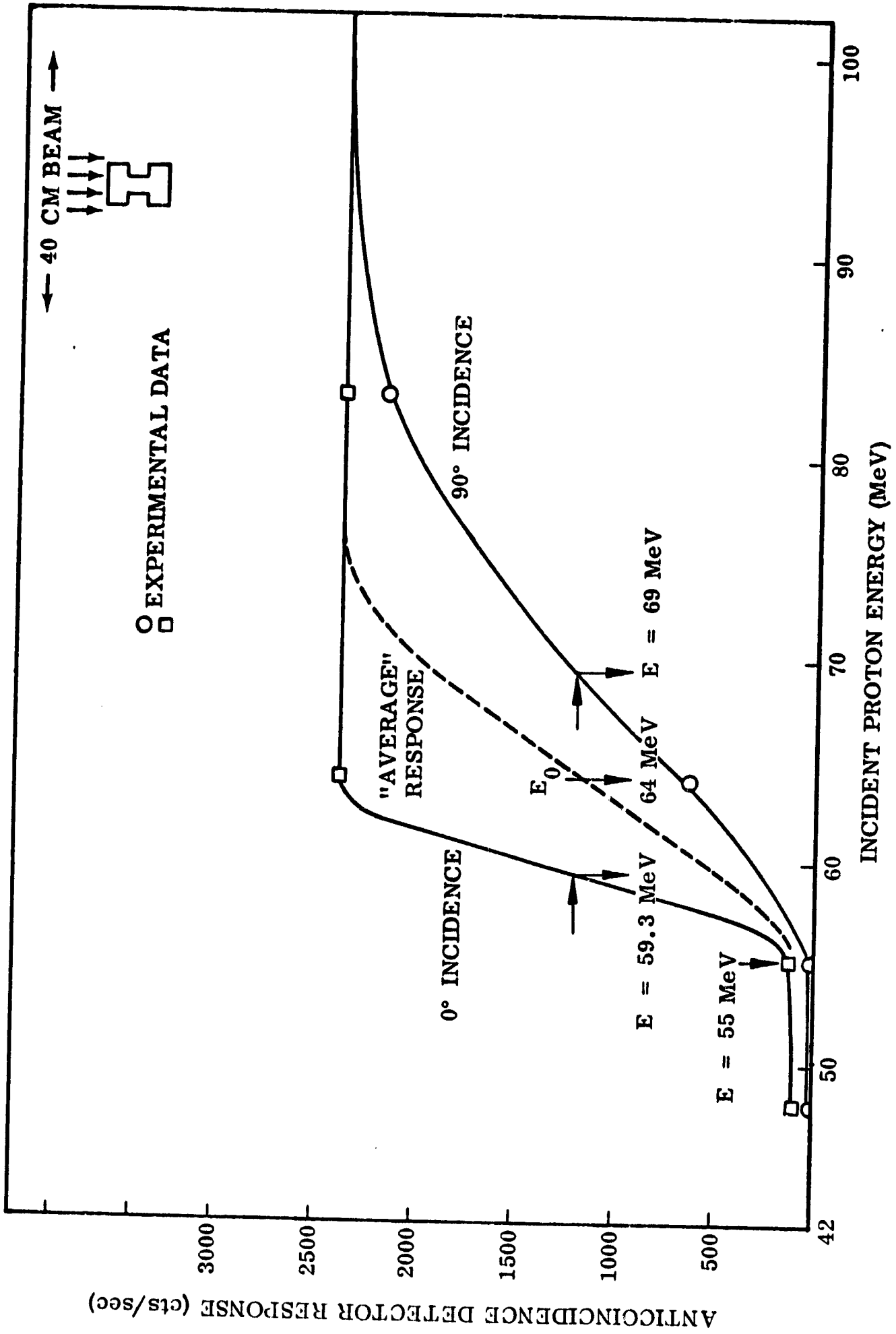Calculated and Experimental Data

Figure 9 Energy Threshold Calibration of the Anticoincidence Detector in the Gemini IV Spec-
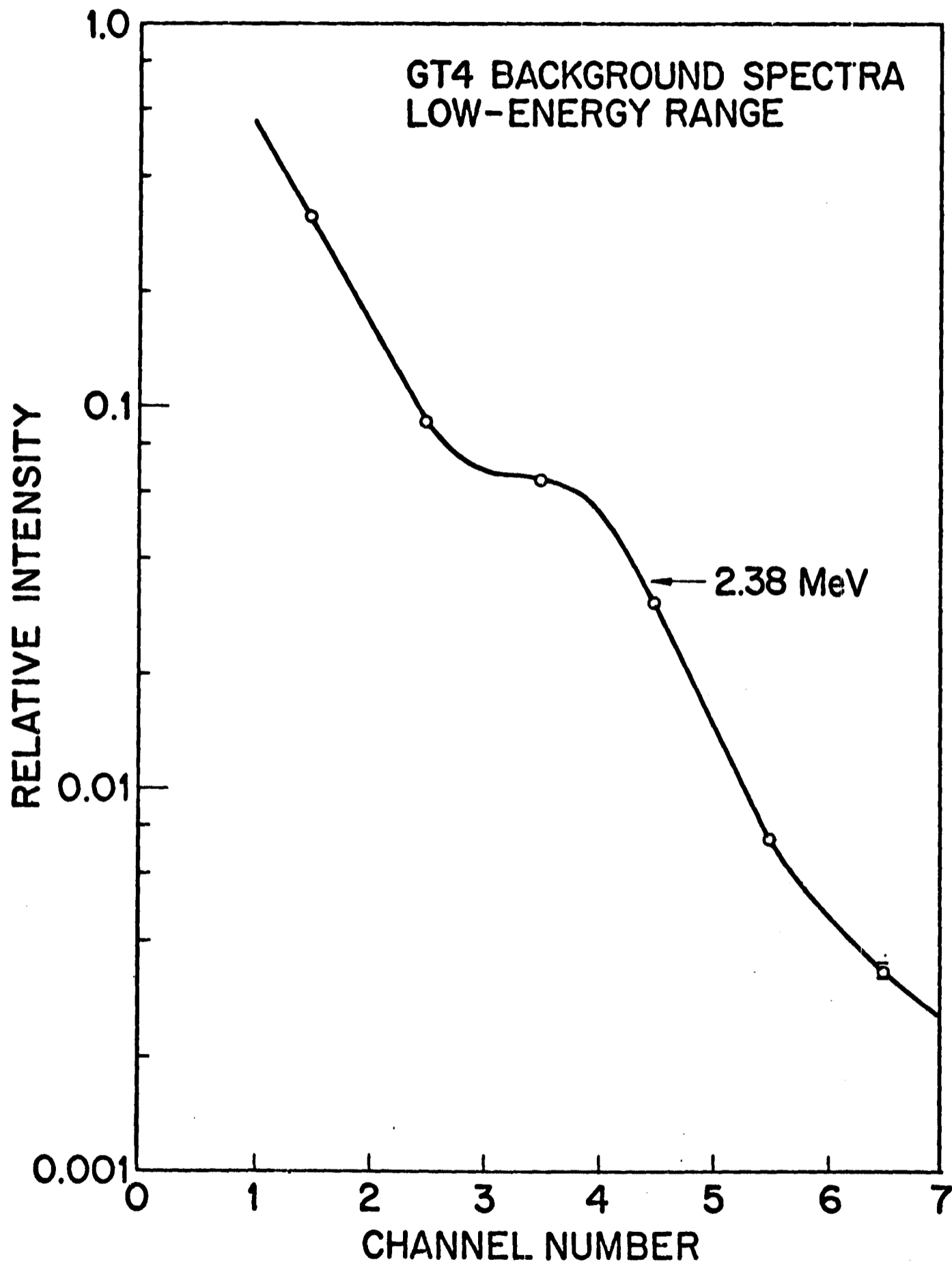trometer

Figure 10   Spectrum of the Thorium Background Used as an In-
            Flight Calibration Source on the Gemini IV Spec-
            trometer

flight. This spectrum, which was the only background present in the Gemini IV
spectrometer over regions where trapped particle fluxes were not present, was
compiled on an orbit-by-orbit basis with sufficiently good statistics to
observe even small gain shifts. No measurable gain shifts throughout the
Gemini IV flight were observed.

In addition to the thorium background, the Gemini VII spectrometer detected
a cosmic background in the electron mode which was of comparable intensity to
the thorium source. The absence of an anticoincidence detector in this spec-
trometer caused the additional background. The resulting composite spectrum,
as shown in Figure 11, made detection of the thorium edge somewhat more dif-
ficult since the cosmic-ray intensity is known to be a function of L shell
location. The procedure used was to assume that the thorium contribution was
negligible in the highest four channels of the spectrometer based on the back-
ground spectra obtained on the ground, as shown in Figure 11. The final thorium
spectrum obtained during grc nd calibrations was then subtracted from the com-
posite in-flight spectrum. The resulting spectrum was assumed to be attribut-
able entirely to cosmic rays in regions where trapped particle fluxes did not
exist. As can be seen in Figure 11, the cosmic-ray spectrum was rather flat
and of low intensity in the lower channels of the pulse-height analyzer. The
main contribution from cosmic rays was in the last or overload channel of the
analyzer which is consistent with the external source being highly penetrating
particles at near minimum ionization. The shape of the cosmic ray spectrum
obtained in this manner was assumed to be independent of L shell with only the
intensity of the cosmic rays being a function of L. The cosmic-ray intensity
so obtained was compiled as a function of L shell at B values where trapped
particle fluxes could not exist and is shown in Figure 12. The solid line
shown in this figure is the L dependence of cosmic rays as obtained by Lin et
al. from geiger-tube data on Explorer 7. The Lin (1963) data have been normalized
to the Gemini VII data to account for the different geometric factors of the
two instruments. The data are in good agreement and substantiate the cosmic
ray subtraction technique employed.

When the cosmic-ray contribution was subtracted from the measured composite
spectrum, the resulting thorium spectrum was easily discernible. The location
of the thorium edge was compiled on an orbit-by-orbit basis throughout the
flight. Gain shifts amounting to 30 percent from the average were observed at
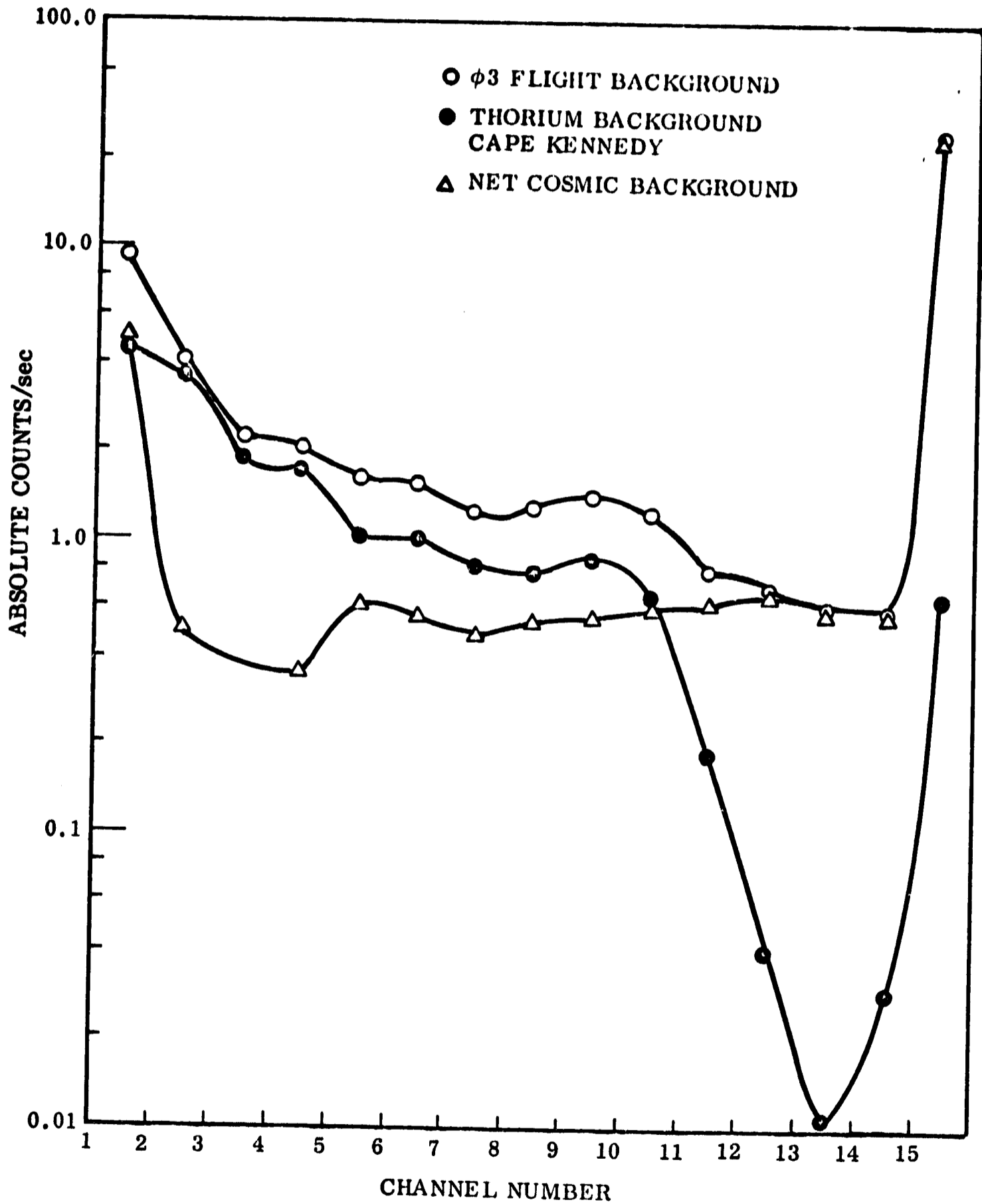
23

Figure 11 Background Spectra Obtained with the Gemini VII Spectrometer. The Ground-Based Thorium Spectrum was Subtracted from the Composite In-Flight Spectrum to Obtain the Net Cosmic-Ray Spectrum.
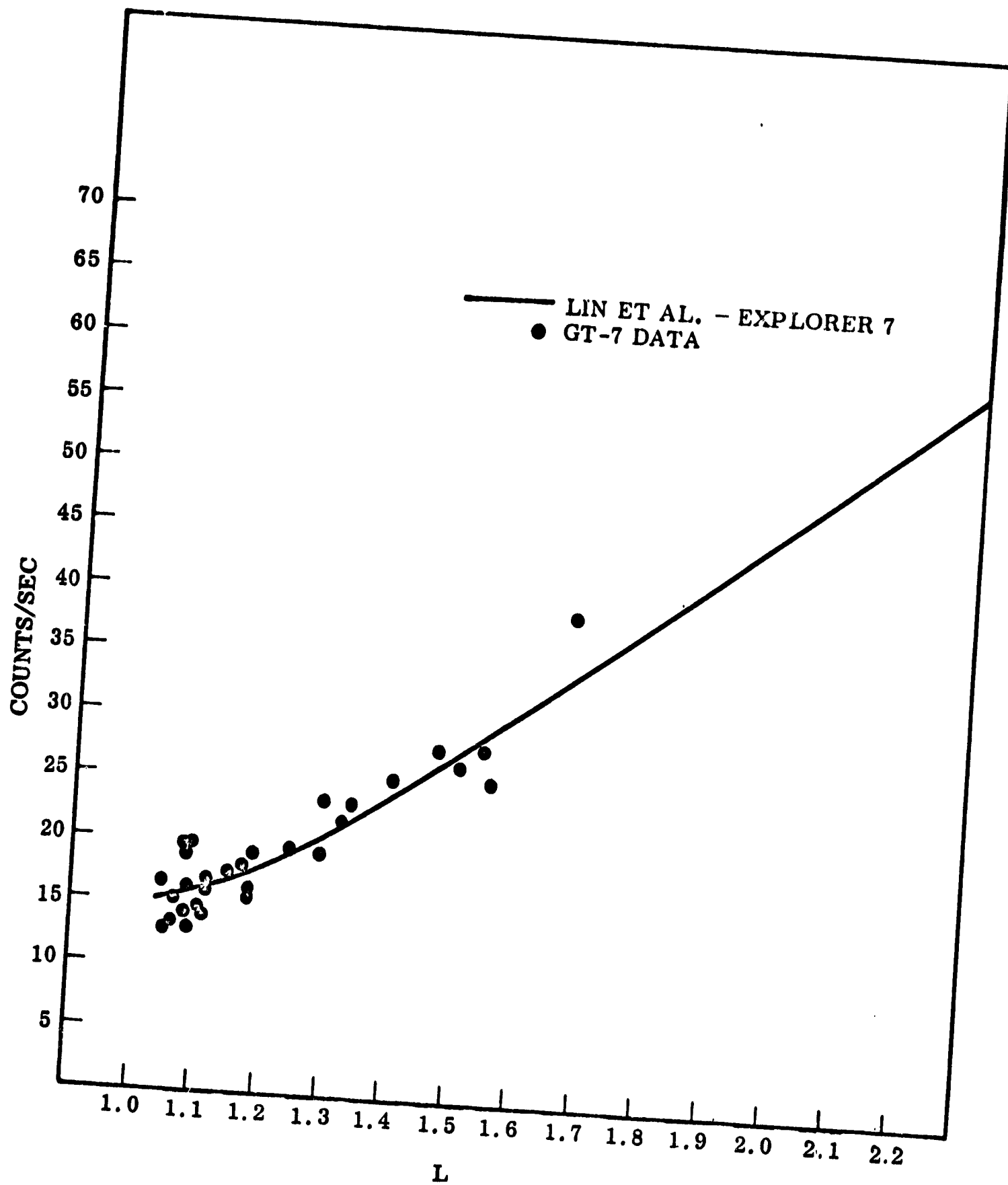
Figure 12 Cosmic-Ray Intensity Obtained with the Gemini VII Spectrometer as a Function of L-Shell

the temperature extremes but the more typical gain shifts from orbit to orbit were less than ten percent. In all cases, when processing the data, the energy calibration of the spectrometer was adjusted just prior to each anomaly pass to account for these variations. The accuracy in the energy calibration of the Gemini VII spectrometer is therefore considered to be of the order of $\pm$ 5 percent.

Section 4

DATA PROCESSING

4.1 Data Quantity and Quality

Data were obtained from the spectrometer throughout the Gemini IV flight period of 3-7 June 1965. Of the total of twelve orbits which were programmed for turn-on, nine orbits of good data were obtained. The remaining data were lost because of poor signal quality on the flight magnetic tapes. Data were obtained from the Gemini VII spectrometer for the first seven-day period of the 4-18 December 1965 flight. An on-board tape recorder failure at that time prevented the acquisition of any further data. Over seventy orbits of data were available and have been processed, but difficulties with the magnetic tapes have significantly reduced the amount of useful data. These difficulties, which were primarily associated with erroneous data on the original computer tapes such as incorrect B,L values at certain times, improper time intervals, and incorrect magnetometer data, demanded that a great deal of expensive test, monitoring and correctiv action be employed to be assured of good data.

On both flights, the analog voltage outputs of the spectrometer were provided every 0.8 seconds. The sixteen samples of the digital pulse-height analyzer outputs which were obtained during this time period were decoded, sorted, and listed by channel number on the original computer tapes. Data from a companion tri-axis magnetometer experiment were also provided by the NASA/MSC. Pertinent spacecraft ephemeris data were provided for both flights in five second intervals and merged with the B,L program of McIlwain (1961) to provide the spectrometer data in terms of the earth's magnetic field strength, B, and the magnetic shell parameter, L.

4.2 Orbit Coverage in B,L Space

Because of the low-altitude, low-inclination, circular nature of these two Gemini flights, significant radiation fluxes were encountered only in the vicinity of the Brazilian anomaly. In this region, which is located between South America and Africa, the magnetic field of the earth departs drastically from a dipole field representation and both trapped and precipitated particles are observed at low altitudes. Figure 13 shows the regions of each orbit of

Gemini IV in B,L coordinates where significant particle fluxes above background were observed. The orbital paths in B,L space for the Gemini VII flight are shown in Figure 14. On both flights, the region of 1.1 < L < 1.7 and 0.213 < B < 0.260 was reasonably well covered by the orbital trajectories through the anomaly. The magnetic equator is plotted on Figures 13 and 14 as well as the locus of B,L points corresponding to particles which in their longitudinal drift around the earth encounter a minimum altitude of 100 kilometers. Particles encountering minimum altitudes less than this value are presumably lost in a very short time due to atmospheric collisions. Therefore, one can expect to encounter particle fluxes with significant lifetimes on these flights only in the B,L region below the h_{min} = 100 km curve. Spacecraft altitudes in this region varied between 274 and 293 kilometers.

It has been recently demonstrated (Lindstrom and Heckman, 1968) that significant differences can occur in the trapped particle fluxes in this region of B,L space depending on which model of the earth's magnetic field is used in the calculations. Lindstrom and Heckman have also shown that the Goddard Space Flight Center 99-coefficient magnetic field model (9/65) and the GSFC 120-coefficient model (12/66) equally describe the geomagnetic field in the South Atlantic anomaly for the epoch 1965. We have therefore converted all of our B,L data from the originally used Jensen and Cain (1962) field model to the GSFC (9/65) field model (Hendricks and Cain, 1966). All of the final B,L contours presented in this report were calculated from the latter field mode. Preliminary data presented in earlier reports were calculated from the former field model so that differences in flux contours should be anticipated.

4.3 Computer Processing

The data from both flights have been processed through a master computer program written for this purpose. The program accepts the raw data tapes and merges these data with ephemeris data from an additional set of tapes and ultimately provides a condensed reduced master data tape.

The preliminary goal of the program was to reduce the quantity of data to be ultimately processed. This was accomplished through data averaging over each energy range time period of the spectrometers, i.e., approximately every 16 seconds. This was judged to be a reasonable minimum time period based on preliminary analysis of the data and on the fact that statistically accurate spectra could be obtained in this interval. The average ratemeter values in each inter-
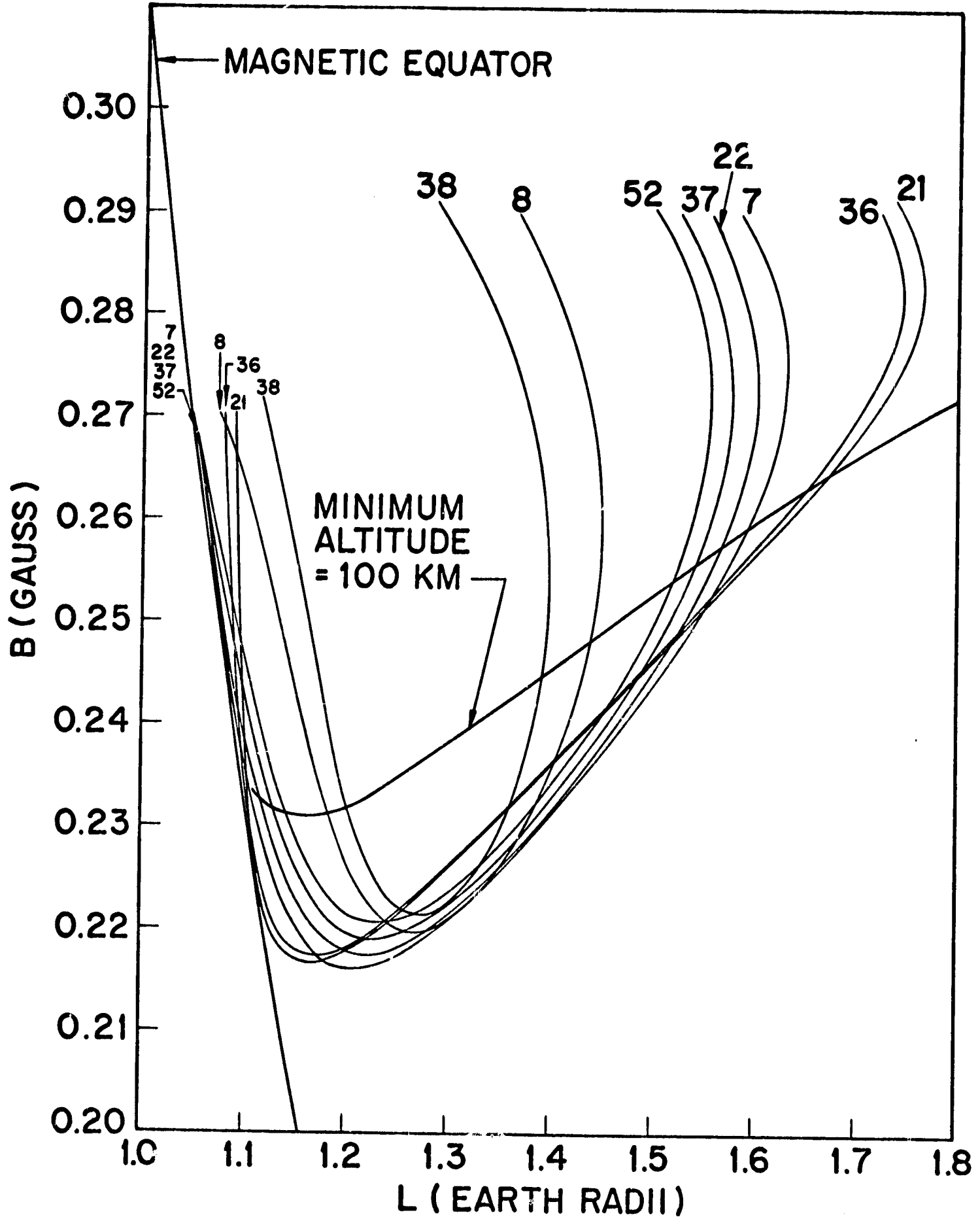
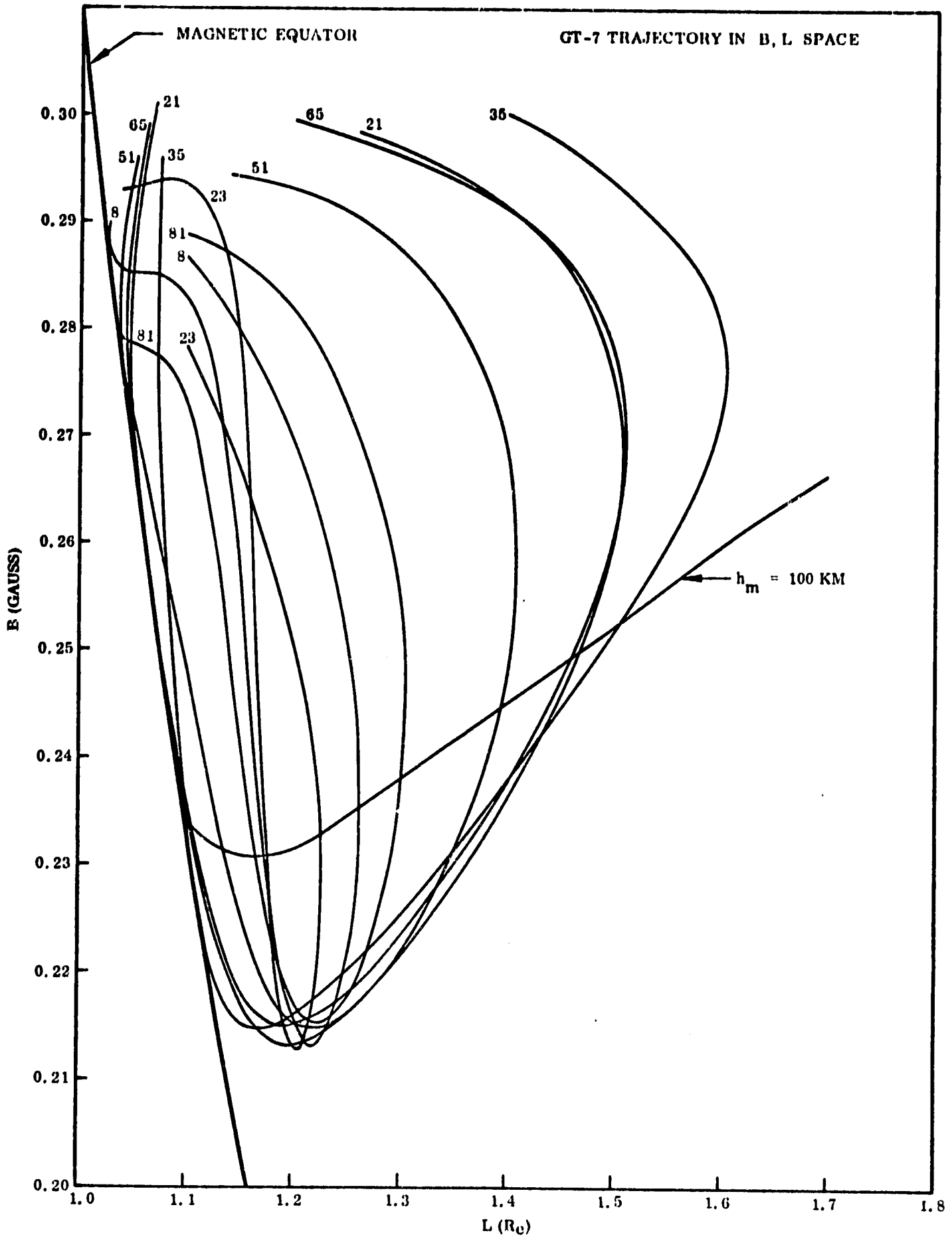Figure 13 Regions of B,L Space Covered by the Gemini IV Flight

Figure 14   Regions of B,L Space Covered by the Gemini VII Flight

val were converted to counting rates in the computer through the application
of the appropriate calibration curves. No temperature corrections were
necessary or applied to the Gemini IV calibration curves. A small temperature
correction was applied to several orbits of the Gemini VII data. In counting
rate regions where ratemeter overlap existed, agreement was usually within
less than 10 percent in counting rate. The averaged data were computer plotted
in all cases and compared with the computer plotted raw data to verify the
accuracy of the averaging procedure prior to subsequent calculations.

Ephemeris data were interpolated in time to correspond to the averaged
data time in each range interval. The values of B and L, utilizing the GSFC-
1965 magnetic field model, were then calculated for this time. The value of
h_{min}, the minimum altitude encountered by the particles on that B,L trajectory,
was then obtained from a subroutine written at LMSC which also utilizes the
GSFC-1965 field model.

4.3.1 Magnetometer Data

The orientation of the spectrometers at any given time was obtained
from tri-axis magnetometer data available from a companion experiment provided
by the NASA/MSC. The Gemini IV magnetometer had a rather large residual magnetic
field present on one axis of the magnetometer which had to be subtracted in the
data processing. On the Gemini VII flight, only two axes of magnetometer data
were available. Fortunately, it was established that the residuals in the remain-
ing axes were small. The calculated value of the total scaler magnetic field was
used to supplement the available data in order to arrive at the angle between the
spectrometer and the magnetic field. A computer processing error in the original
data also caused the available outputs to vary in quantized steps instead of in
a smoothly varying manner. This latter problem was solved through a least-
square-fit analysis of the magnetometer data prior to the angular calculation.

The angle between the axis of the spectrometer and the magnetic field
was calculated in each case at the time corresponding to the averaged data.
Despite the difficulties encountered with the magnetometer data, it is felt that
the final orientation information is accurate within ± 5 percent. This accuracy
is based on calculations performed on the Gemini IV magnetometer data. The scaler
value of the magnetic field, as calculated from the magnetometer data after the
residuals were removed, agreed with the magnetic field model to within ± 5 per-
cent in all cases. The reader is referred to an earlier report (Reagan, 1966a)

31

for a more detailed treatment of these offsets. As will be seen in the next section, the geometric factors of the instruments are not especially sensitive to small changes in the orientation angle so that small errors in this angle do not create large errors in the subsequent omnidirectional flux.

4.3.2 Geometric Factors

The counting rates observed by the detectors are related to the omnidirectional particle fluxes by the expression

$$\epsilon G = \frac{C}{J_O} \qquad (1)$$

where C is the net detector counting rate, after backgrounds have been subtracted and dead time corrections have been applied; J_O is the omnidirectional flux, ϵ is the efficiency of detection as a function of orientation and energy, and G is the geometric factor of the instrument. Since the counting rate observed for a given aperture of area A in a unidirectional particle flux j is C = jA, the total counting rate is given by the sum over solid angle $C = \int jAd\Omega$, while the omnidirectional flux is defined by $J_O = \int jd\Omega$ so that

$$\epsilon G = \frac{\int jAd\Omega}{\int jd\Omega} \qquad (2)$$

As can be seen from Figure 1, the radiation incident on the plane of the detector was collimated by the finite tungsten shielding and the thickness of the anticoincidence scintillator in the vicinity of the aperture. The effective area A of the detector is then the area available for the passage of particles through the ends of an open-ended cylinder, as shown in Figure 15.
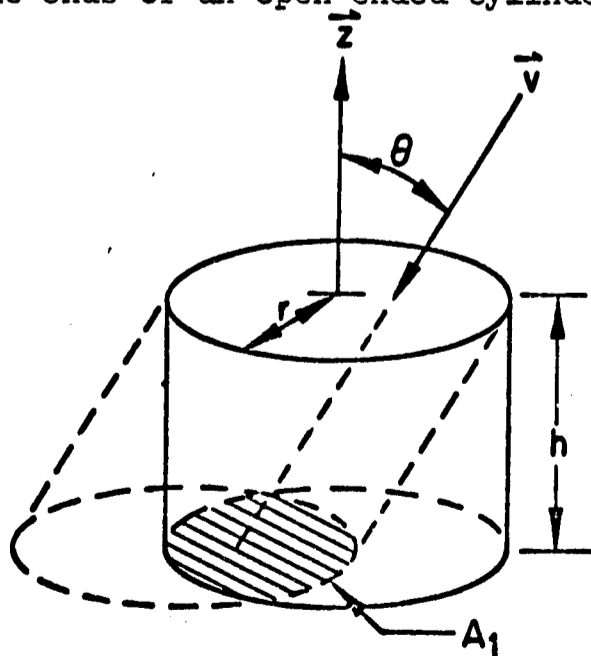

Figure 15. Effective Area of the Spectrometers Available to Particles as a Function of the Incident Angle θ.

This area can be expressed by the relation

$$A = A_1 \cos \theta$$
$$= \pi r^2 \cos \theta \left\{ 1 - \frac{2}{\pi} \left[\sin^{-1} (\delta \tan \theta) + \delta \tan \theta \sqrt{1-(\delta \tan \theta)^2} \right] \right\} \quad (3)$$

where $\delta = h/2r$.

The spatial distribution of the particle flux must be taken into account before this last equation may be used to integrate equation 2. Heckman and Nakano (1963) have shown that in the anomaly region at these altitudes the particle fluxes are near their mirror points and are therefore confined to a plane or "Pancake" distribution normal to the local magnetic field. The relationships between the particle flux, the longitudinal axis of the detector, and the magnetic field vector can then be described as shown in Figure 16.
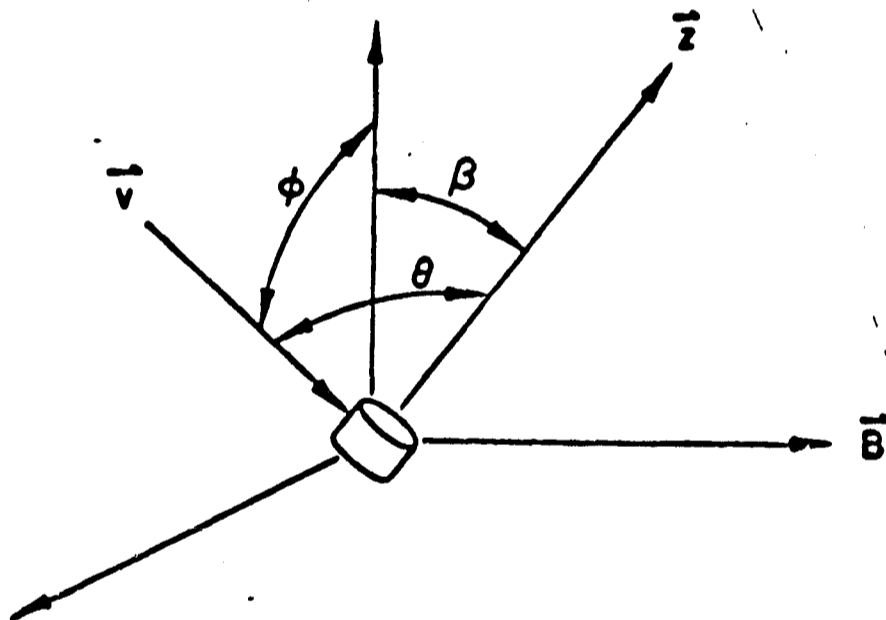

Figure 16. Angular Relationships Between the Incident Particle Flux $\vec{V}$, the Longitudinal Axis of the Spectrometer Z, and the Magnetic Field Vector, $\vec{B}$.

The assumptions that the flux distribution parallel to $\vec{B}$ is constant over the dimension of the aperture and that the angular distribution of j can be expressed completely by $j(\varphi) = $ constant leads to the expression

$$G = \frac{1}{2\pi} \int \epsilon [\theta(\varphi), E] \ A[\theta(\varphi)] d\varphi \quad (4)$$

If β is defined as the minimum angle θ between the Z axis and the plane of the particle flux, as shown in Figure 16, the relation between θ and φ is

$$\cos \theta = \cos \beta \cos \varphi \quad (5)$$

33

and
$$\frac{d\varphi}{d\theta} = \frac{\sin\theta}{\sqrt{\sin^2\theta - \sin^2\beta}}.$$

Substitution of this expression into equation 4 yields

$$G(\beta) = \frac{1}{\pi} \int_{\theta_{min}=\beta}^{\theta_{max}} \epsilon(\theta,E) \frac{A(\theta)\sin\theta \, d\theta}{\sqrt{\sin^2\theta - \sin^2\beta}} \qquad (6)$$

where θ_{max} is the angle at which $A(\theta)$ goes to zero and is determined by the geometry of the detector and its location in the spacecraft. The above expression has been solved by numerical integration for fixed values of β.

In the determination of the geometric factors for electrons in both spectrometers, the efficiency term, $\epsilon(\theta,E)$, has been equated to unity. This assumption is valid based on the size and shape of the scintillators used for the electron energy range of interest. The calculated electron geometric factors for the Gemini IV and VII spectrometers as a function of the angle, θ_z, between the axis of the spectrometer and the magnetic field are shown in Figures 17 and 18, respectively.

In addition, a small quantity, k, is added to the above calculated geometric factor to account for scattering, bremsstrahlung and penetrating particles which constituted a small background counting rate. This factor is energy dependent, hence a different value of k was applied to each energy channel of the spectrometer. The values of k were determined by observing the flux and spectra obtained in the electron mode at identical B,L locations in space but from two or more passes where the orientation was well within the acceptance cone in one case and near or beyond the geometrical cutoff angle in the other case. A set of such data obtained from the Gemini VII spectrometer at an L value of 1.301 and B value of 0.223 is shown in Figure 19. The values of k ranged from 0.059 in the lowest energy channel to 0.079 in the higher energy channels. At most orientations, the values of k exert a very small influence on the subsequent omnidirectional flux values. At orientations near or beyond the cutoff angle, however, the values of k greatly influence the omnidirectional flux values since the calculated geometrical factor vanishes. An overall analysis of the data indicates that the values of k used adequately predict the
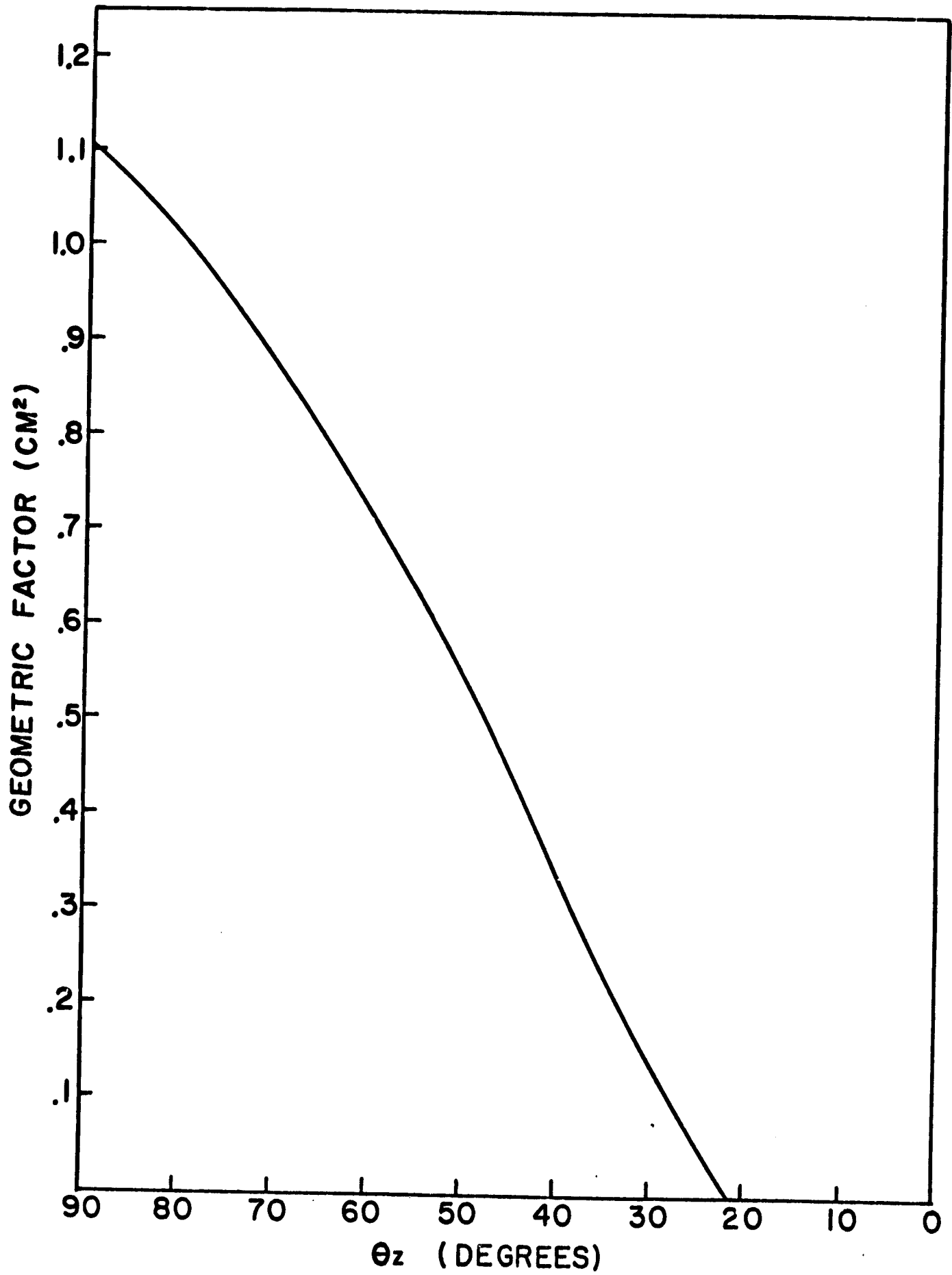
34

Figure 17   Calculated Geometric Factor for the Detection of Electrons
in the Gemini IV Spectrometer as a Function of the Angle,
θ_Z, Between the Spectrometer and the Geomagnetic Field.
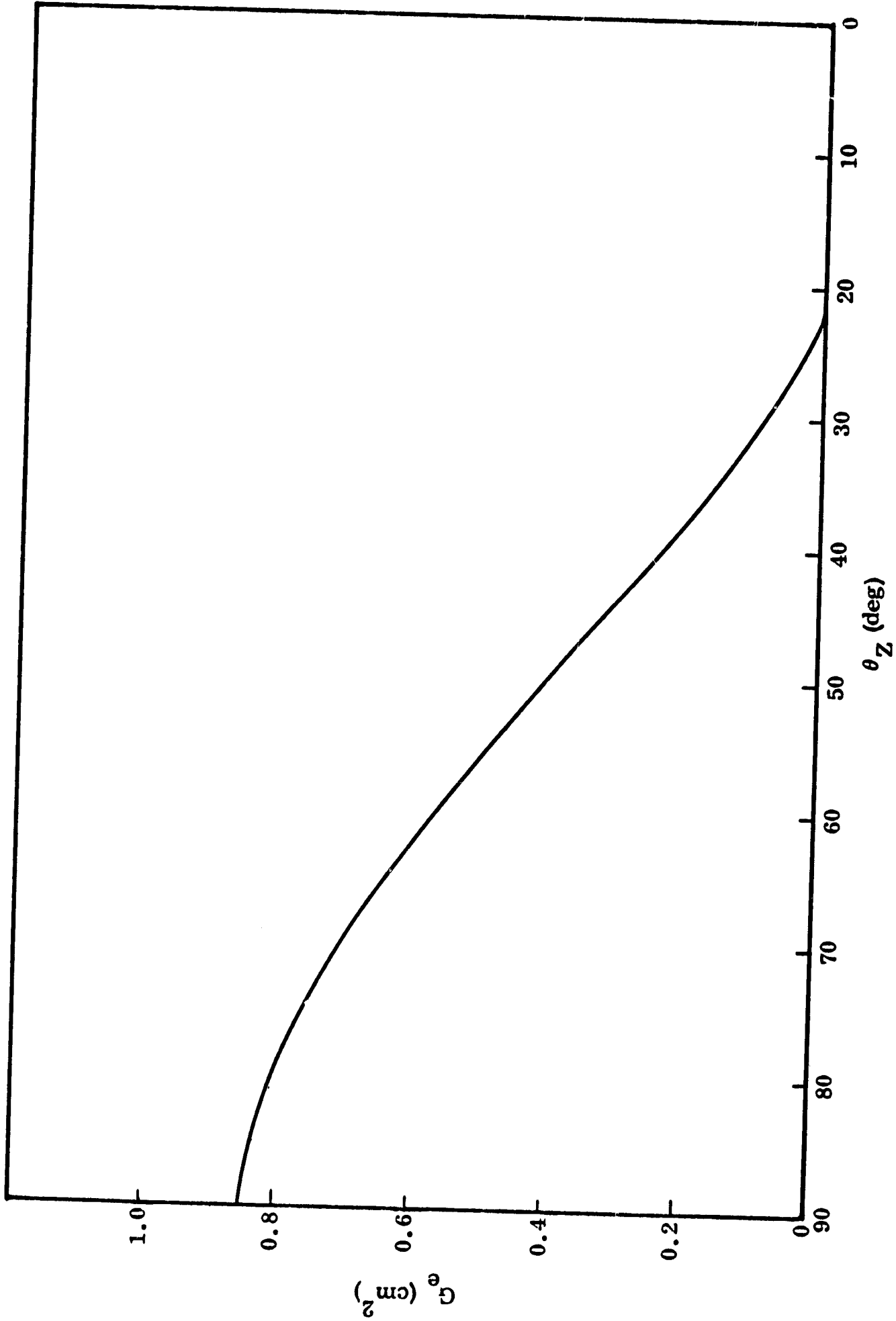
35

Figure 18 Calculated Geometric Factor for the Detection of Electrons in the Gemini VII Spectrometer as a Function of the Angle θ_Z.
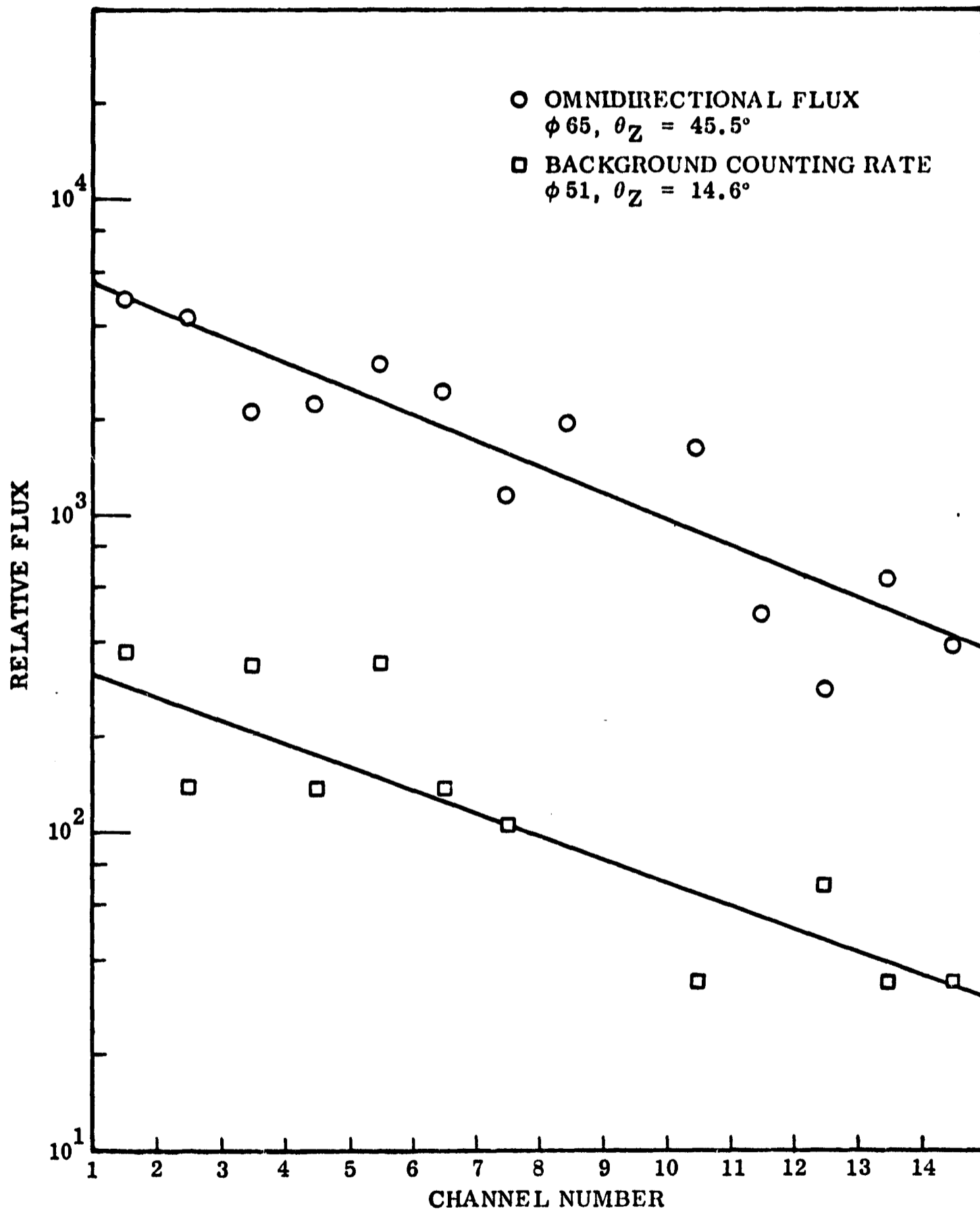
Figure 19   Flux and Spectra Obtained from the Gemini VII Spectrometer
in the Electron Mode from Two Orbits at Identical Locations
in Space of L = 1.301 and B = 0.223 but at Different Orienta-
tion Angles.

omnidirectional flux even in these regions. However, in the interest of eliminating as much error as possible, data obtained at orientation angles less than 25 degrees have been eliminated from the final flux contours and spectra analysis.

In the determination of the geometric factor for protons in the 23.5-80 MeV energy range, the efficiency term is a function of both proton energy and orientation. A special computer program was written to calculate this efficiency factor. The program treats in considerable detail the geometric shape and size of the scintillators and the range-energy relationship of protons in the scintillator for a pancake-flux distribution. As a function of orientation, the range of incident protons is calculated as a function of energy to determine if the range of the particle is greater than or less than the range of the scintillator. In the former case, the efficiency is taken as zero and in the latter case as one. The proton geometric factors calculated in this manner for each energy channel of the Gemini IV spectrometer are shown in Figure 20. The efficiency factor has no effect on the lowest three energy channels of the spectrometer and only a small effect on the 56.5-69.0 MeV energy channel. This factor is, however, important in the fifth or last linear energy channel of the spectrometer.

The omnidirectional flux of protons above approximately 64 MeV was obtained from the Gemini IV anticoincidence scintillator. This detector was basically a cylinder of plastic scintillator material of sufficient thickness to detect any particle which penetrated the surrounding aluminum and tungsten shielding. Since the shielding was equivalent to the range of an 8.5 MeV electron, there was a negligible counting rate from penetrating electrons. Laboratory tests with intense electron sources up to 2.27 MeV in energy demonstrated that this detector would not respond to the bremsstrahlung produced by the electrons. The observed counting rate was therefore produced by energetic protons or higher Z particles.

The geometric factor for a cylinder in an isotropic flux situation is simply

$$G_{ISO} = \frac{A}{4} \tag{7}$$

where A is the area of the scintillator exposed to the penetrating protons. The geometric factor in this case is of course independent of orientation. On the
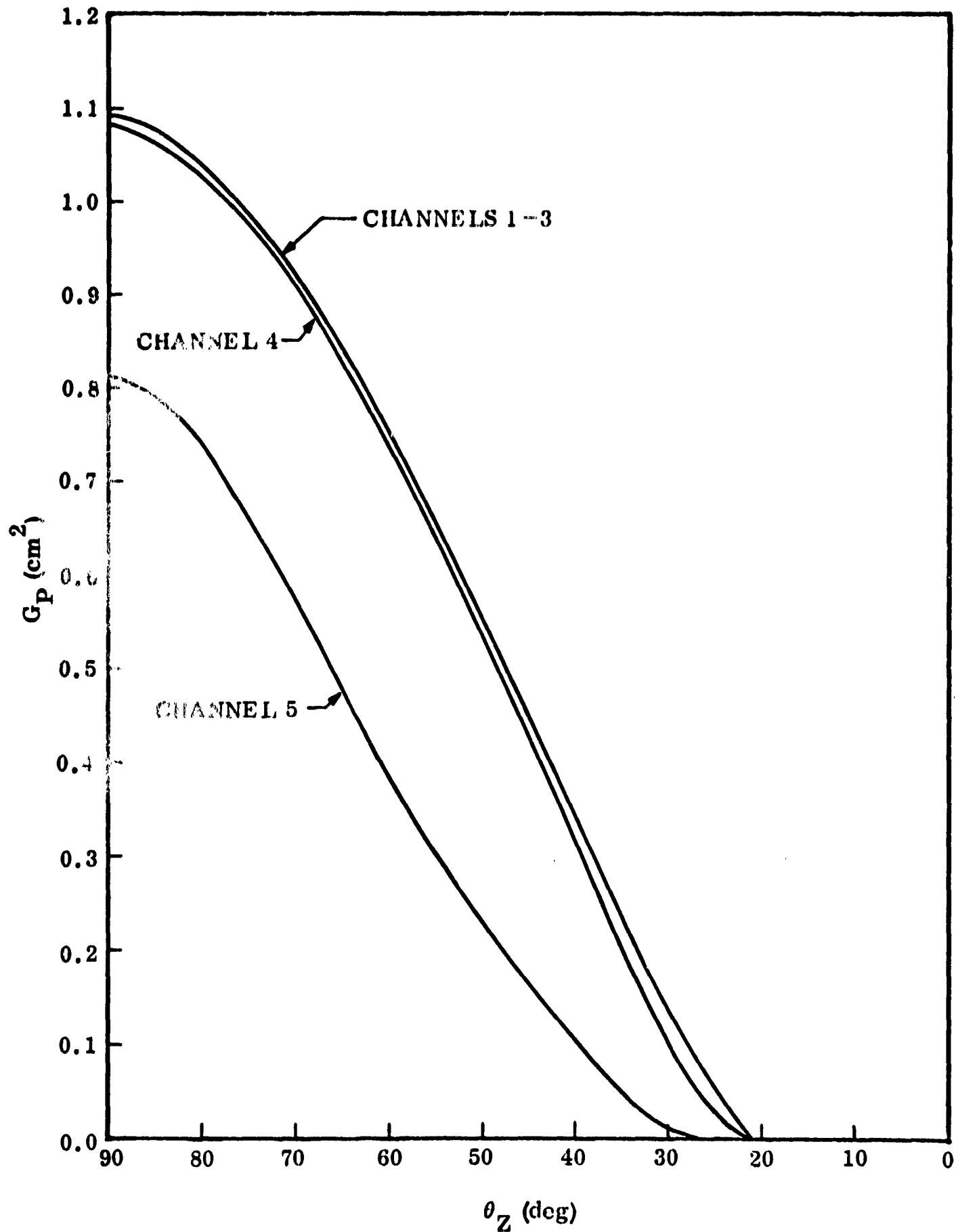
Figure 20   Proton Geometric Factors as a Function of the Orientation Angle, θ_Z, for the Five Energy Channels of the Gemini IV Spectrometer.

other hand, the geometric factor for the cylinder in a pancake-flux distribution displays a small angular effect. Figure 21 shows the geometric fa   r for this detector versus orientation angle, θ_z, as calculated for both types of flux distribution. The geometric factor curve for a pancake-flux distribution was used for subsequent calculations since it more nearly represents conditions in this region of B,L space.

In the Gemini VII spectrometer, the overload channel in the electron mode of operation functioned as an effective omnidirectional threshold detector. The measured energy spectrum in this mode showed that electron contribution ceased several channels below the overload channel. The overload channel counting rate was therefore exclusively associated with penetrating protons which deposited the equivalent of approximately 10 MeV of energy in the main scintillator. The geometry of the Gemini VII spectrometer and hence the geometric factor was considerably more complex than for the Gemini IV spectrometer. Figure 22 shows the calculated geometric factor as a function of incident proton energy for a pancake-flux distribution. The threshold energy, E_o, of the detector has been taken as the approximate midpoint of the efficiency curve and has a value of 100 MeV.

4.3.3 Computer Output

With the determination of the orientation angle, θ_z, and the subsequent calculations of the geometric factors, the computer program proceeds to calculate the various omnidirectional fluxes and differential spectra. A sample of the final computer output for the Gemini IV data is shown in Figure 23. The ephemeris data, B,L values, inclination, declination, minimum altitude and orientation angle are listed across the top of the output. The next line contains the raw electron counting rate data as well as the final omnidirectional electron flux. On subsequent lines the pulse-height analyzer content for each channel is listed along with the normalized counting rate. The statistical errors, based on the number of raw counts in each channel of the analyzer, are shown in the next column. These statistics have been carried throughout the subsequent calculations to provide an indication of the accuracy associated with the final differential spectra. The next column shows the net counting rate after the thorium background is subtracted. In the Gemini VII data, the additional cosmic ray background is subtracted as a function of L location as explained in an earlier section. The next column shows the effective geometric
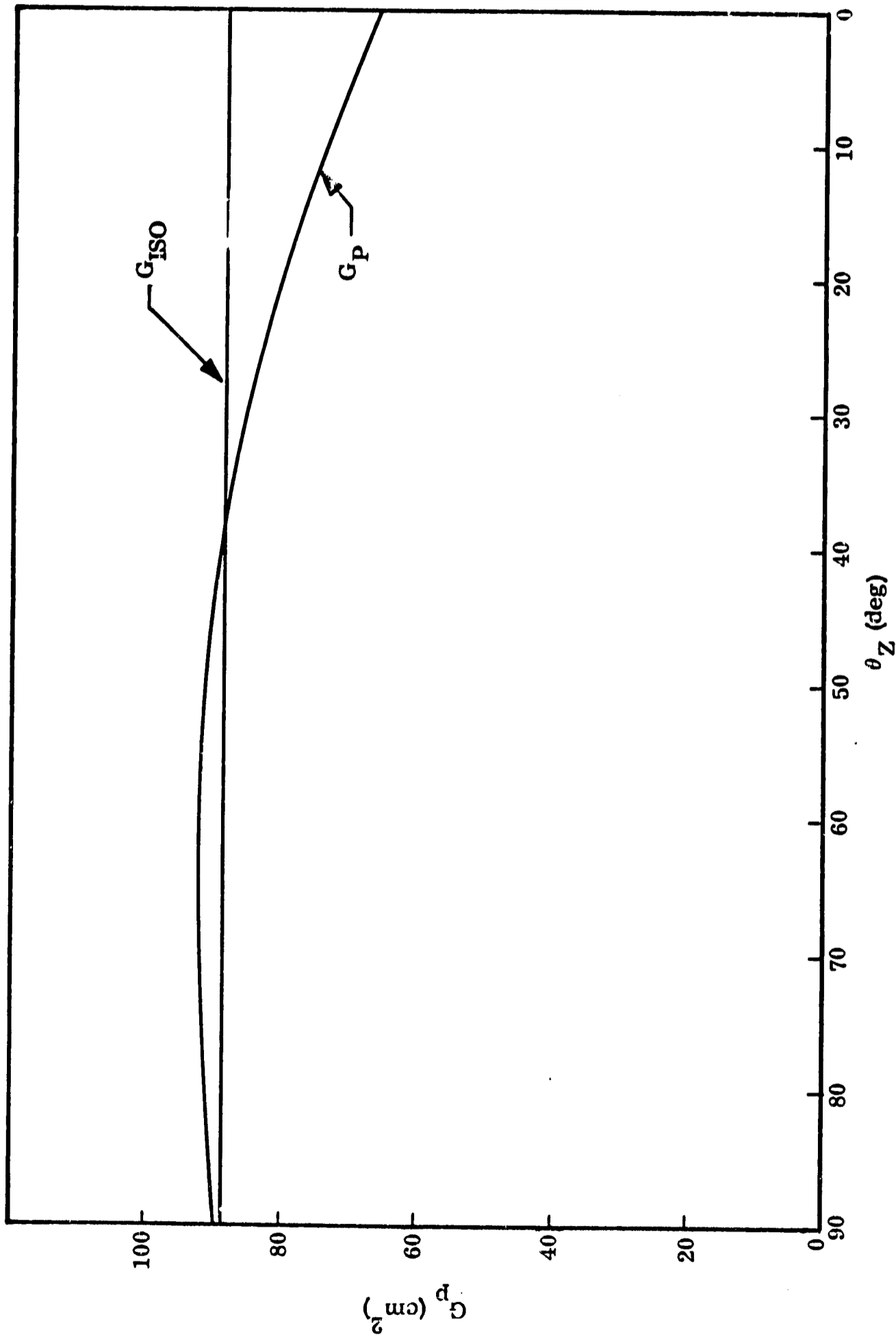
Figure 21 Proton Geometric Factor for the Gemini IV Anticoincidence Detector as a Function of the Orientation Angle, θ_Z. The Geometric Factor is Shown for Both Isotropic and Pancake-Flux Distributions.
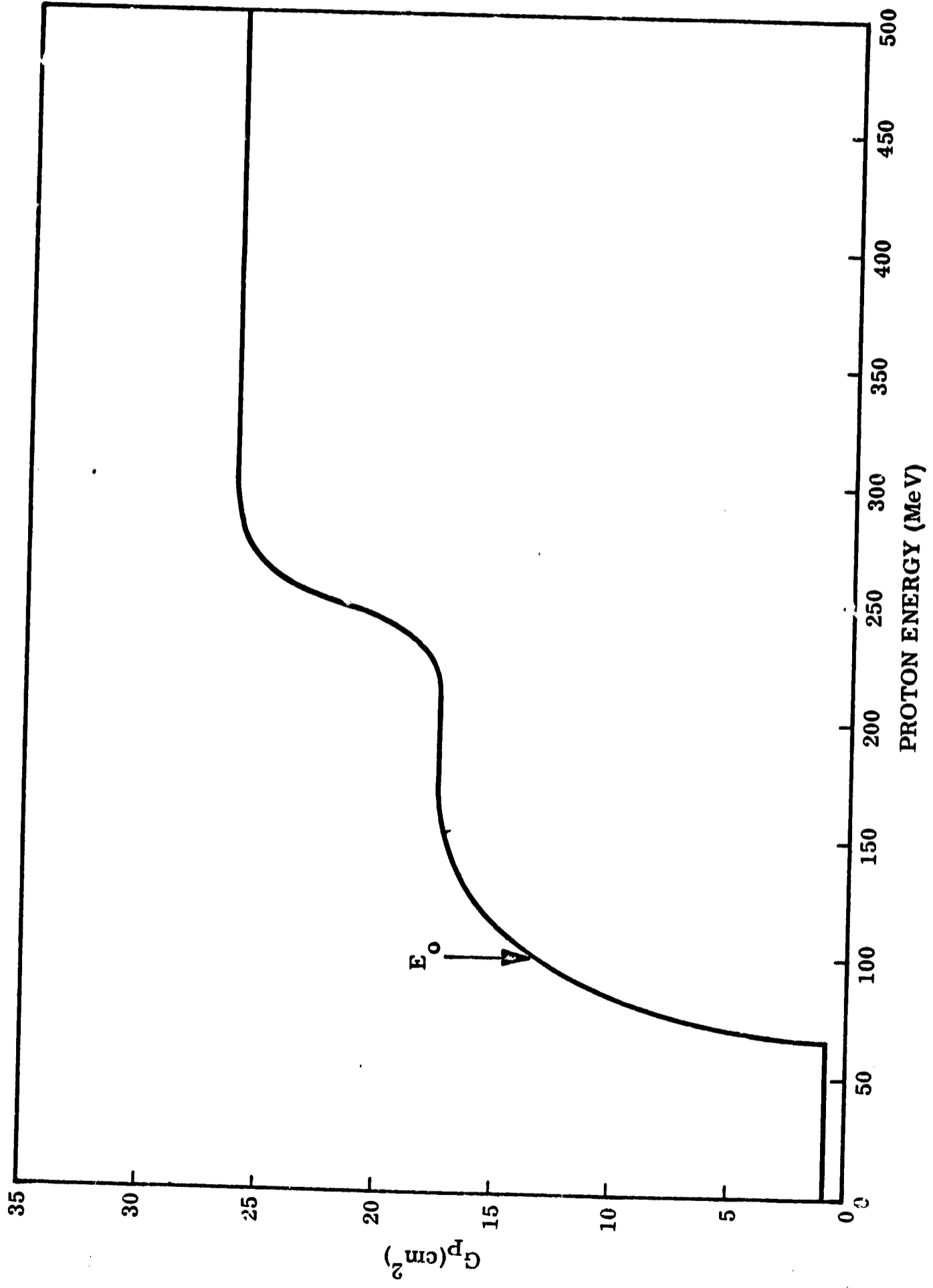
Figure 22 Calculated Geometric Factor for the Gemini VII Omnidirectional Proton Detector as a Function of Proton Energy for a Pancake-Flux Distribution.

	TIME										
HR MIN SEC	SEC	ALT	LAT	LONG	R	L	INC	DEC	H-9-W	T7	
55 35 50	200150.	272.690	-31.480	342.810	.24101	1.466	50.73	-25.02	272.5	89.77	

CRE = .739+04 COUNTS/SEC   OMNIDIRECTIONAL ELECTRON FLUX >0.45MEV = .652+04 ELECTRANS/CM2-SEC

CH NO	ENERGY MEV	AE MEV	RAW CTS	NORMALIZED COUNTS/SEC	NFT COUNTS/SEC	GF CM2	KF	DIFFERENTIAL FLUX ELEC/CM2-SEC	DIFFERENTIAL FLUX ELEC/CM2-SEC-MEV
1	.45-1.04	.59	102.	.227+04	.225+04	1.144	.051	.333+04	.340+03
2	1.04-1.63	.59	86.	.195+04	.195+04	1.114	.027	.297+04	.357+03
3	1.63-2.21	.59	65.	.144+04	.144+04	1.107	.014	.221+04	.380+03
4	2.21-2.80	.59	39.	.866+03	.864+03	1.104	.011	.132+04	.225+03
5	2.80-3.39	.59	15.	.333+03	.333+03	1.109	.016	.509+03	.134+03
6	3.39-3.98	.59	8.	.178+03	.177+03	1.106	.013	.272+03	.974+02
7	3.98-4.57	.59	4.	.988+02	.887+02	1.093	.000	.139+03	.693+02
8	4.57-5.15	.59	7.	.155+03	.155+03	1.093	.000	.241+03	.921+02
9	5.15-5.74	.59	1.	.222+02	.221+02	1.093	.000	.347+02	.341+02
10	5.74-6.33	.59	0.	.000	-.700-01	1.093	.000	.000	.000
11	6.33-6.92	.59	1.	.222+02	.222+02	1.093	.000	.344+02	.345+02
12	6.92-7.51	.59	0.	.000	-.600-01	1.093	.000	.000	.000
13	7.51-8.09	.59	0.	.000	-.300-01	1.093	.000	.000	.000
14	8.09-8.68	.59	0.	.000	-.300-01	1.093	.000	.000	.000
15	8.68-	.59	3.	.666+02	.661+02	1.093	.000	.103+03	.599+02
TOTAL			333.	.739+04	.736+04				

CRP COUNTS/SEC	TAC COUNTS/SEC	GAC 89.96 CM2
.620+01	.148+04	

OMNIDIRECTIONAL FLUX
23.5 -80MEV = .486+01 (PROTONS/CM2-SEC)   >64 MEV = .165+02 (PROTONS/CM2-SEC)

CH NO	ENERGY MEV	AE MEV	RAW CTS	NORMALIZED COUNTS/SEC	NFT COUNTS/SEC	GP CM2	KP	DIFFERENTIAL FLUX PROTONS/CM2-SEC-MEV	DIFFERENTIAL FLUX PROTONS/CM2-SEC-MEV
1	23.5 -35.0	11.5	20.	.197+01	.505-00	1.255	.163	.136-00	.350-01
2	35.0 -46.0	11.0	13.	.128+01	.390-00	1.157	.065	.101+00	.304-01
3	46.0 -57.0	11.0	10.	.984-00	.335-00	1.116	.024	.802-01	.273-01
4	57.0 -68.3	11.3	2.	.118+01	.372-00	1.104	.022	.946-01	.298-01
5	68.3 -79.6	11.5	2.	.197-00	.141-00	1.038	.027	.204-01	.147-01
6	79.8 -90.8	11.0	6.	.590-00	.146		.004	.369-0.	.157-00
TOTAL			63.	.620+01	.252-00				

Figure 23   A Sample of the Computer Output Listing for the Gemini IV Data

factor for each channel. These values include the calculated geometric factor plus the small quantity, k, explained earlier. The actual values of k for each energy channel are shown in the next column. Finally, the resulting differential flux is presented along with the associated statistics in the last two columns.

The proton data for the same time interval are shown below the electron data. The only background present in this mode of operation was from penetrating particles or gamma rays which did not generate an anticoincidence. This small background was obtained in the same manner as the penetrating background in the electron mode. The counting rate and spectrum associated with orientations beyond the geometrical cutoff were compared with acceptable orientations at the same B,L position in space. The overall net effect of this background on the integral omnidirectional flux amounted to approximately 6.5 percent. The individual values of k for each energy channel are shown in the listing. The quantity TAC represents the singles counting rate from the anticoincidence detector. No background was evident in this detector. The geometric factor for this detector and the resulting omnidirectional flux of protons above 64 MeV are shown.

The above information, which was stored on magnetic tape, was then sorted in the computer by L shell to provide the fluxes and spectra in intervals of 0.005 in L value.

Section 5

RESULTS

5.1 Omnidirectional Fluxes

5.1.1 Electron Fluxes

The omnidirectional fluxes of electrons above 0.45 MeV and 0.56 MeV have been obtained from the Gemini IV and VII spectrometers respectively, as a function of B value on specific L shells. There was a sufficient quantity of data in each experiment to warrant the sorting of the data into consecutive L-shell intervals of 0.005. For clarity of presentation, the data have been plotted in increments of 0.025 only, with the L interval at each incremental value being $\pm$ 0.0075. For example, the omnidirectional flux as a function of B-value on the nominal L shell of 1.200 represents data gathered from the L-interval of $1.1925 \leq L \leq 1.2075$. The omnidirectional fluxes in electrons/cm^2-sec, above 0.45 MeV, as measured with the Gemini IV spectrometer in June 1965, are shown in Figure 24. The solid lines are best-fit curves through the available data. The envelope of the curves reflects the trajectory of the spacecraft in B,L space through the anomaly region. The lowest B-values were encountered primarily at low L-shells and the highest B values were encountered on the highest L-shells. The omnidirectional flux of electrons above 0.56 MeV, which was measured with the Gemini VII spectrometer in December 1965, is shown in Figure 25 as a function of B-value. It is evident from both of these figures that a broad range of fluxes have been measured with these spectrometers and because of the high sensitivity available, flux levels as low as a few electrons/cm^2-sec have been obtained.

The above data have been used to generate flux contours in B-L space. Figures 26 and 27 show the contours that result for the omnidirectional electron flux in June 1965 and December 1965, respectively. The solid circles represent points obtained from the curves of Figures 24 and 25. Best-fit curves have been generated through the resultant points. Very little scatter exists and smooth contour lines easily describe the experimental data. Also shown in Figures 26 and 27 is the contour line in B-L space that describes a minimum altitude of 100 km. Particle trajectories, encountering B,L values above this line reach altitudes lower than this value somewhere in their trajectory. It is evident
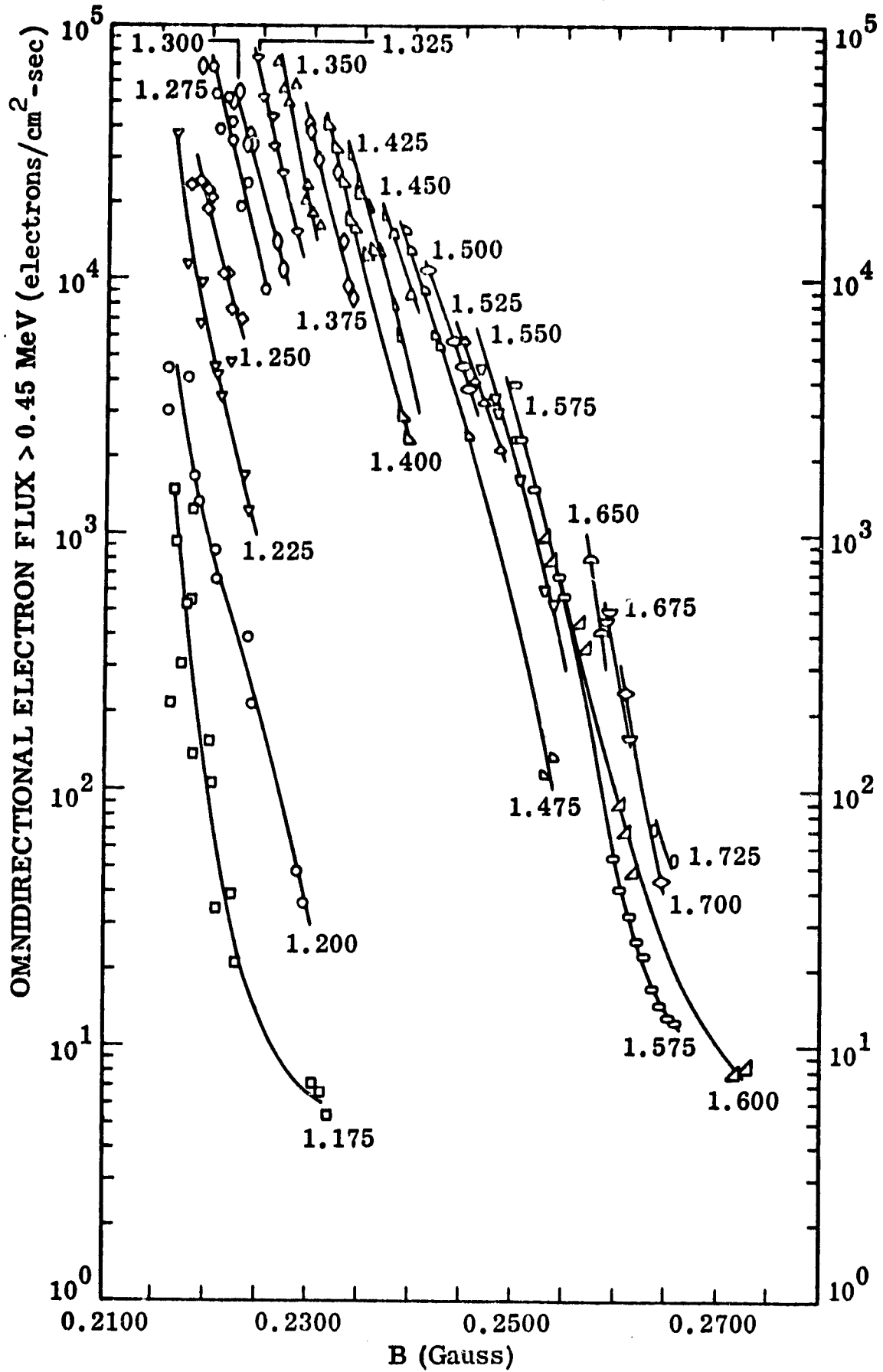
Figure 24   Omnidirectional Flux of Electrons > 0.45 MeV
as a Function of B-Value on Specified L-Shells
as Measured with the Gemini IV Spectrometer in
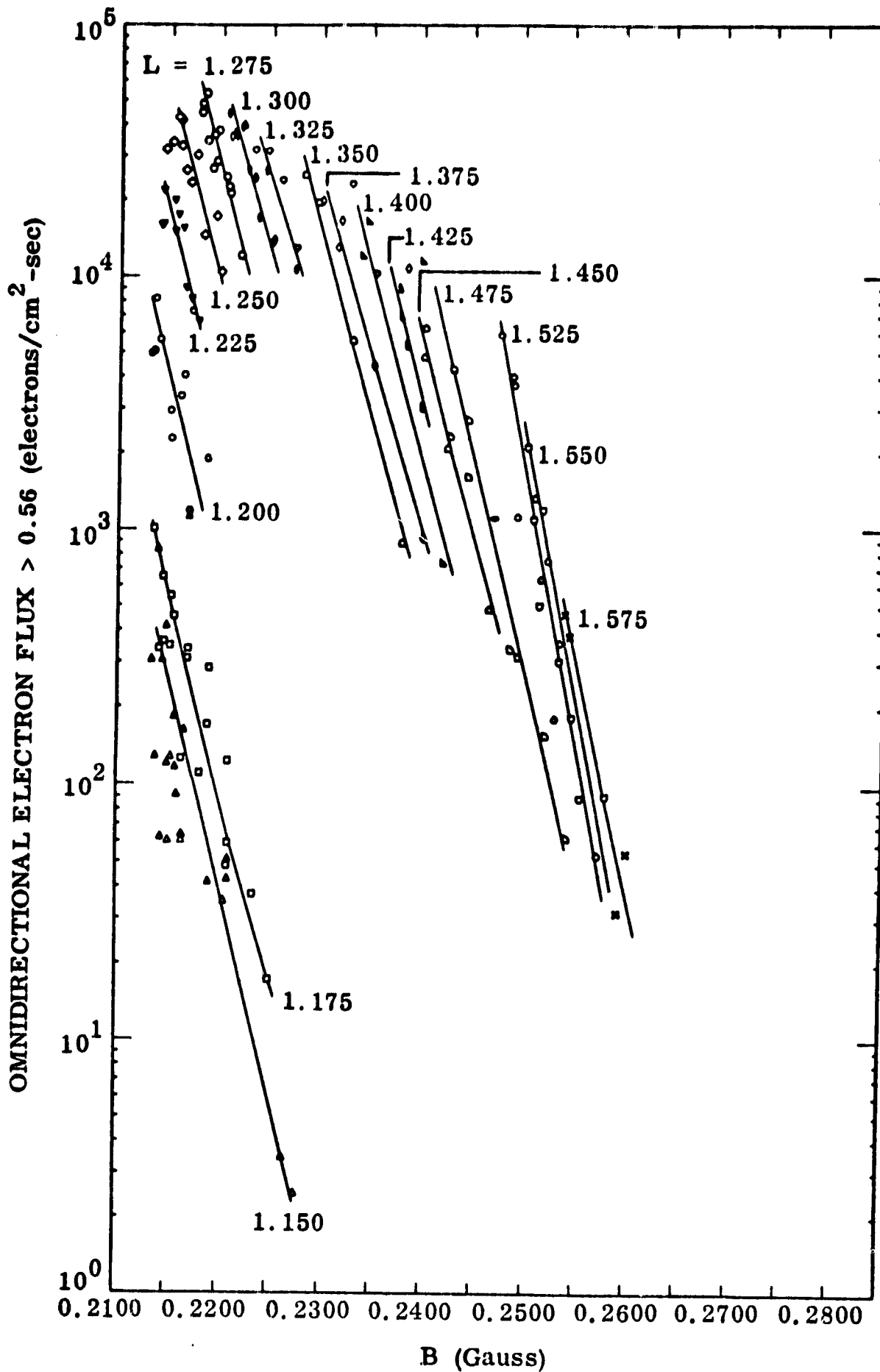June 1965.

46

Figure 25 Omnidirectional Flux of Electrons > 0.56 MeV as a
Function of B-Value on Specific L-Shells as Meas-
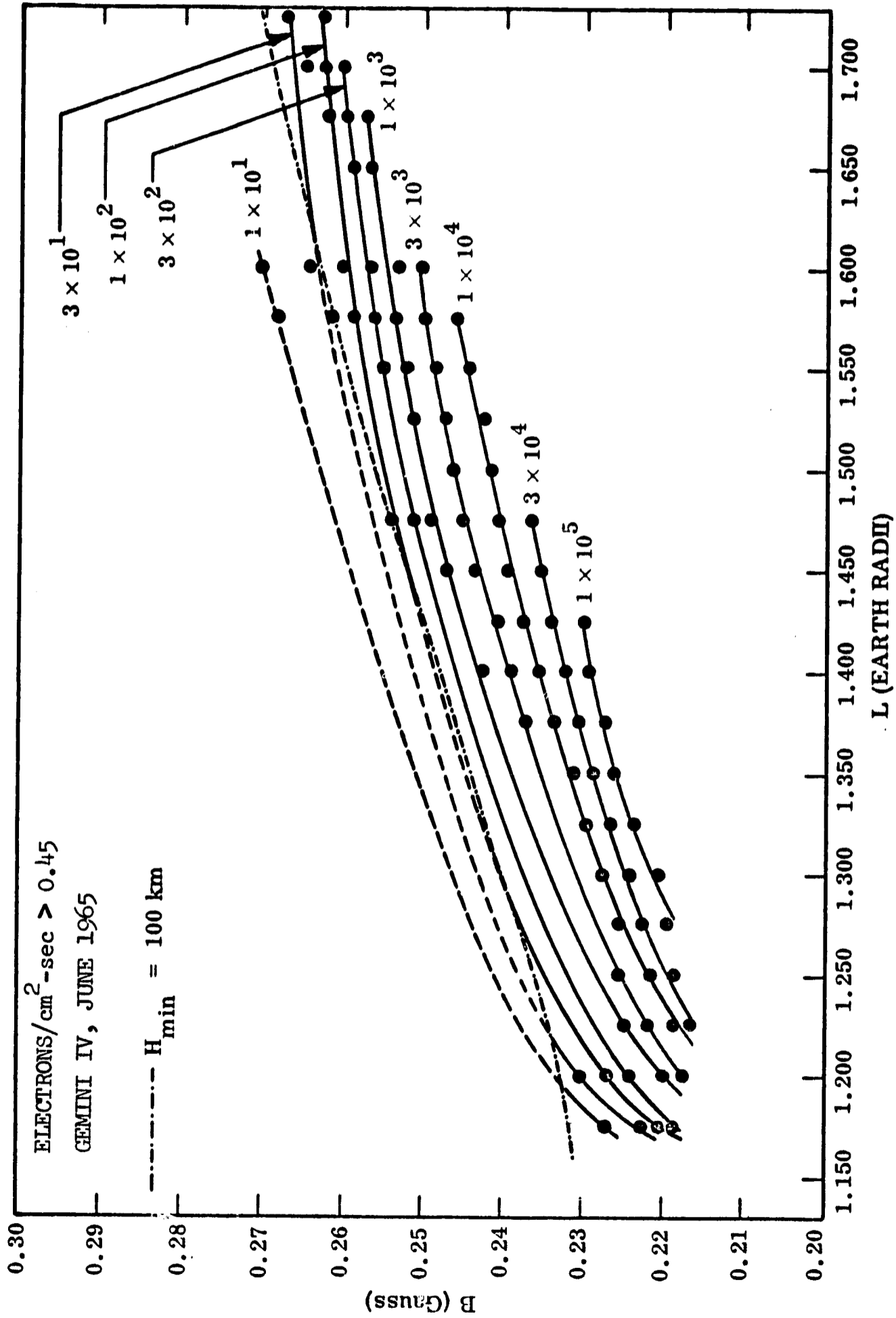ured with the Gemini VII Spectrometer in December
1965.

Figure 26   Flux Contours in B-L Space of the Omnidirectional Flux of Electrons > 0.45 MeV in June 1965.
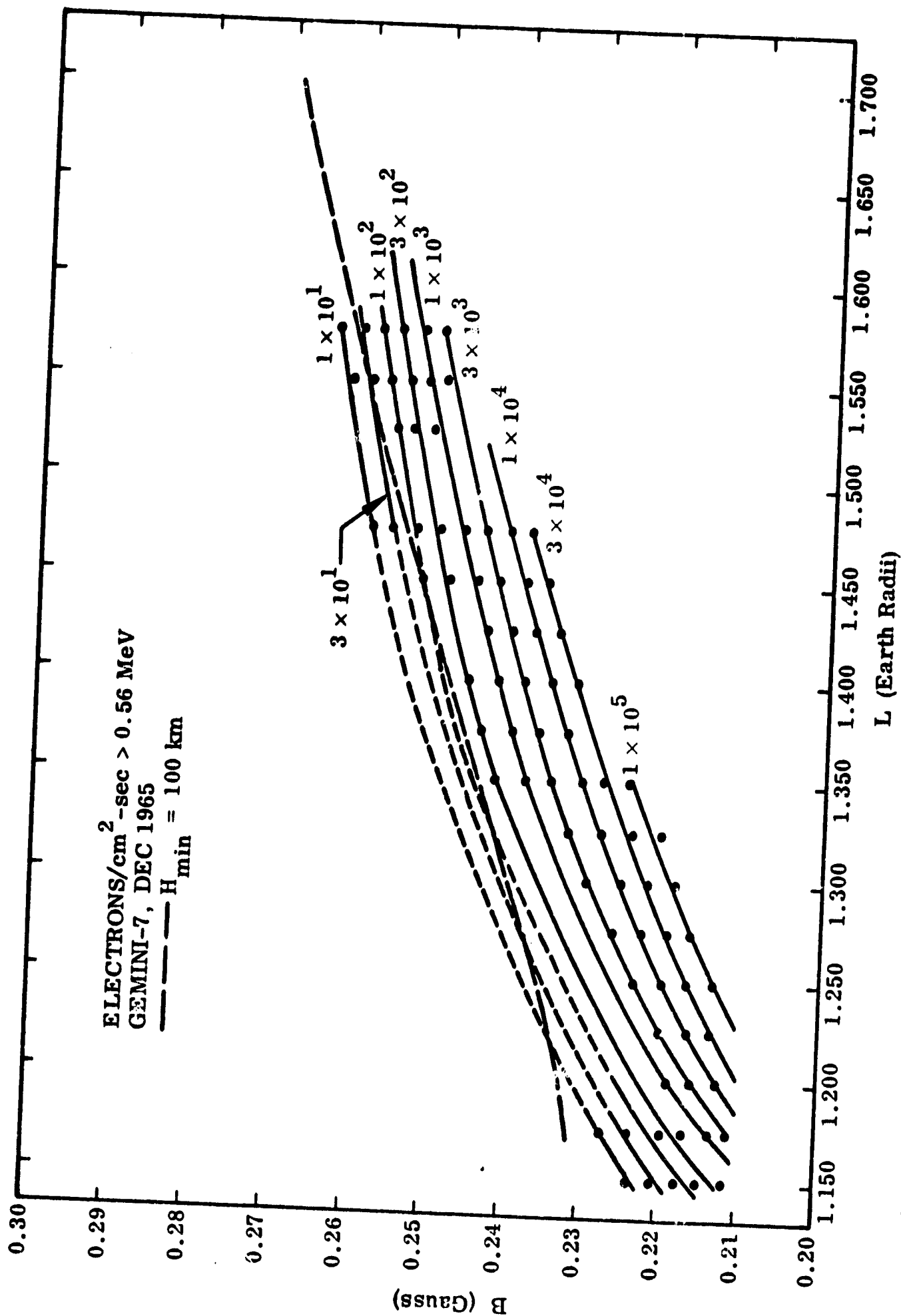
Figure 27 Flux Contours in B-L Space of the Omnidirectional Flux of Electrons > 0.56 MeV in December 1965.

from these two figures that electrons at flux levels of 10 and 30 electrons/cm^2-sec encounter minimum altitudes less than 100 km and are therefore presumably quasi-trapped or precipitating in this region.

5.1.2 Proton Fluxes

Omnidirectional fluxes of protons in the 23.5-80 MeV energy range and integral omnidirectional fluxes of protons above 64 MeV and approximately 100 MeV have been obtained from the Gemini IV and VII spectrometers.

Figure 28 shows the flux of protons in the 23.5-80 MeV energy range, as a function of B-value on specific L-shells, as measured in detail by the Gemini IV spectrometer. The two most evident features of the data are the low flux levels that were measured in this region and the steep dependence of the flux on B-value. Figure 29 shows the omnidirectional proton flux greater than 64 MeV that was measured with the same spectrometer. These higher energy flux data show a much less steep variation with B-value than the lower energy data shown in Figure 28. Finally, the proton flux greater than approximately 100 MeV, as measured with the Gemini VII spectrometer in December 1965, is shown in Figure 30. Once again, the flux levels measured are relatively low and do not show as steep a variation with B as the lower energy protons exhibit.

The resulting contours in B,L space of the various omnidirectional proton fluxes are shown in Figures 31, 32 and 33. Figure 31 shows the omnidirectional flux in the energy interval of 23.5-80 MeV as a function of B,L location. The resulting flux contours through the data points are smooth but extremely closely spaced in the higher L region as a result of the steep dependence on B. The equator and the minimum altitude of 100 km contour lines are also shown in this figure. In contrast to the electron flux contours, proton fluxes of intensity equal to or greater than 1 proton/cm^2-sec within this energy interval do not exist near or below minimum altitudes of 100 km. Figure 32 shows the B-L relationship of the omnidirectional proton flux above 64 MeV. The isoflux contours are more evenly spaced than those for the lower energy protons demonstrating a less severe dependence on B, particularly at the higher L values. Finally, Figure 33 shows the equivalent data for protons above approximately 100 MeV as measured in December 1965. These data also display a smoother dependence with B than the lower energy protons. It should be noted that these data were acquired with different spectrometers and at different epochs. The higher energy proton data from both spectrometers, however, agree quite well in shape and absolute flux intensity but both differ in isoflux shape from the lower energy protons at the higher L values.
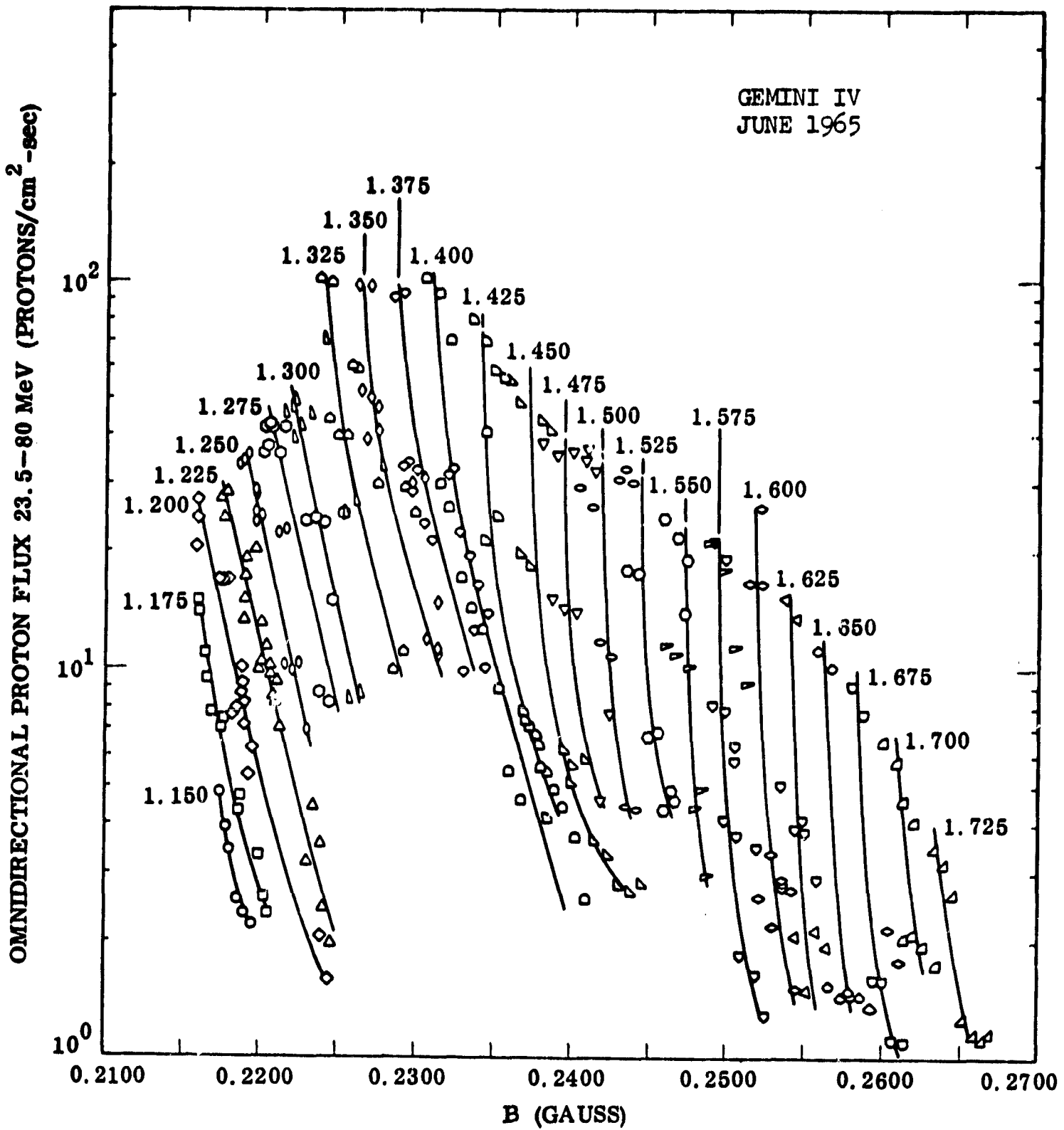
Figure 28 Omnidirectional Flux of Protons in the Energy Range 2.35-80
MeV as a Function of B-Value on Specific L-Shells as Meas-
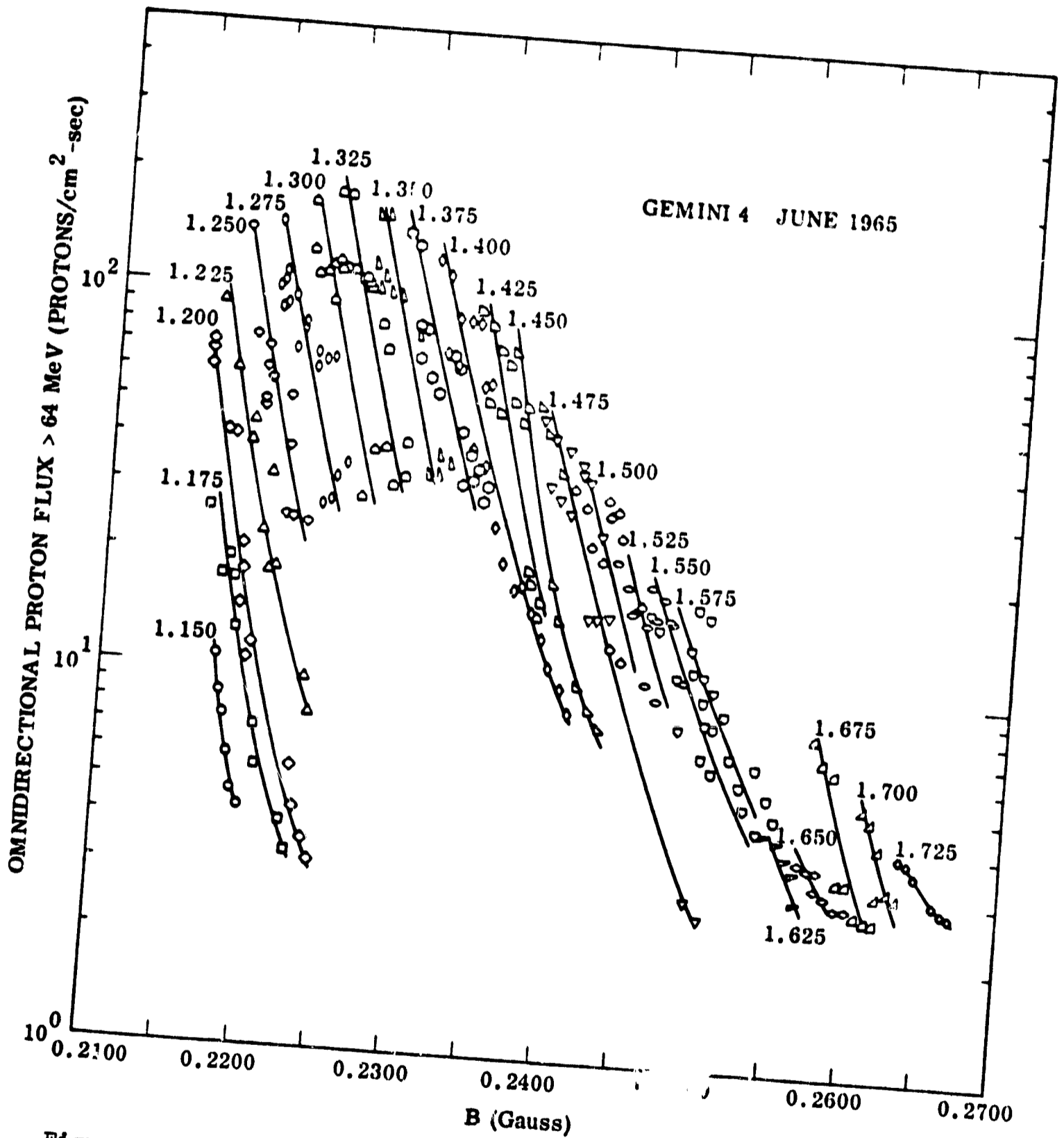ured in June 1965.

Figure 29   Omnidirectional Flux of Protons > 64 MeV as a Function of
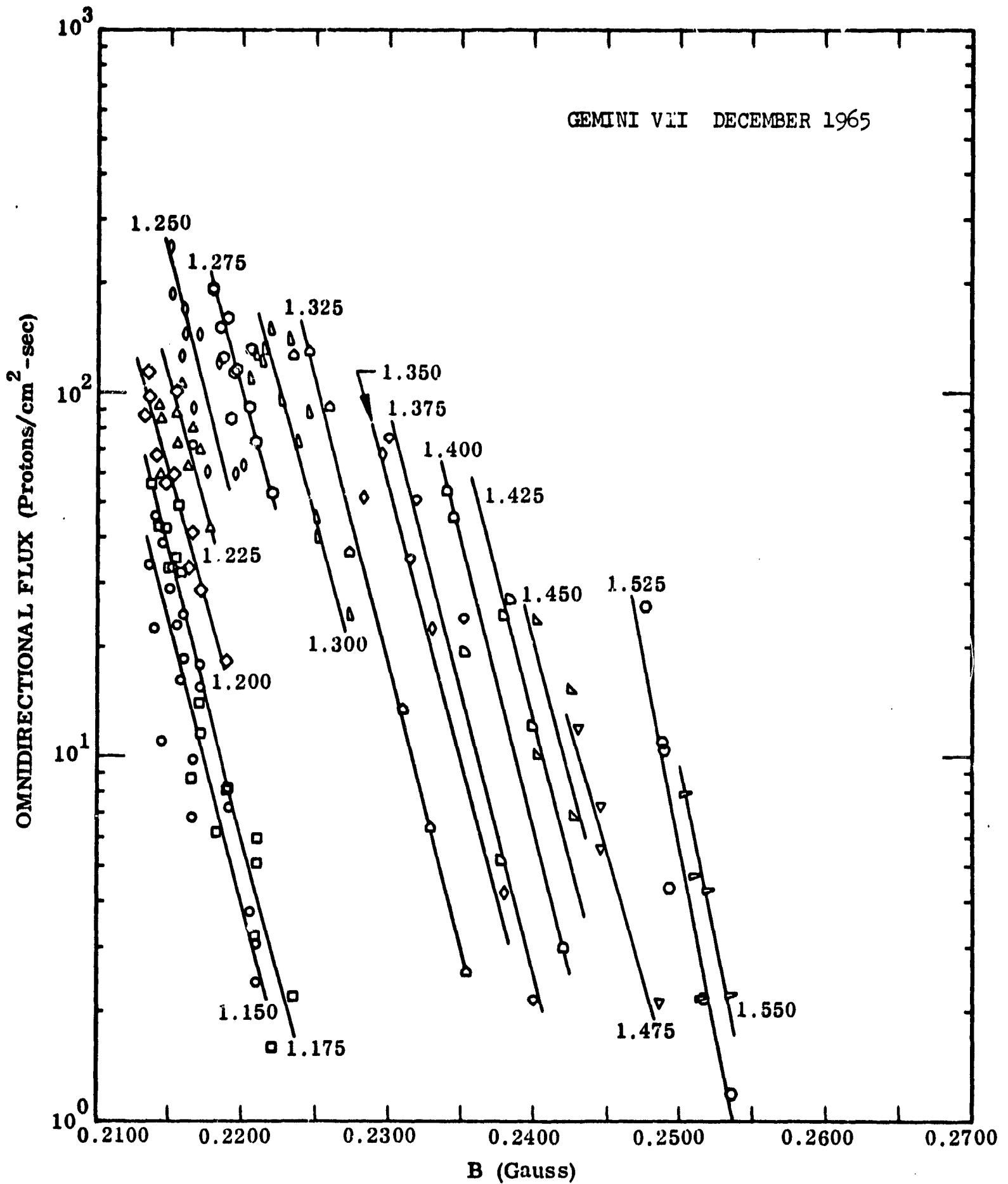B-Value on Specific L-Shells as Measured in June 1965.

Figure 30   Omnidirectional Flux of Protons Above Approximately 100 MeV as a Function of B-Value on Specific L-Shells as Measured in December 1965.
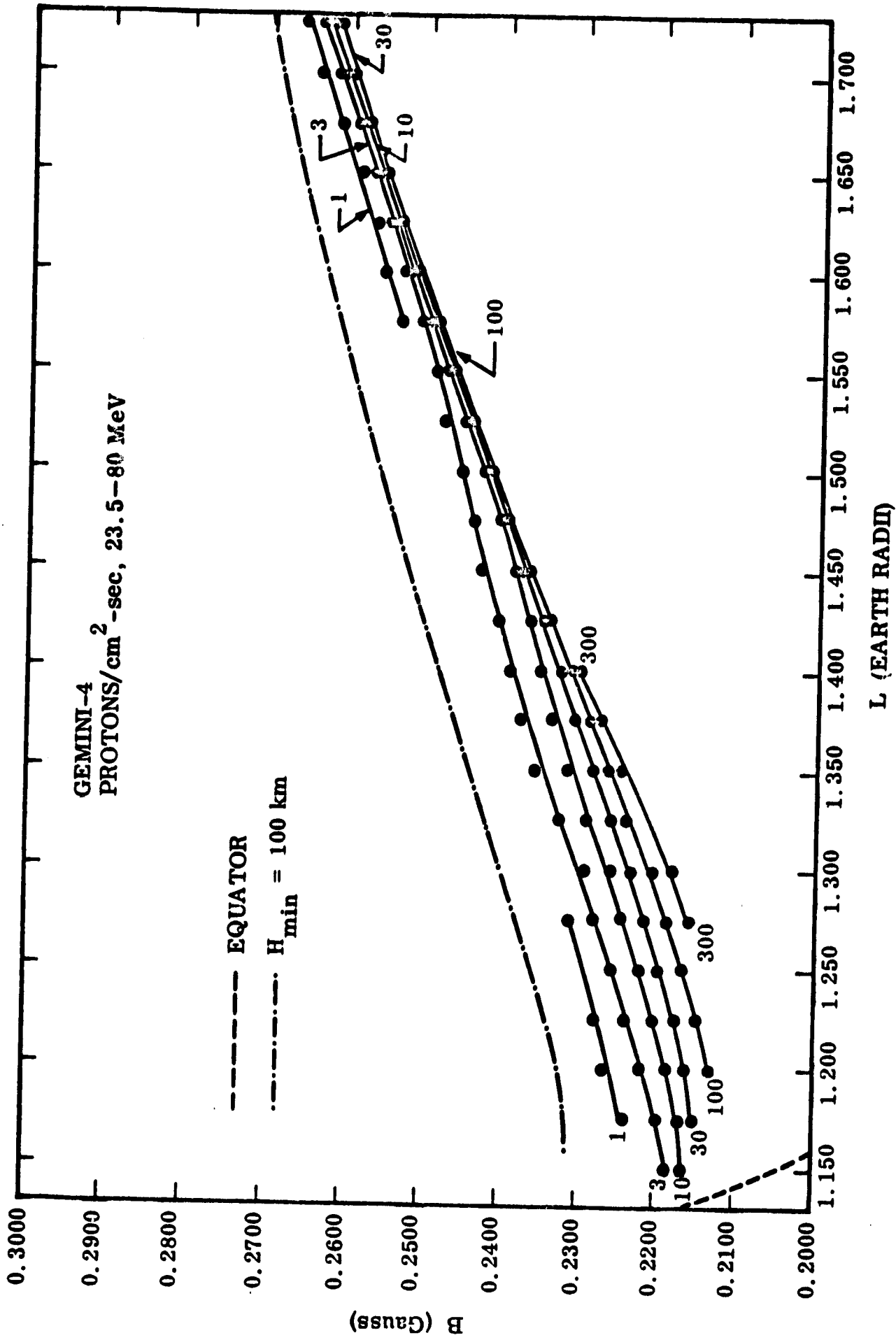
Figure 31 Flux Contours in B-L Space of the Omnidirectional Flux of Protons in the 23.5-80 MeV Energy Range as Measured in June 1965.
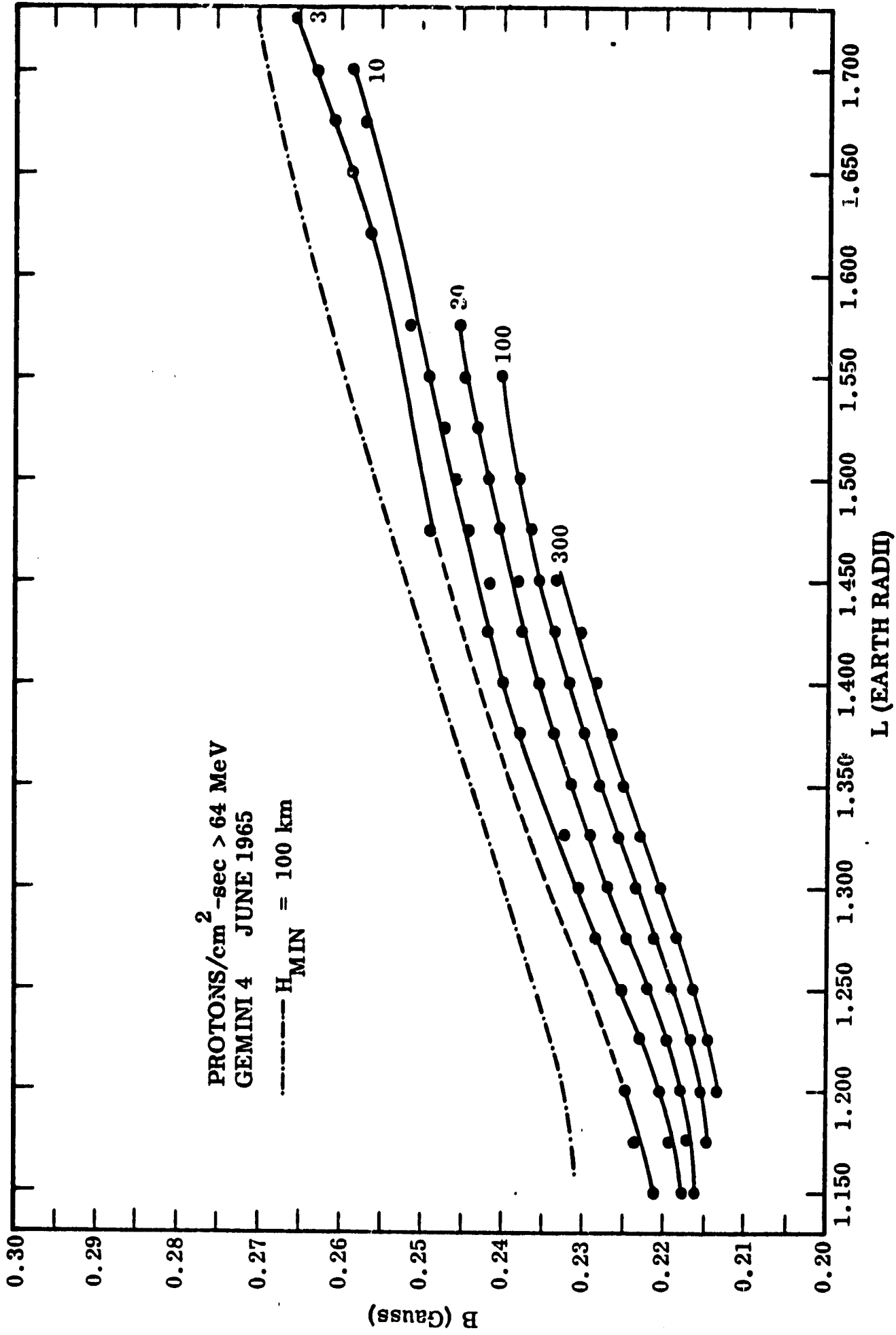
Figure 32 Flux Contours in B-L Space of the Omnidirectional Flux of Protons above 64 MeV as Measured in June 1965.
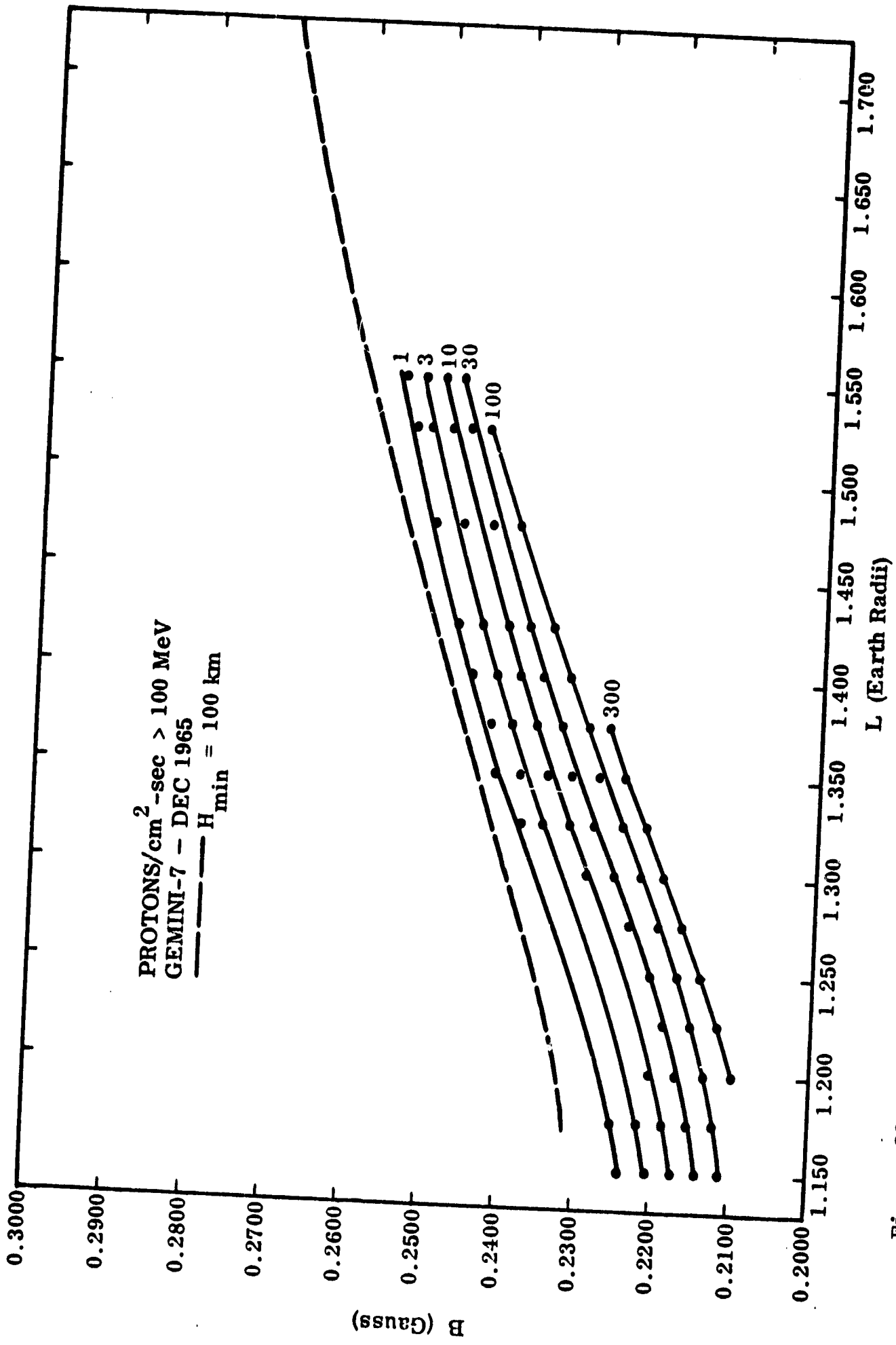
Figure 33 Flux Contours in B-L Space of the Omnidirectional Flux of Protons Above Approximately 100 MeV as Measured in December 1965.

5.2 Differential Spectra

5.2.1 Electron Spectra

As mentioned earlier, the differential electron spectrum was obtained for each data accumulation interval of approximately 16 seconds. The B-L values corresponding to the average time of each interval were assigned to the data. The statistical error associated with the number of counts in each energy channel of the spectrometer during this interval was calculated and appropriately applied during subsequent calculations. The initial assumption in treating the spectral data has been that the spectrum shape is independent of B to first order for h_{min} > 100 km and dependent only on L. Except for the very lowest L-interval, the spectral shapes have been obtained at L values differing by 0.025, each with an acceptable data interval of ± 0.0075. There were sufficient significant data available to warrant this narrow L grouping. Figures 34, 35, 36, and 37 show the differential electron spectra above 0.45 MeV for the L interval 1.150 < L < 1.725 as obtained with the Gemini IV spectrometer in June 1965. The lowest energy point for each L value has been arbitrarily normalized to unity on the logarithmic ordinate scale so that the relative intensities shown are applicable only to individual L shells. It can be seen that the errors associated with the data are small and meaningful spectra were obtained out to 6 MeV in energy. In this presentation, best-fit curves have been applied to all of the data. In most cases, the overall data could not be fitted with a single exponential curve. The data could be approximated with two exponential curves above and below an approximate energy of 2 MeV.

In Figure 38, the electron spectra from several L shells have been overlapped and arbitrarily normalized to unity at the midpoint of the lowest energy channel. It can be seen that a significant variation in spectrum exists over this rather narrow L interval. The spectra on both the lowest L shell of 1.165 and the highest L shell of 1.700 are considerably softer than the spectra at the mid-L values near 1.300. The softer spectra presumably represent the presence of large fluxes of naturally ocurring electrons along with the remains of the fission-like electron belt created by the Starfish and Soviet high-altitude nuclear tests of 1962. The hardest spectra are observed between 1.275 ≤ L ≤ 1.375 indicating that in June 1965 the decaying artificial electron belt was centered near an L value of 1.325.
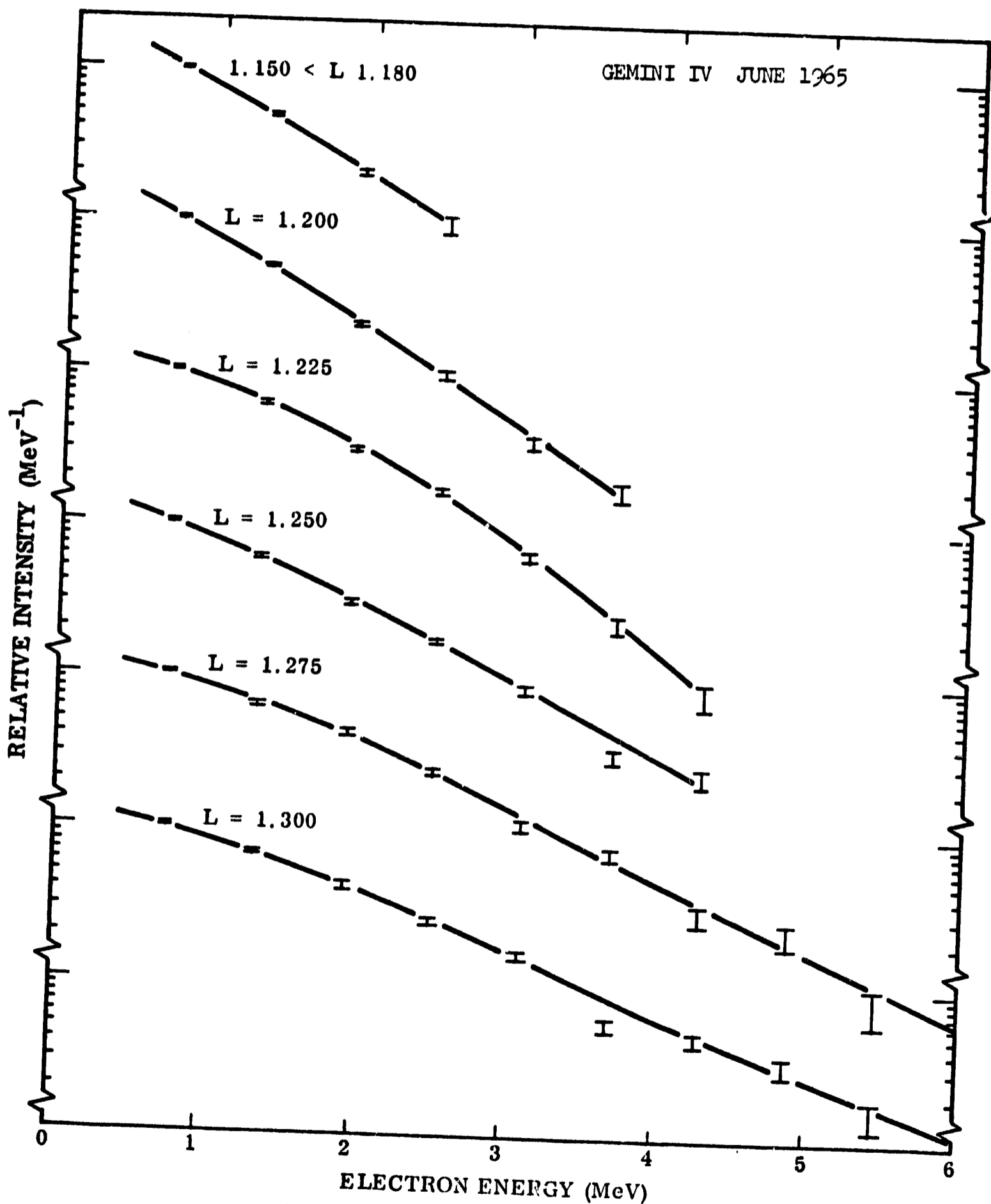
Figure 34   Differential Electron Spectra as a Function of L-Shell in the Interval $1.150 \leq L \leq 1.300$ for the Epoch June 1965.
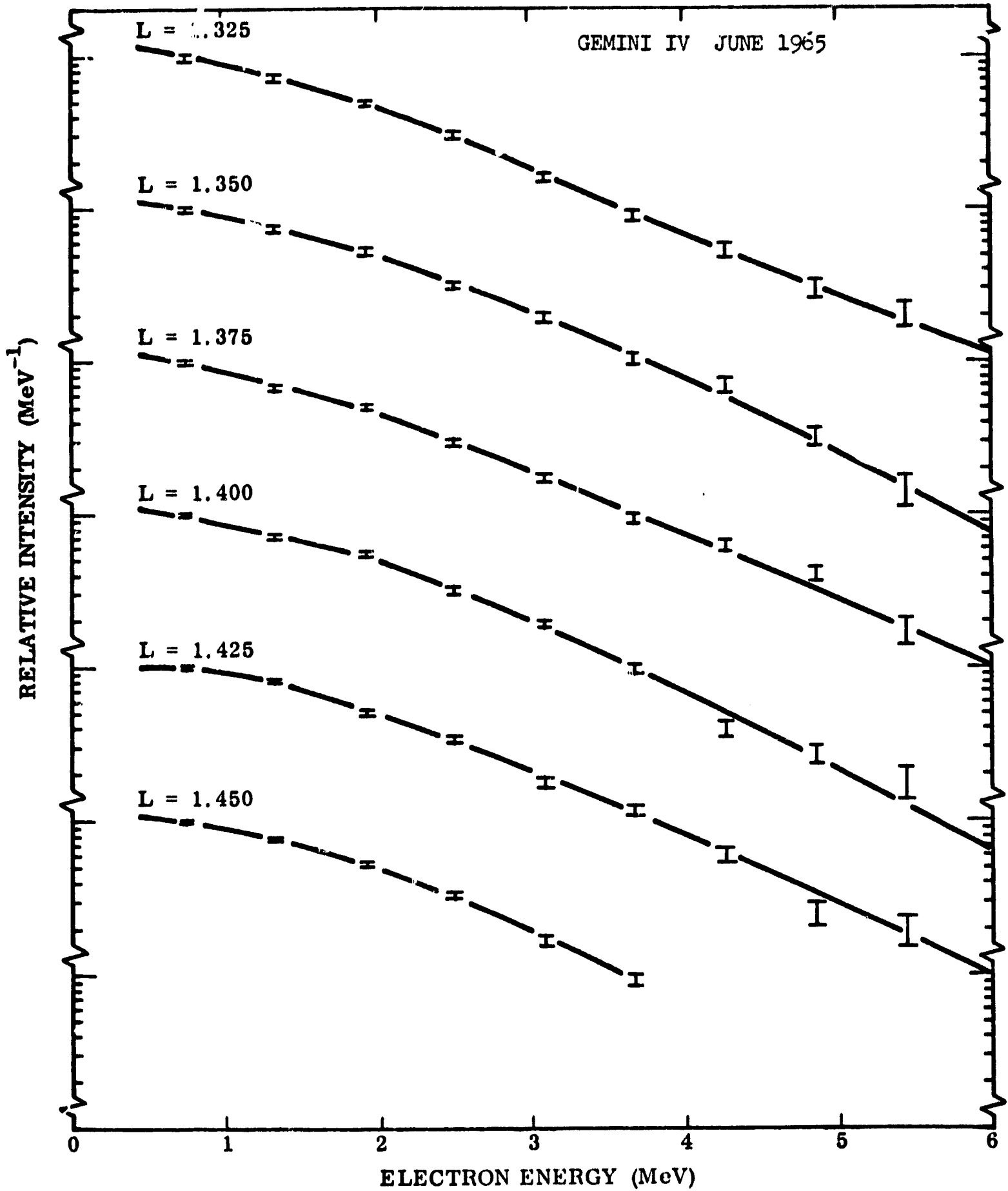
58

Figure 35   Differential Electron Spectra as a Function of L-Shell in the
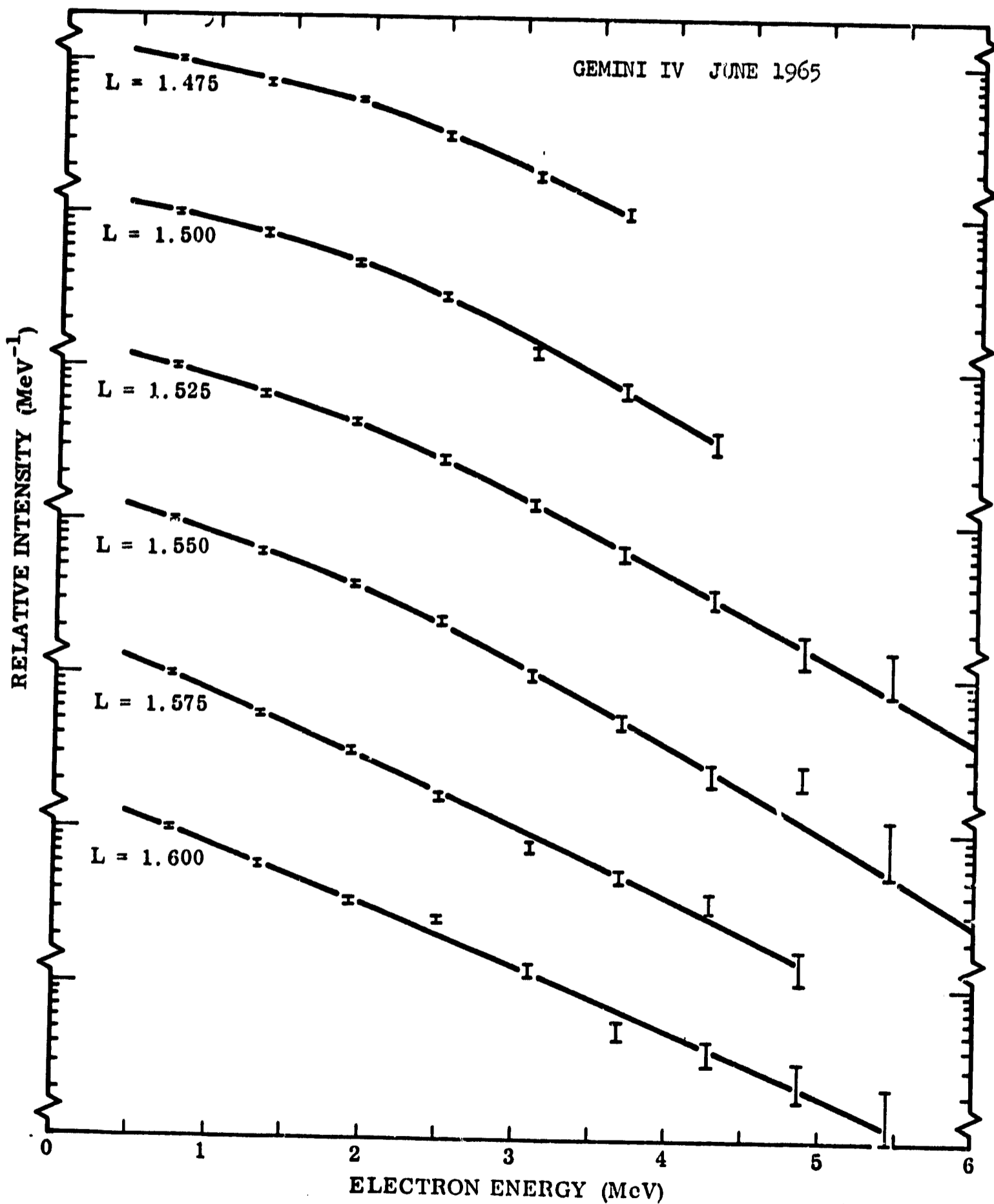Interval 1.325 ≤ L ≤ 1.450 for the Epoch June 1965.

Figure 36 Differential Electron Spectra as a Function of L-Shell in the
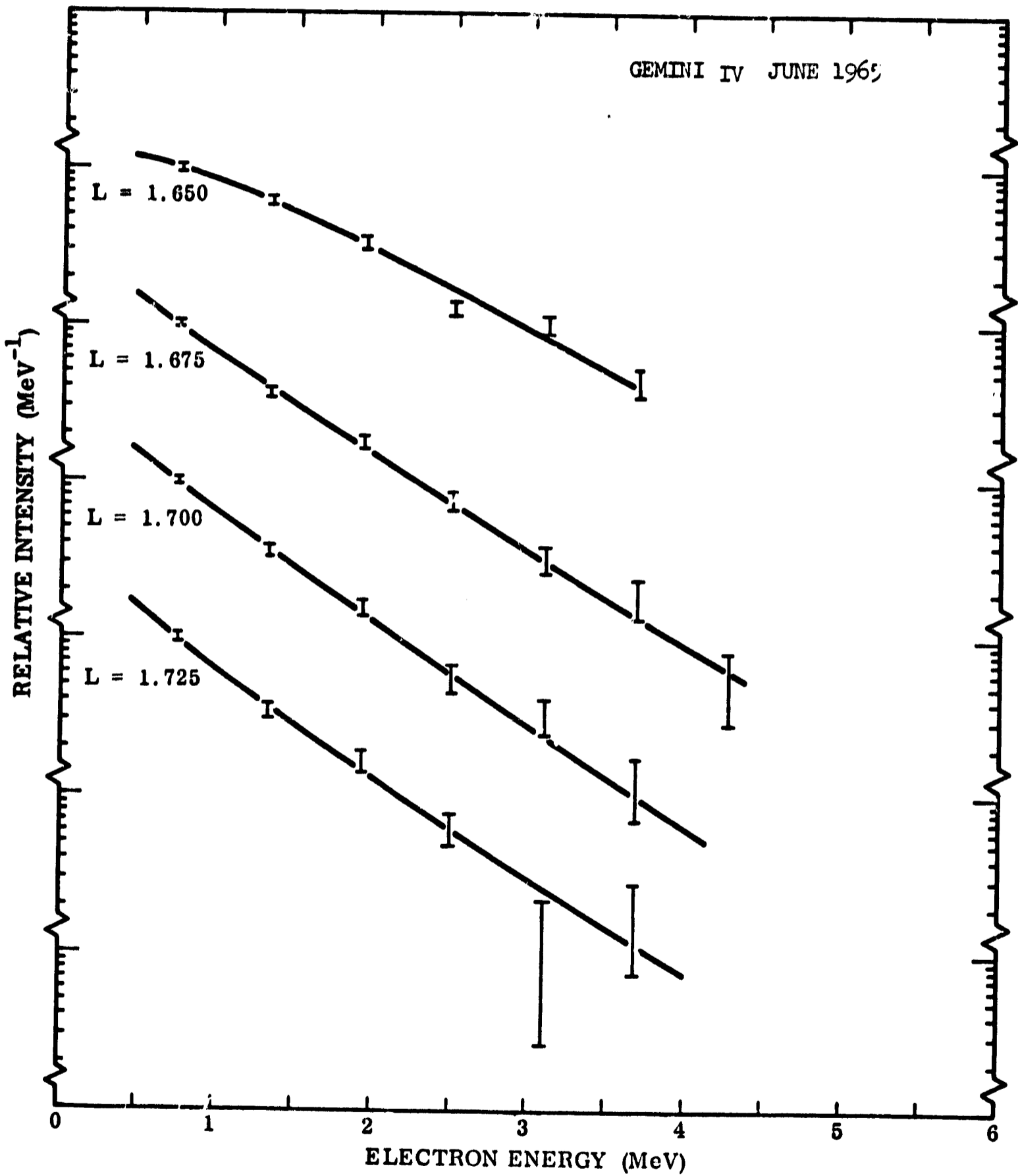Interval 1.475 ≤ L ≤ 1.600 for the Epoch June 1965.

Figure 37 Differential Electron Spectra as a Function of L-Shell in the
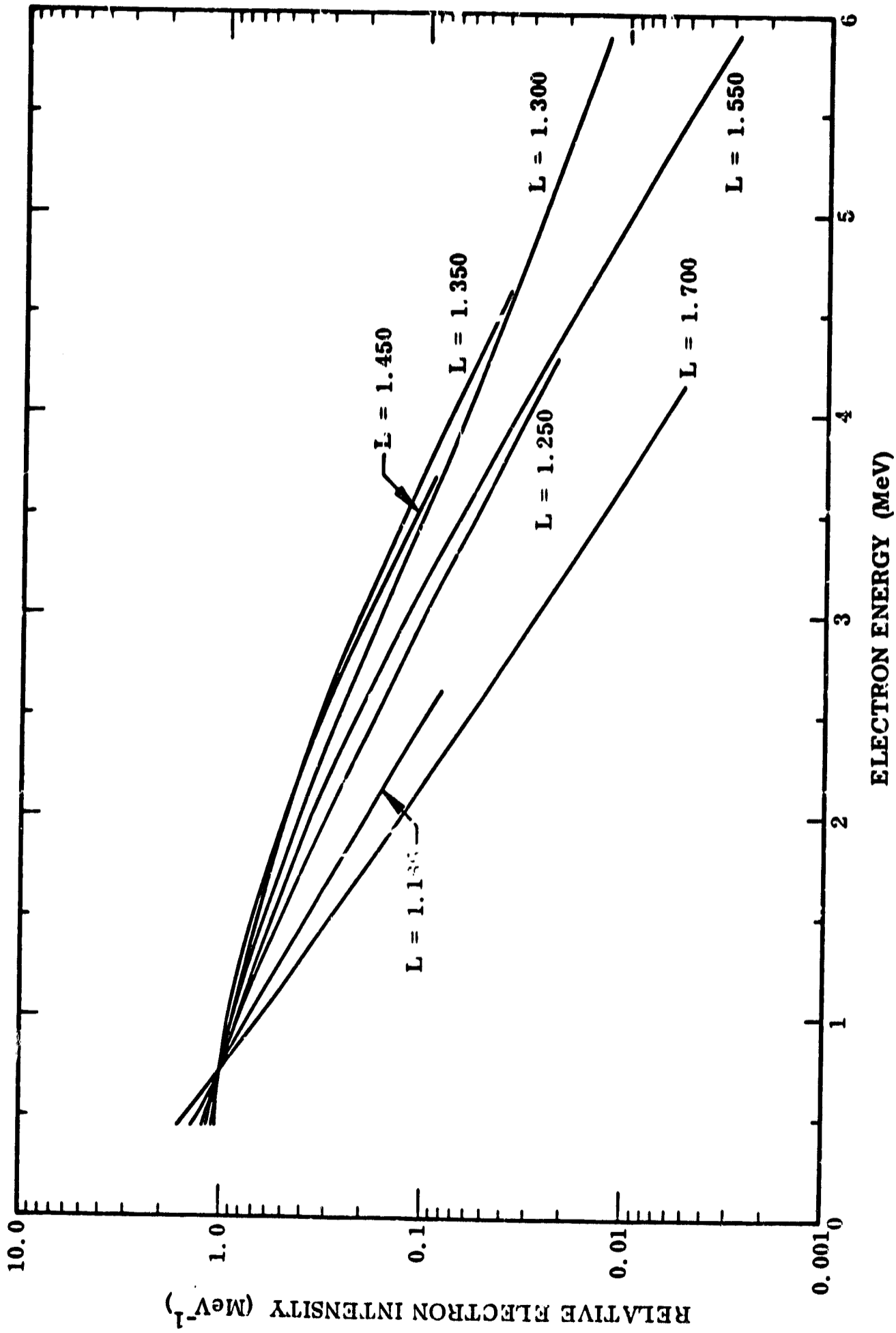Interval 1.650 ≤ L ≤ 1.725 for the Epoch June 1965.

Figure 38 Comparison of the Electron Spectra on Several L-Shells for the Epoch June 1965

Similar differential electron spectra have been generated for the Gemini VII data. Figures 39, 40 and 41 show these data over the L-interval of 1.175 ≤ L ≤ 1.525. Above approximately 2 MeV in energy, the Gemini IV and VII spectra agree quite well in shape. However, below this energy, the latter data show less tendency for the flux to rise with decreasing energy.

5.2.2 Proton Spectra

The omnidirectional proton spectra in the energy region 23.5-80 MeV are shown in Figures 42, 43, 44 and 45 as a function of L shell over the region 1.150 ≤ L ≤ 1.725. The spectra are characteristically quite hard with typical E_o energy parameters being in excess of 50 MeV in this region. The most pronounced feature of the data is the existence of a rather persistent broad peak centered at approximately 50 MeV in energy.
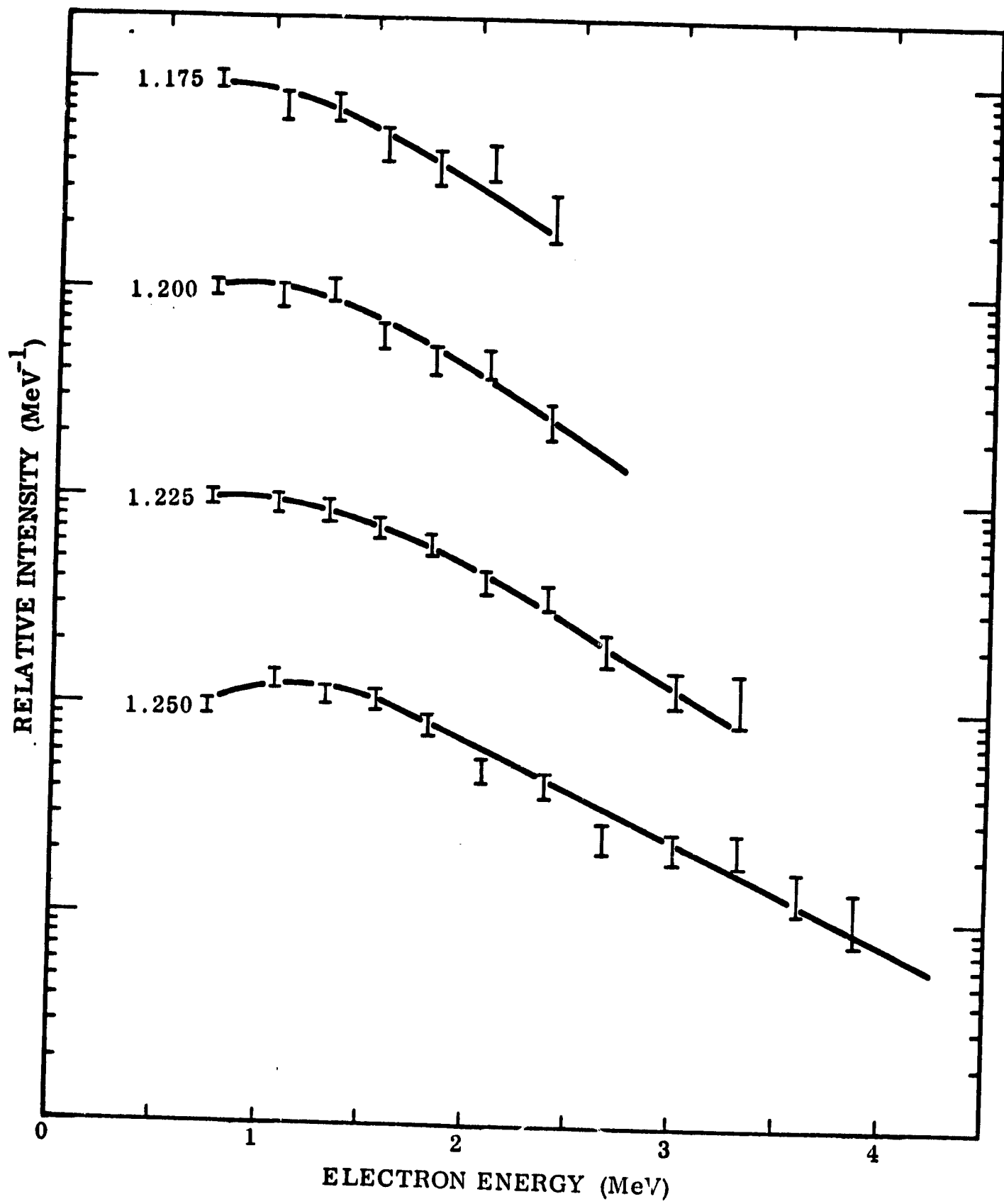
Figure 39 Differential Electron Spectra as a Function of L-Shell in the Interval $1.175 \leq L \leq 1.250$ for the Epoch December 1965.
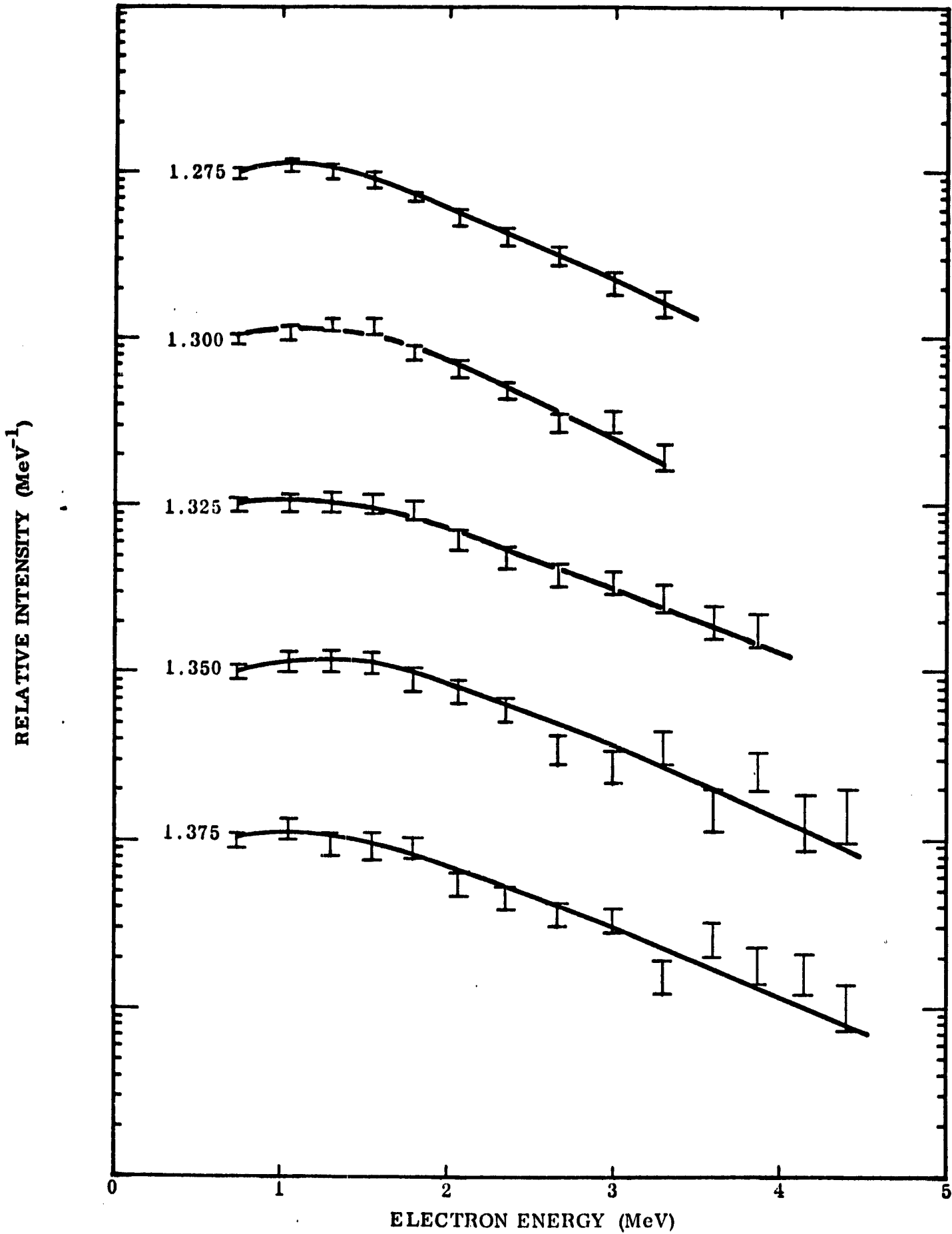
Figure 40 Differential Electron Spectra as a Function of L-Shell in the Interval $1.275 \leq L \leq 1.375$ for the Epoch December 1965.

Figure 41   Differential Electron Spectra as a Function of L-Shell in the
Interval $1.400 \leq L \ 1.525$ for the Epoch December 1965.

Figure 42   Differential Proton Spectra as a Function of L-Shell in the
Interval 1.150 ≤ L ≤ 1.300 for the Epoch June 1965

Figure 43 Differential Proton Spectra as a Function of L-Shell in the Interval $1.325 \leq L \leq 1.450$ for the Epoch June 1965
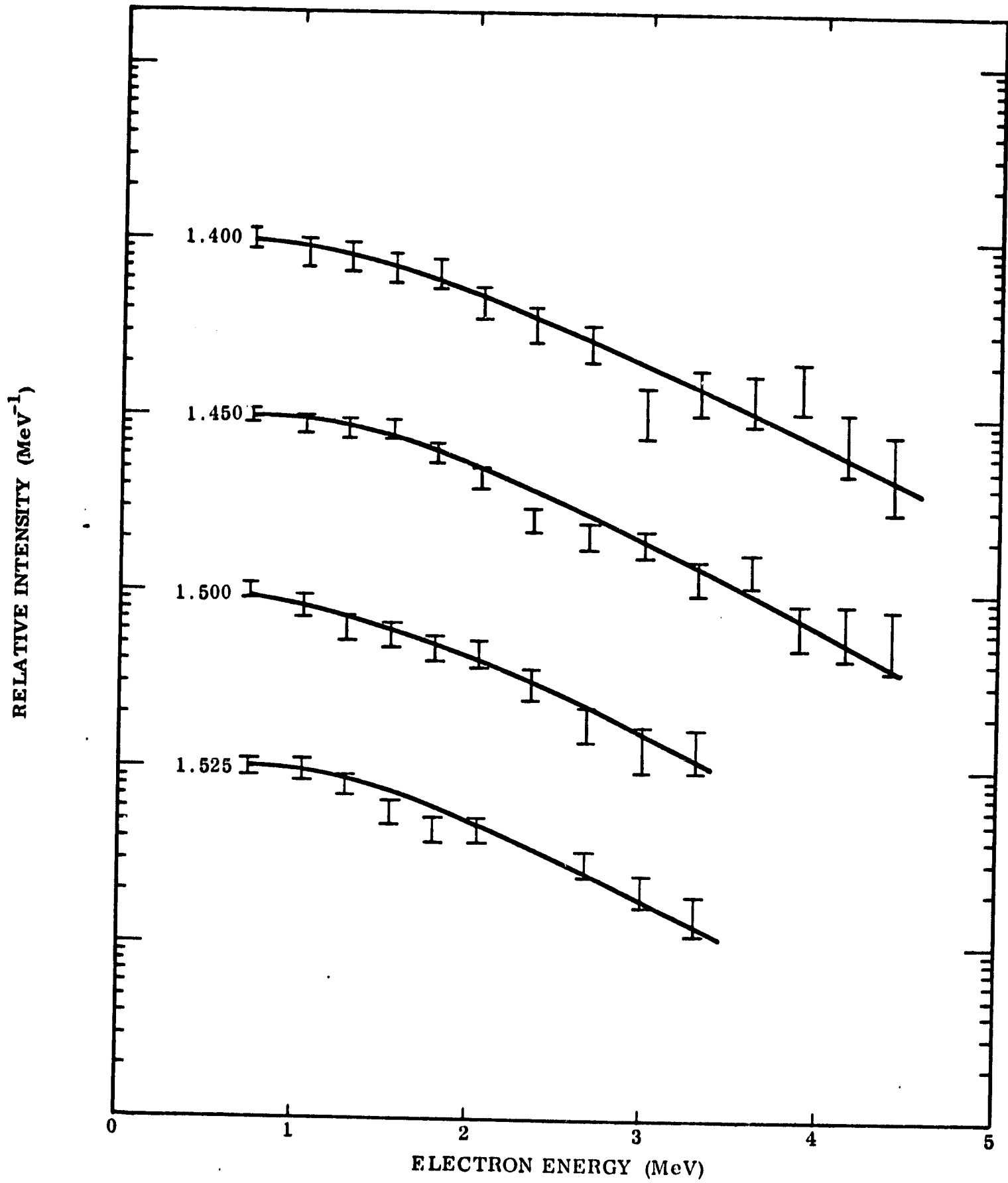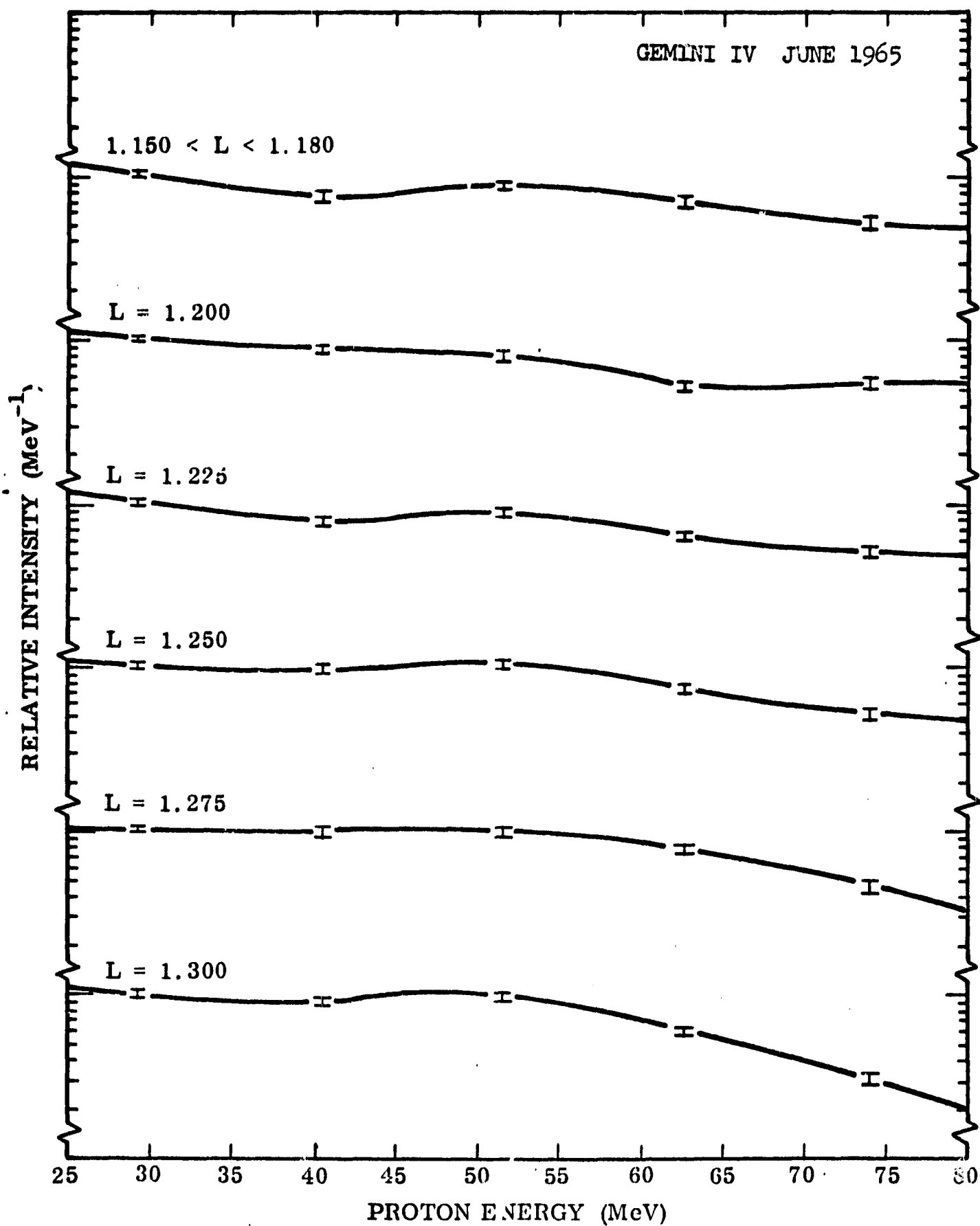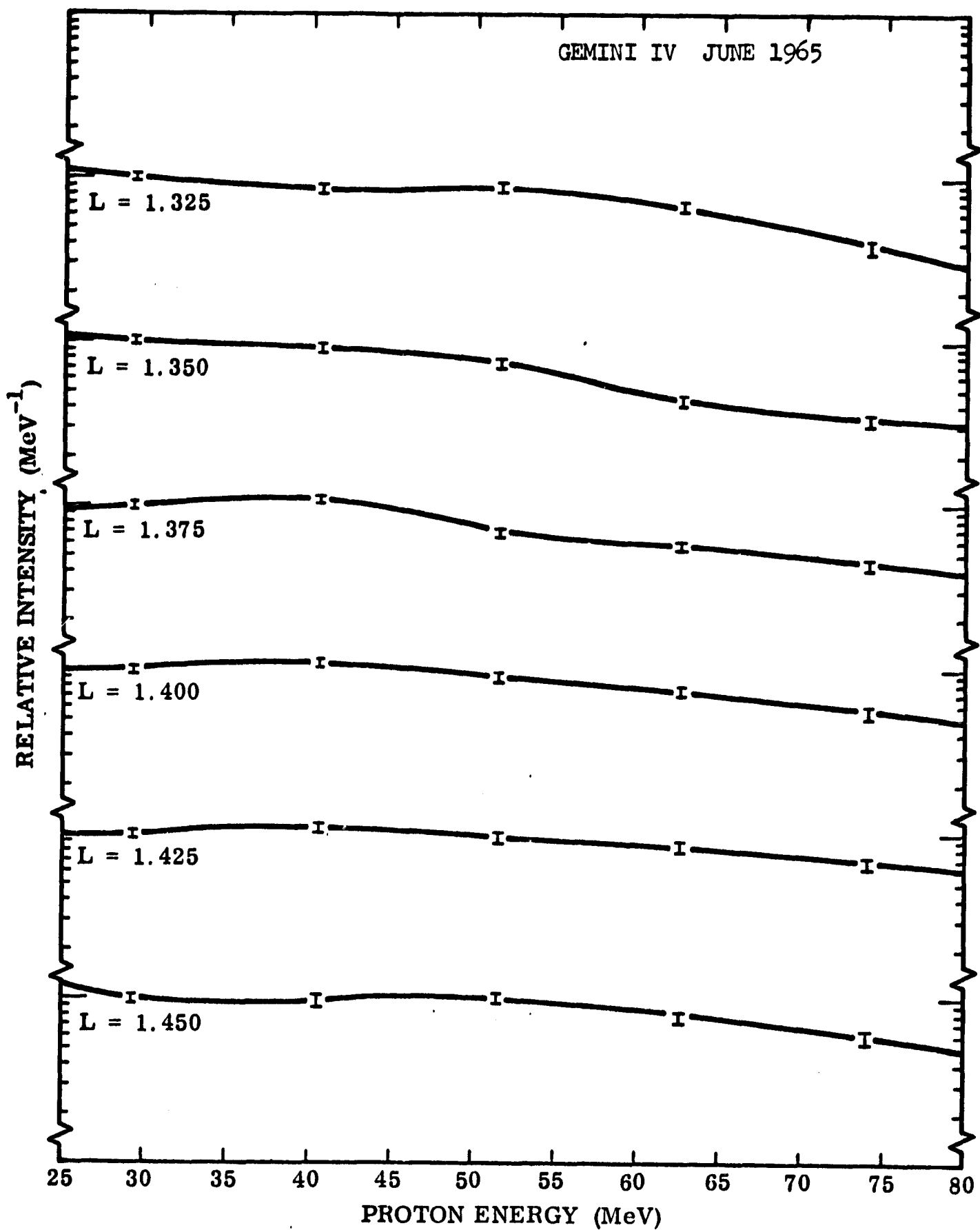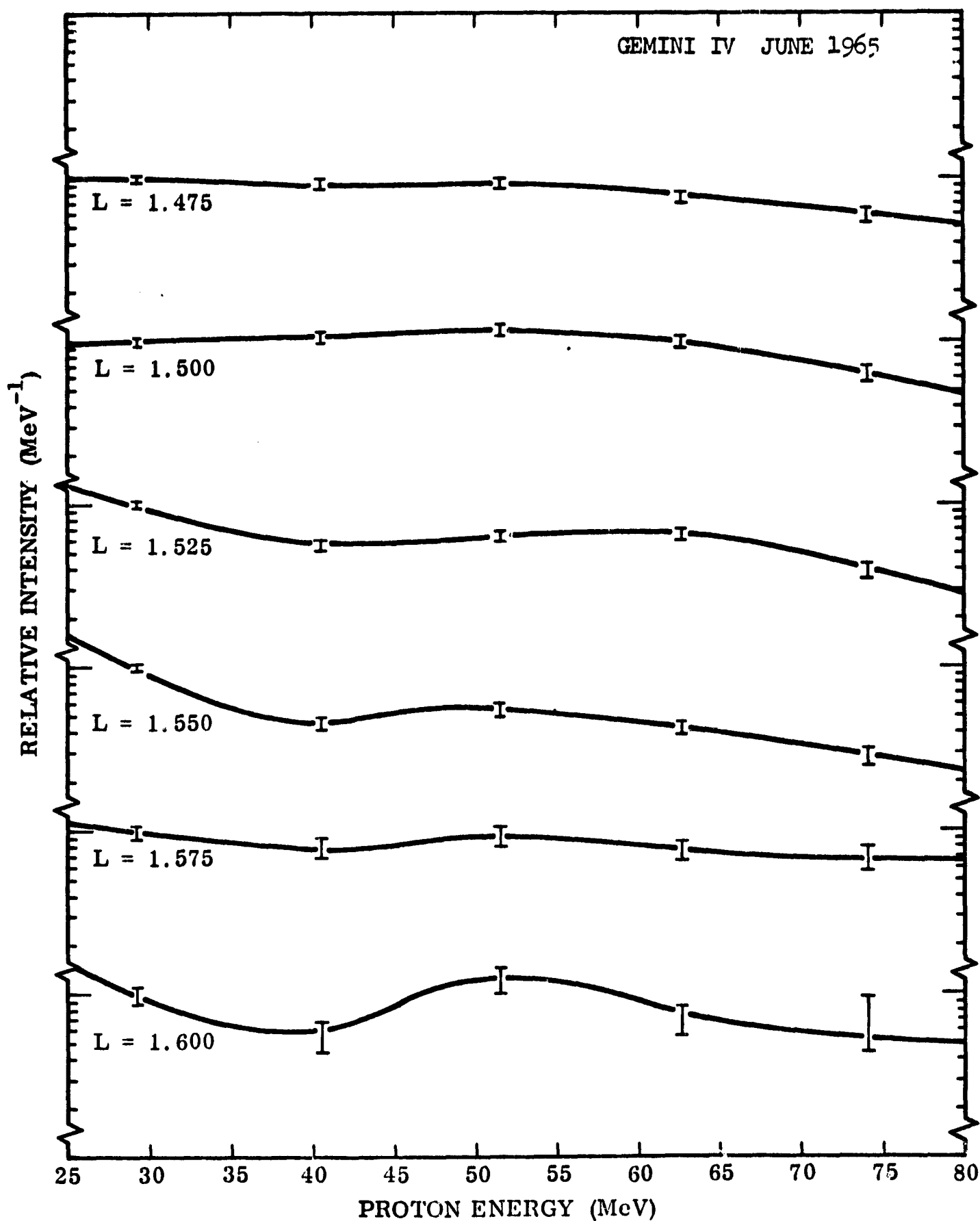
Figure 44 Differential Proton Spectra as a Function of L-Shell in the Interval $1.475 \leq L \leq 1.600$ for the Epoch June 1965.
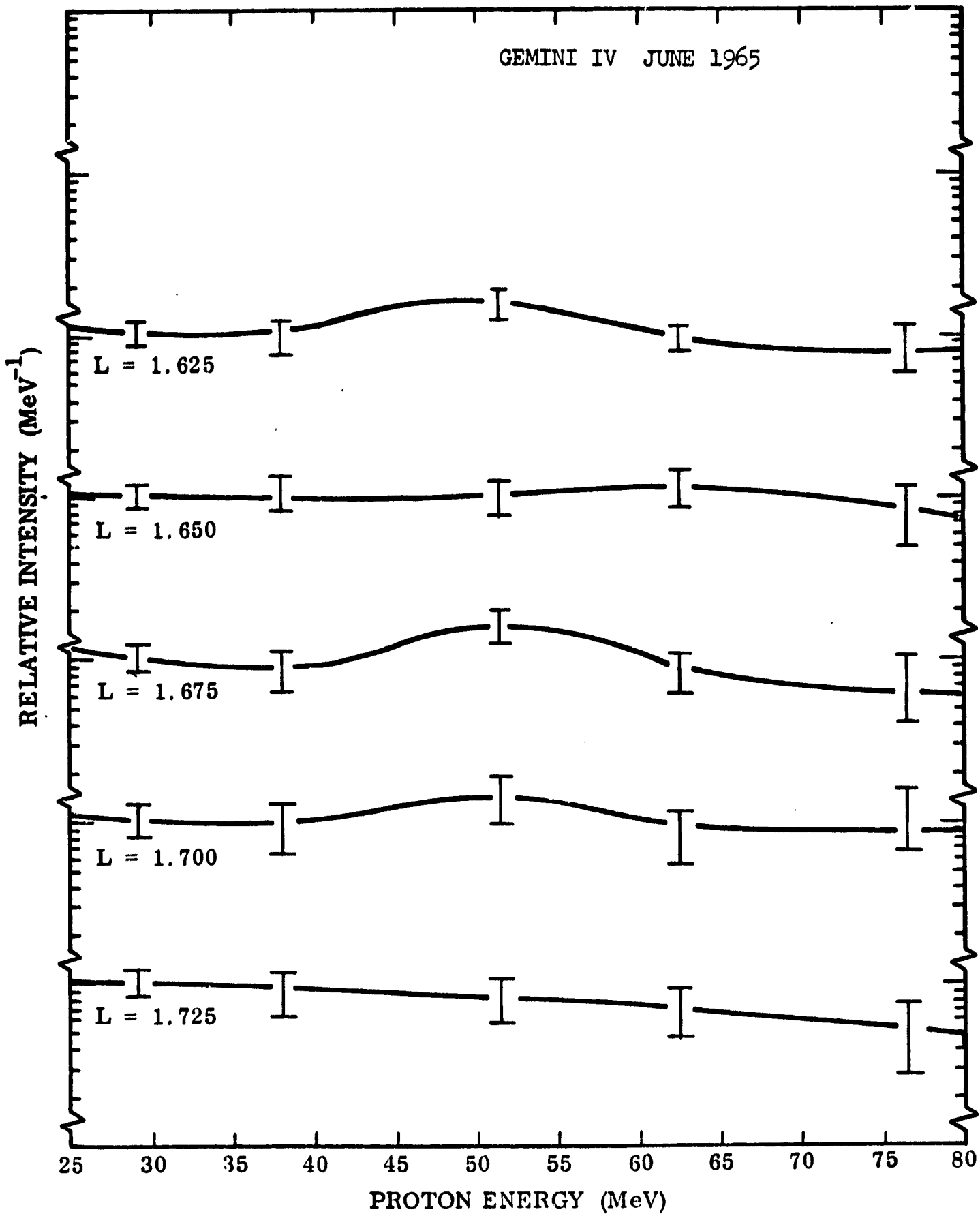
Figure 45   Differential Proton Spectra as a Function of L-Shell in the
Interval $1.625 \le L \le 1.725$ for the Epoch June 1965

Section 6

COMPARISON OF RESULTS

From the measured decay of the Starfish electrons, it has been shown by Walt (1964) that atmospheric scattering is the dominant loss mechanism for electrons trapped on magnetic shells with $L \leq 1.3$. The existence of a dominant loss mechanism which can be calculated to a rather high degree of accuracy has presented the opportunity of learning more about other important loss and/or source mechanisms by making careful comparisons of atmospheric scattering calculations with the measured fluxes and energy spectra. With these objectives in mind, we have analyzed the Gemini electron data in considerable detail at low L values. A summary of these investigations will now be presented.

Due to atmospheric scattering, the fission type electron spectra injected by the Starfish detonation have been calculated to change in shape with time (Walt, 1964). A general depletion in the low energy electrons is predicted to occur, particularly on very low L shells, with a resulting broad peak in the spectrum at energies of about 1 MeV. Comparisons between early measurements and these theoretical spectral shapes, shown in Figure 46, have revealed excellent agreement above about 1.5 MeV but have indicated differences at lower energies (Imhof and Smith, 1965). These differences have been attributed possibly to the presence of naturally injected electrons. Comparisons between the spectra measured on Gemini IV and those calculated by Walt are also shown in Figure 46. Again at high energies the agreement is very good, but below about 1.5 MeV the measured spectra for the Gemini VII data lead to similar conclusions, although the discrepancies at low energies are perhpas less pronounced. Because of our inadequate knowledge of pre-Starfish electrons, it has not been possible to perform quantitative subtraction of the naturally occurring electrons.

As the Starfish electrons continue to decay, it is to be expected that eventually the naturally trapped electrons should begin to dominate, particularly at the lower energies. Convincing evidence for the occurrence of this trend has been reported by Marbach et al. (1968) for measurements in November 1966 at a time of approximately one year after the Gemini VII measurements. Due to differences in the epoch of the measurements and to differences in the threshold
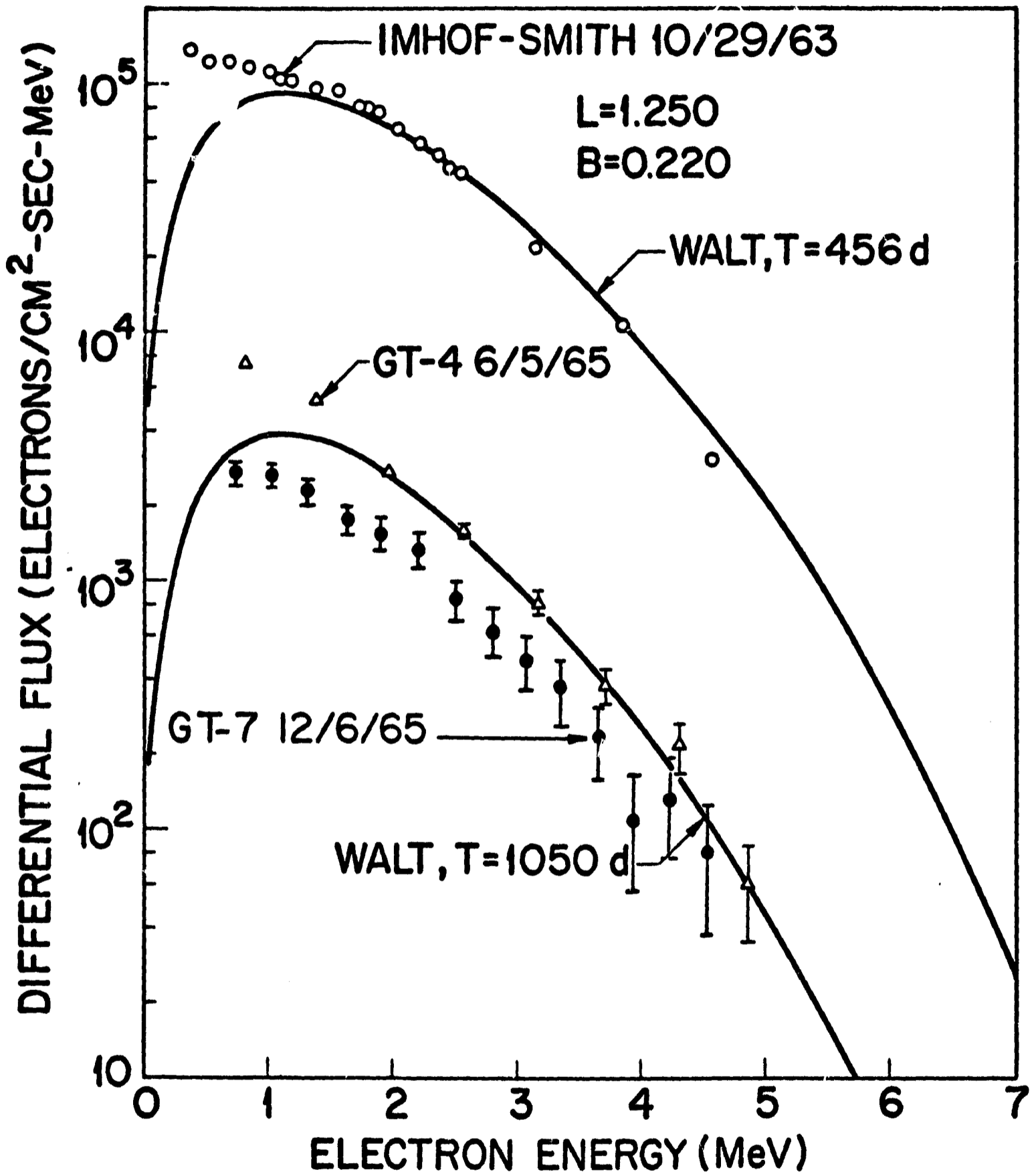
Figure 46 Differential Electron Energy Spectra Measured at Various
Epochs. Also Shown are the Theoretical Spectra Calculated
by Walt for Atmospheric Scattering Effects.

energies, one would expect that the naturally occurring electrons observed by Marbach et al. would have been only weakly visible in the Gemini VII data, provided the natural fluxes were steady in time. Detailed comparisons between the Gemini VII measurements and the Gemini XII measurements of Marbach et al. reveal no significant discrepancies between these two sets of measurements.

When undertaking comparisons between measurements at different epochs, it should be recognized that the naturally occurring electron intensities may well be time dependent. For example, measurements from OGO-1 and OGO-3 by Pfitzer and Winckler (1968) have shown that the September 2, 1966 solar flare injected electrons of energy less than 690 keV to L shells as low as 1.3.

The intensities of electrons measured from Gemini IV and Gemini VII on very low L shells have been examined carefully and compared with atmospheric scattering calculations. The observed omnidirectional electron fluxes at various time periods are plotted in Figure 47 as a function of L. In this presentation all intensities have been normalized to integral fluxes above 0.5 MeV at a value of B = 0.2158 gauss. The best-fit e-folding decay time of the trapped electron fluxes obtained from Figure 47 are shown as a function of L in Figure 48. Although the values are based on measurements performed with different instruments on-board various satellites, the overall decay time errors are estimated to be no greater than a factor of 2, principally because of the long time interval between measurements. Decay time values from other experiments are also included (McIlwain, 1963; Van Allen, 1964; Bostrom and Williams, 1965).

Included in Figure 48 are the theoretical values of Walt (1964) calculated from atmospheric scattering, under the assumption of no additional injections, for the Anderson and Francis (1964) atmospheric model and the Jensen and Cain (1962) expansion of the earth's magnetic field for 1960. The theoretical values deviate significantly from experiment; over long periods of time the characteristic decay times do not decrease with decreasing L value as sharply as expected from atmospheric scattering effects in the absence of any source(s) of new electrons. The theoretical calculations are, of course, dependent upon both the atmospheric and magnetic field models used. At the minimum altitudes of concern here the Harris and Priester (1962) atmospheric model has a higher particle concentration (by about 40%) than the Anderson and Francis atmosphere and would lead to correspondingly shorter lifetimes. However, the effect on the variation of lifetime
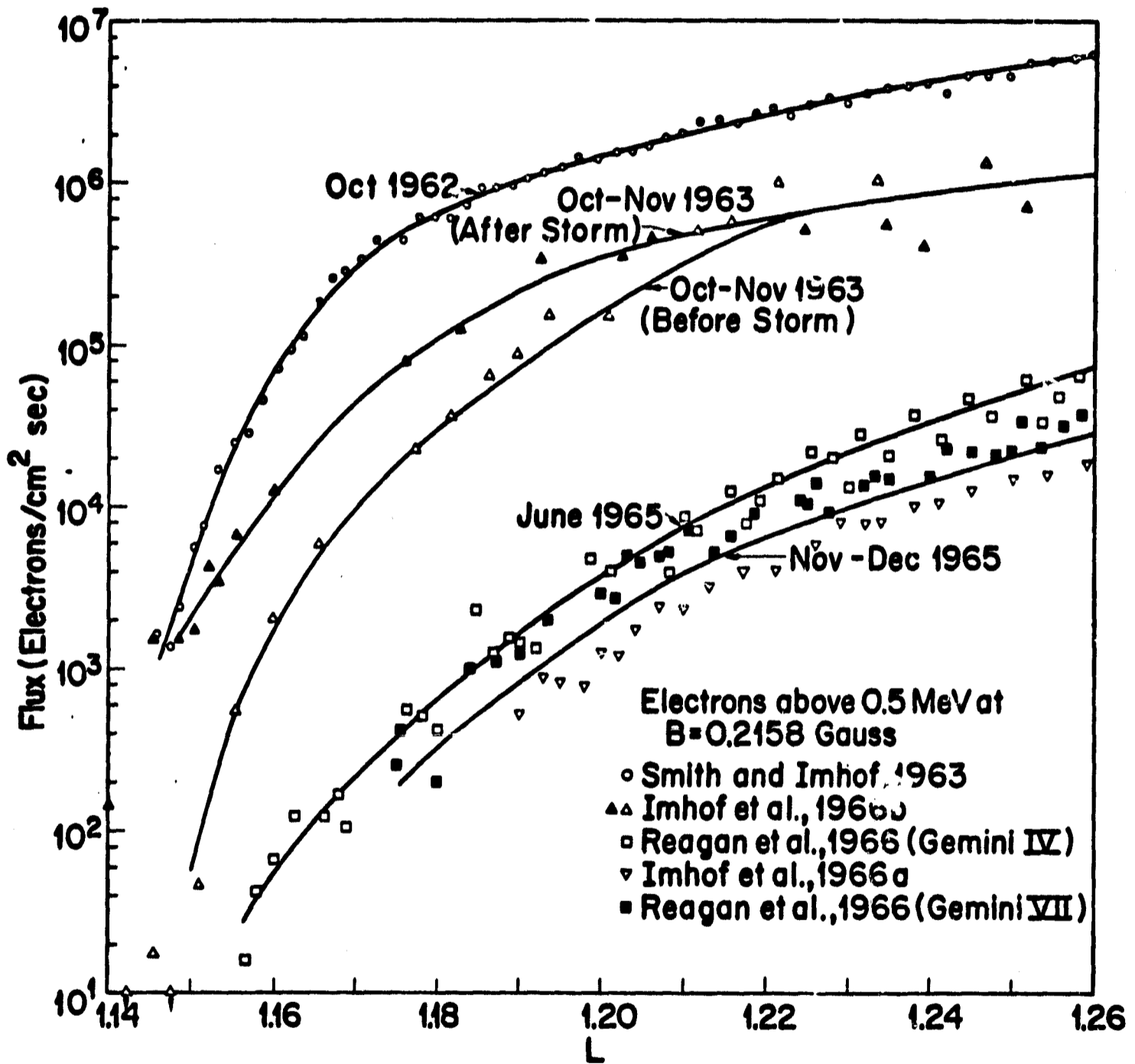
Figure 47. Omnidirectional Electron Fluxes, Plotted as a Function of L, at Various Time Periods.
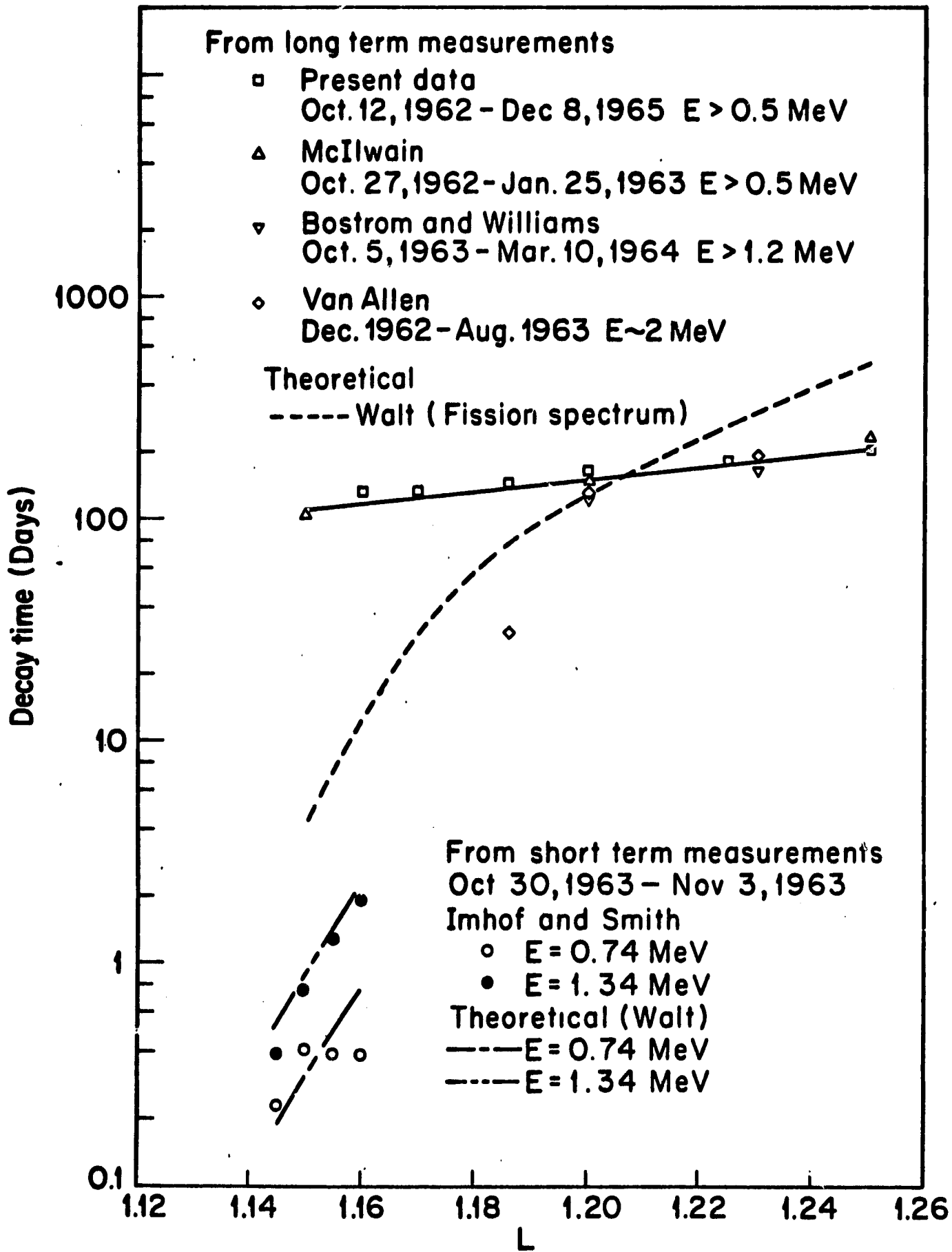
Figure 48. Best-Fit Trapped Electron e-folding Decay Times Over Various Time Periods Plotted as a Function of L.

with L should be appreciably less. Since the same magn·tic field model was used both for processing the data and for the theoretical calculations, it is not felt that large variations in the comparisons between theory and experiment would result from use of a different magnetic field representation.

In contrast to the sharp L-shell dependence calculated from atmospheric scattering effects in the absence of injection, the measured overall decay times are relatively independent of L in this narrow region. Since the atmospheric losses must continue to occur, the apparent decrease in loss rate at low L values indicates that additional electrons are being supplied to these low L shells. In this region of low L values, the trapped electron flux profiles suggest the occurrence of radial diffusion from higher L shells.

Based on the Fokker-Planck diffusion equation, an empirical evaluation of the diffusion coefficient has been obtained by Newkirk and Walt (1968) to account for the observed radial profile and the long-term decay rate of the trapped electron flux. Surprisingly the diffusion coefficient was found to increase with decreasing L, a trend opposite to the known variation of diffusion rates higher in the magnetosphere. This significant finding has led to a greatly increased interest in electron measurements in this region of space. More recently, calculations of the diffusion coefficient have also been performed by T. A. Farley (1968) on the basis of his low L-shell electron observations from OV1-2.

The proton fluxes and spectra measured in the present experiments have been compared with other experimental data and with theoretical predictions on the behavior of trapped protons at low altitudes. Figure 49 shows a comparison of the omnidirectional isoflux contours in B,L space between the Gemini IV data above an energy threshold of 64 MeV and the Injun 3 data (Valerio, 1964) measured over the energy interval 40-110 MeV in the epoch 1962-63. The absolute agreement between the two sets of data is really quite good, considering that the measurements were made over somewhat different energy intervals and at different epochs. The close agreement in absolute intensities indicates that no drastic changes have occurred in the inner belt proton environment at low altitudes over the period 1963-1965.

The differential proton spectra measured with the Gemini IV spectrometer over the energy interval 23.5-80 MeV have been compared with the spectra obtained from nuclear emulsions by Freden and White (1962). Figure 50 shows
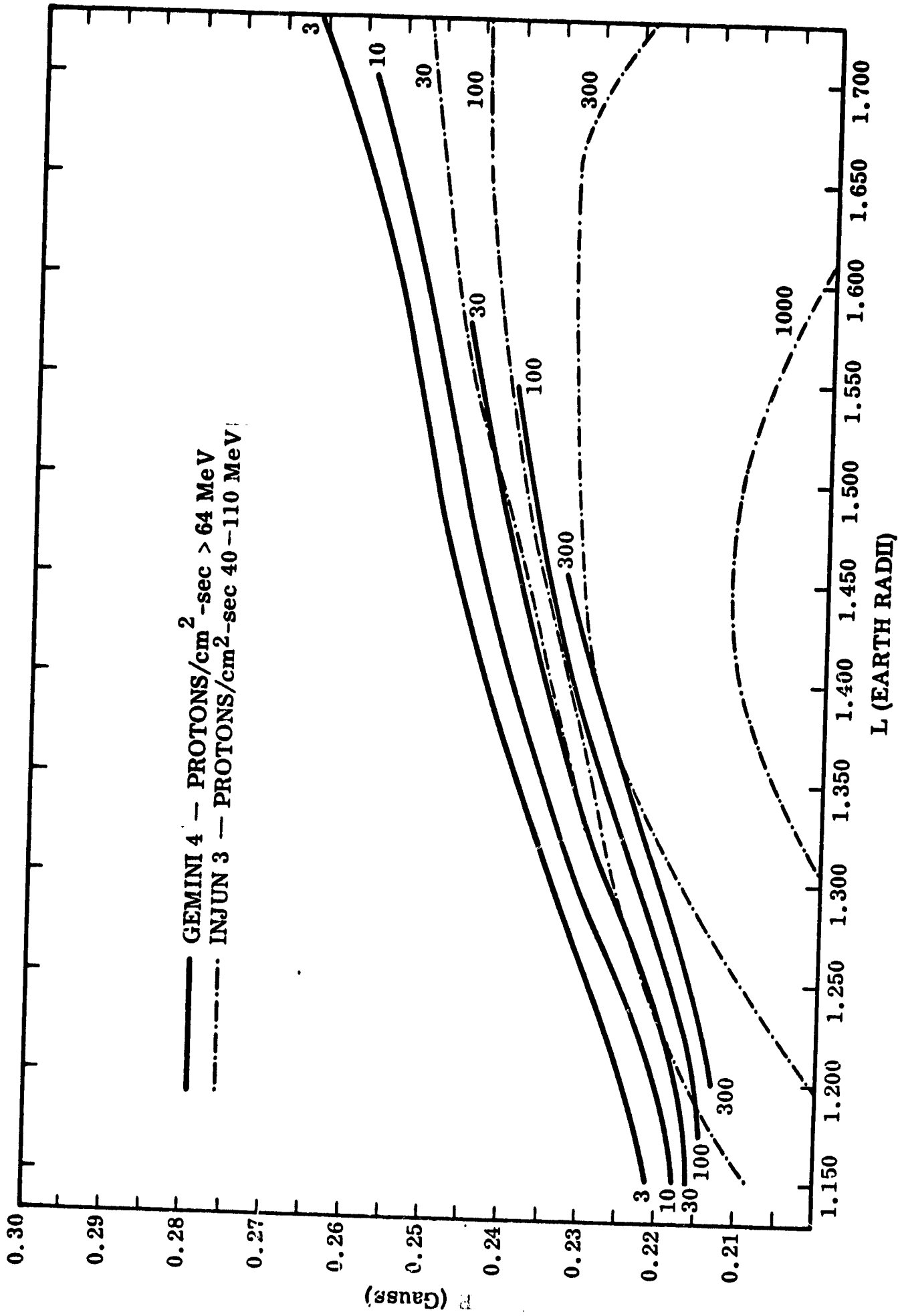
Figure 49 Comparison of the Gemini IV Omnidirectional Isoflux Proton Contours Above 64 MeV with INJUN 3 Data Obtained in the Energy Interval 40-100 MeV.

the comparison at an L-value of 1.40. The data have been arbitrarily normalized
at an energy of approximately 40 MeV. The resulting spectral shapes are in
good agreement. Both sets of data display broad peaks in energy. The Gemini IV
data have the maximum occurring at an energy of approximately 40 MeV while the
emulsion data indicate a peak closer to 30 MeV. As mentioned earlier, the proton
spectra measured in these experiments consistently contain this broad peak but
at somewhat higher energies than other previous data.

An interesting phenomenon associated with trapped protons at low altitudes
was also observed with the Gemini IV spectrometer. At low altitudes, the atmo-
sphere plays a dominant role in the lifetime and behavior of trapped protons.
In the anomaly region, protons trapped on low L-shells are at or very near to
their mirror points and hence have a very narrow pitch angle distribution.
Lenchek and Singer (1962) have predicted that for mirroring protons with gyro-
radii comparable to the atmospheric scale height, and east-west asymmetry in the
trapped flux should be observable. The assumptions in this prediction are that
the atmospheric density varies exponentially with altitude and that the average
atmospheric density encountered over an orbit is equal or proportional to the
average over a circle of gyration at the mirror point.

Direct observations of this asymmetry have been reported by Heckman and
Nakano (1963). They used integrating nuclear emulsions which were carefully
positioned on stabilized, recoverable satellites such that simultaneous tracks
of protons over a narrow-energy interval could be identified as having entered
the detector from either the east or the west with respect to the magnetic field
direction. This east-west asymmetry in the proton flux was also observed with
the Gemini IV spectrometer and since both the flux and spectrum of the protons
involved in the effect were measured, detailed comparisons between the data and
theory can be performed.

On a series of passes through the anomaly region, the spacecraft was
stabilized in flight and flown by astronauts McDivitt and White in either a
small-end forward or blunt-end forward maneuver such that the detector was
oriented in either a true geographic easterly or westerly direction. The
trajectory labeled 22 in Figure 51 indicates a pass where the spacecraft was
passing through the anomaly region such that the detector was facing toward
the east. In contrast, the instrument was facing toward the west on the pass
labeled 52. These two passes were essentially parallel over the entire anomaly
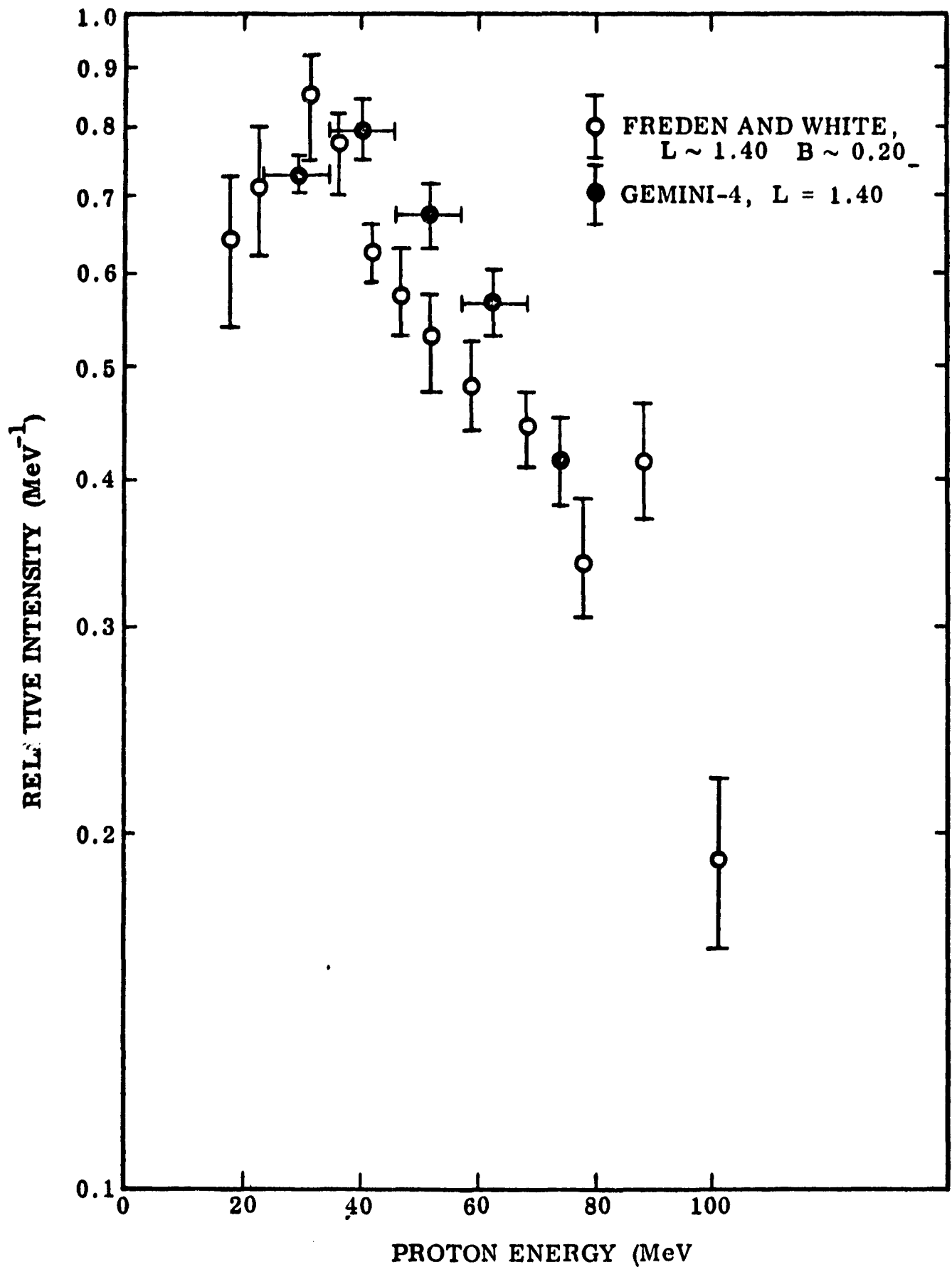
Figure 50   Comparison of the Gemini IV Differential Proton
              Spectra at L = 1.40 with the Emulsion Data of
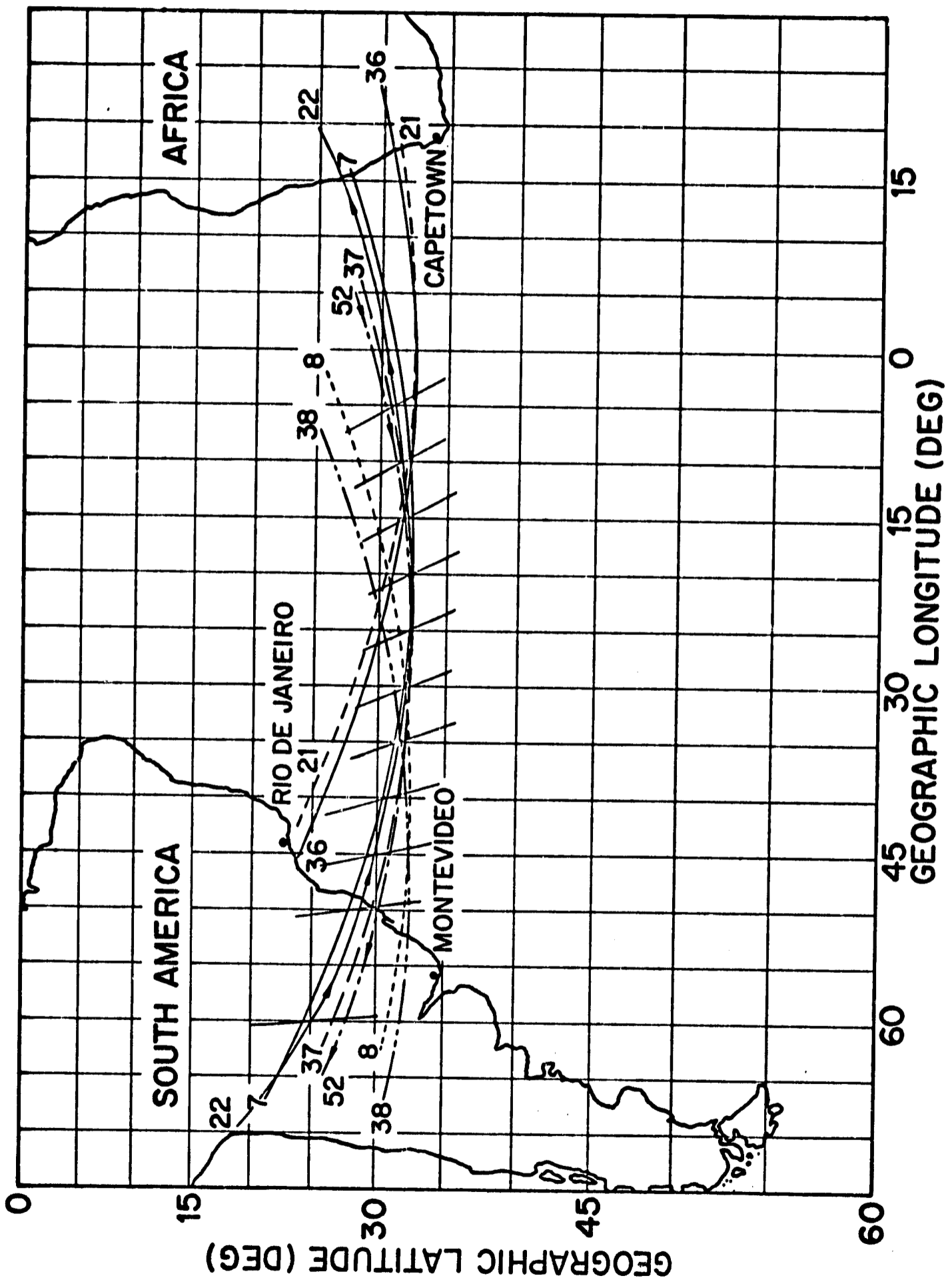   Freden and White.

79

Figure 51   Orbital Paths of the Gemini IV Spacecraft Through the Anomaly Region. On the Pass Labeled 22, the Spectrometer was Facing Toward the East and on Pass 52 was Facing Toward the West.

region. Also shown in the figure are the declinations of the geomagnetic field at positions along the trajectories. The declination in this region varies between a few degrees and a maximum of 30 degrees. It can be seen that the detector was essentially normal to the field direction over the entire region.

The reason for the east-west asymmetry can be seen in Figure 52. This figure shows a model depicting the important parameters involved in this effect. The magnetic meridian is shown with a typical magnetic field line at an inclination of β_{inc} and at a declination of α_{dec} with respect to the earth's surface. Typical inclinations in this region vary between -23 and -58 degrees and declinations between -4 and -30 degrees. Since the trapped protons are at or very near to their mirror altitude, they are confined to the plane shown normal to the magnetic field. Positive particles in the magnetic field move in a westerly direction at the highest point in one gyration and move toward the east at the lowest point in one gyration. This implies that any directional detector will register particles whose center of gyration lies above the detector when it points toward the west and below the detector when it points toward the east. Since the proton flux increases with increasing altitude in this region, a directional detector will therefore observe a higher proton flux when it points west than when it points east. The detector is shown in the figure facing west at an angle θ_Z with respect to the magnetic field and at an angle Φ with respect to the incoming protons in the mirror plane. Protons of a given energy traveling toward the east enter the detector at various angles from all circles of radius a, located above the detector. It should be noted that no such asymmetry was observed in either the directional electron data or in the omnidirectional proton data as obtained from the anticoincidence detector.

We have analyzed our proton data for this asymmetry by comparing the experimental east to west ratio with the predicted ratio obtained from the Lenchek and Singer expression. The equations involved in the calculation of the predicted counting rate in our detector under the assumption previously mentioned are as follows:

$$CR_{predicted} = k \int_{\phi_{min}}^{\phi_{max}} A_{eff} [\Psi(\phi, \theta_Z)] \exp\left(\frac{a}{h} \cos \beta_{incl} \cos \phi\right) d\phi$$

where

$$A_{eff}(\Psi) = \pi r^2 \cos \Psi \left\{ 1 - \frac{2}{\pi} \left[\sin^{-1}(\delta \tan \Psi) + \delta \tan \Psi \sqrt{1 - (\delta \tan \Psi)^2} \right] \right\}$$
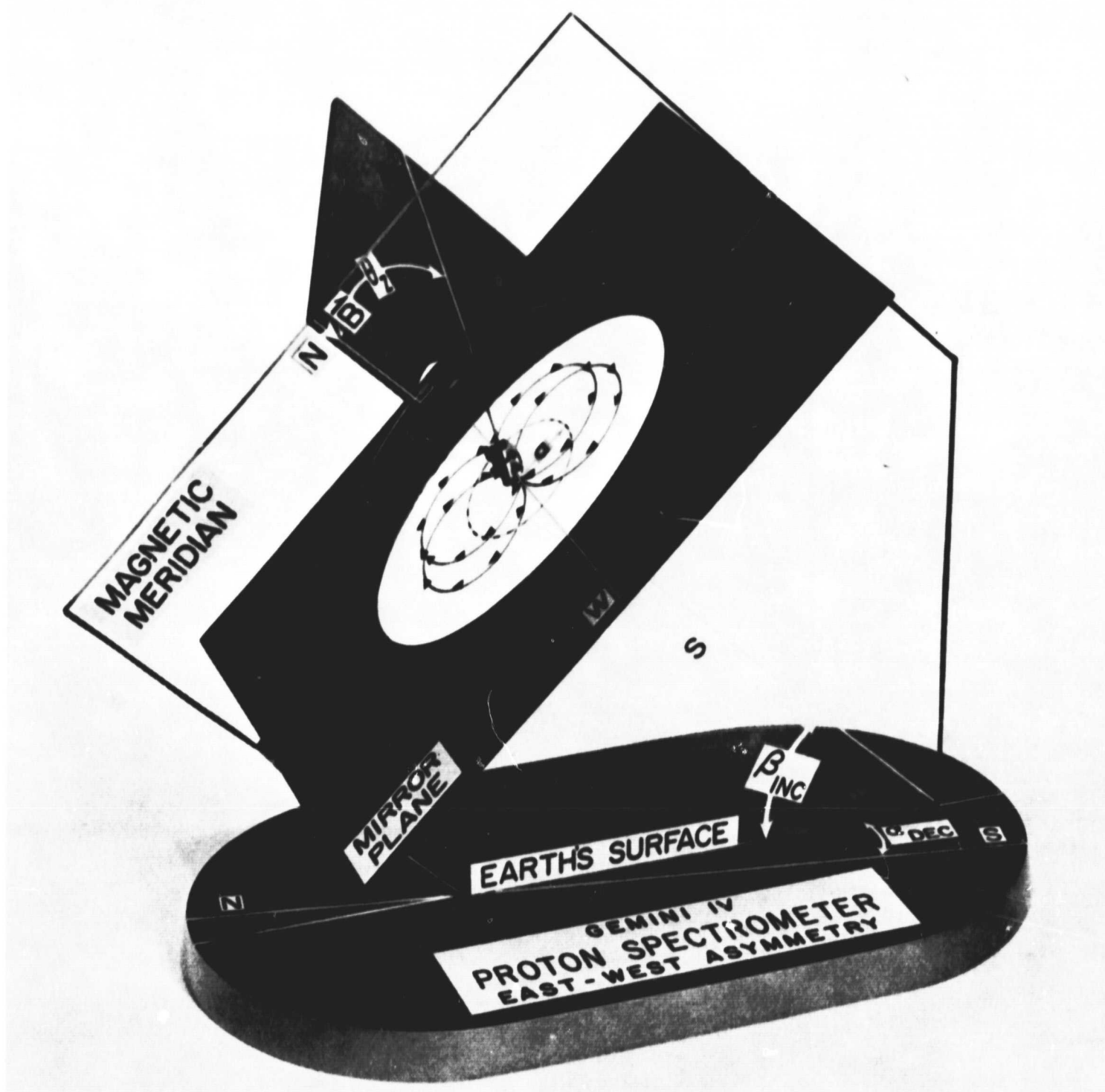
Figure 52 A Model Depicting the Important Parameters Involved in the East-West
Asymmetry of Trapped Protons.

and

$$\cos \Psi = \sin \theta_z \cos \phi$$

a = proton gyroradius (km)

h = neutral atmosphere scale height (km)

β_{inc} = magnetic dip or inclination angle

ϕ = angle within the mirror plane

Ψ = angle between the normal to the detector and the incident flux

θ_z = angle between the normal to the detector and the geomagnetic field vector, $\vec{B}$

r = radius of detector aperture

δ = $d/2r$, where d = detector collimator height

The exponential term under the integral is the Lenchek and Singer expression which inversely relates the unidirectional intensity to the average atmospheric density $\bar{\rho}$ over the particle orbit. In the expression, a is the proton gyroradius, h is the neutral atmosphere scale height, β is the inclination angle of the magnetic field at the point of observation and Φ is the angle within the mirror plane between the plane of the detector and the incoming protons. We have weighted the expression by the effective acceptance area of the detector at each observation point. This effective area, which has been derived for a pancake distribution of particles incident on a cylindrically collimated aperture of radius $\underline{r}$ and height $\underline{d}$, is shown as the second equation. The effective area is a function of ψ, the angle between the normal to the detector and the incident flux. ψ is a function of both θ_z, which is the angle between the normal to the detector and the geomagnetic field, and Φ. The three angles are related by the third equation Cos ψ = sin θ_z Cos Φ. The value of θ_z was obtained directly from magnetometer data. The integral is taken over the limits of the angular acceptance of the detector Φ_{min} to Φ_{max}. The constant $\underline{k}$ in front of the integral normalizes the expression to a unit flux. The predicted counting rates were obtained then by calculating this integral at data points taken every 0.8 second along both the eastbound and westbound passes. The inclination and declination angles at each observation point were obtained from the Jensen and Cain 48-term expansion of the geomagnetic field. The value of the atmospheric scale height corresponding to the minimum altitude of each observation point was obtained from the model atmosphere of Anderson and Francis (1964). The values for the

83

average diurnal scale height for the solar minimum period were used. The predicted ratio of the eastward bound flux to the westward bound flux was then compared with the actual experimental ratio.

Since both of these passes were essentially parallel to each other, it was necessary to normalize the data in B prior to obtaining an experimental ratio for any given L shell. This was accomplished by using the data shown earlier. The results of these calculations are shown in Figure 53. In the bottom two plots, we are comparing the experimentally obtained ratio of the east-to-west proton flux as a function of L in the two proton energy intervals E_p 23.5 - 46.5 MeV and E_p = 46.5-67.5 MeV to the calculated ratio obtained from the Lenchek and Singer predictions. We have also plotted the minimum altitudes corresponding to each data point. It can be seen that the data covered a minimum altitude span of 150-280 km. The scale height as obtained from the Anderson and Francis model atmosphere is also plotted as a function of L in the upper curve. It can be seen that in this minimum altitude regime, the average scale heights vary from 25 to 50 km. The agreement between the experimental ratios and the predicted ratios is only fair.

In the higher-energy group, the discrepancy is approximately 50 percent while in the lower energy group the discrepancy is as much as a factor of 2. The rather smooth discrepancy displayed in the higher energy group might be partially explained by uncertainties in the atmospheric model at these altitudes, but the discrepancies in the lower energy group require further examination. Comparisons of the proton observations with atmospheric scale heights at the minimum altitude positions can be expected to be only approximate since the comparisons should ideally be made with the atmosphere averaged over the proton trajectories. The experimental ratios can also be determined from the omnidirectional data itself. We have calculated the east-west flux ratios that would be obtained from the flux profiles presented earlier by taking the ratio of the flux measured at a distance a, equal to the gyroradius, above and below the observation point along a given inclination. The results of this calculation are in agreement with results presented in this figure.

The stability of the flux contours in this region of space and the general dominance of atmospheric loss mechanisms offer a unique opportunity to learn more about the proton source mechanism from observations at low altitudes. Measurements performed here, where the atmospheric loss rates change very rapidly
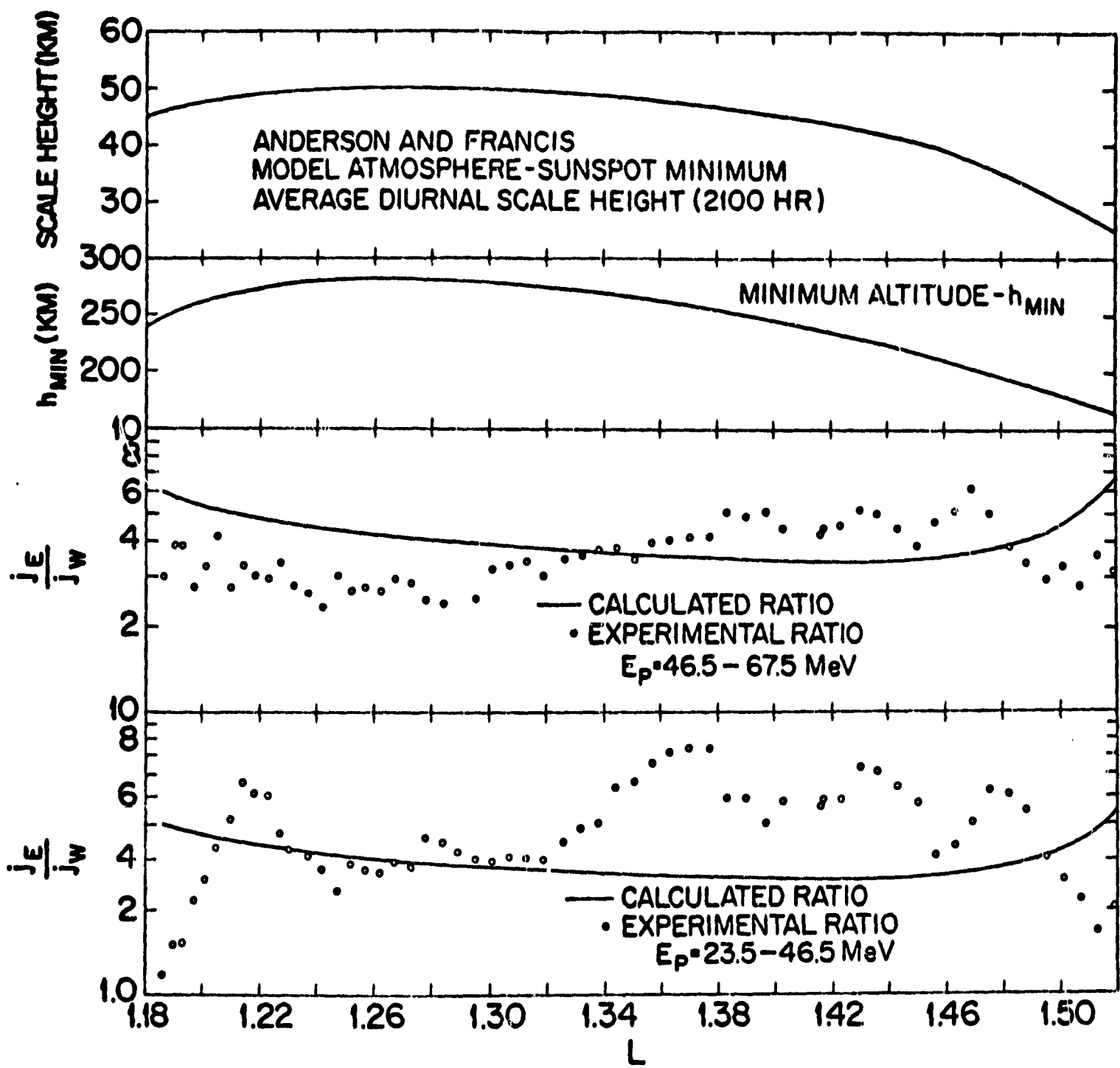
Figure 53   Comparison of the Measured East-West Asymmetry in the Trapped
            Proton Flux at Low-Altitudes with Theoretical Predictions.
            The Atmospheric Scale Heights and Minimum Altitudes Associated
            with the Data are Also Shown.

with position, are ideal for intercomparison of the importance of the cosmic ray albedo neutron decay injection mechanism, which occurs at a nearly uniform rate throughout, with the significance of other injection processes which may show considerably different spatial profiles.

Section 7

CONCLUSIONS

The omnidirectional fluxes and spectra of electrons and protons at low altitudes in the inner radiation belt have been measured in detail for the epochs June and December 1965. These data should prove valuable in updating existing models of the earth's radiation environment and therefore will be submitted to the National Data Center at NASA/GSFC.

The data obtained from these experiments on the decay of the artificial electron belt have been compared with earlier experimental data and with theoretical predictions which are based on atmospheric scattering being the dominant loss mechanism. The present data have conclusively demonstrated that in this low altitude region other mechanisms such as L-shell radial diffusion are also important.

An interesting and important phenomenon associated with protons trapped at low altitudes has also been measured in the present experiments. The existence of an east-west asymmetry in the trapped protons means that any directional detector in this region will observe a higher proton flux when it points west than when it points east. Factors of two to eight difference in flux are possible depending on the position and orientation of the detector. Since many detectors utilized in space physics experiments are directional in type, this asymmetry may be responsible for some of the rather large discrepancies which exist in the experimental proton data in this region. It should be emphasized that the proton flux contours presented in this report were obtained when the detector was oriented essentially in an easterly direction.

The stability of the proton flux in this region of space and the general dominance of atmospheric loss mechanisms offer a unique opportunity to learn more about the proton source mechanism by comparing the present data with the atmosphere in greater detail than has been possible in this report.

REFERENCES

Anderson, A. D. and W. E. Francis, "A Semi-Theoretical Model for Atmospheric Properties from 90 to 10,000 km," Lockheed Missiles & Space Company, Report No. 6-74-64-19, 1964.

Beall, D. S., C. O. Bostrom and D. J. Williams, "Structure and Decay of the Starfish Radiation Belt, October 1963 to December 1965, J. Geophys. Res. 72, 3403, 1967.

Blanchard, R. C. and W. H. Heaa, "Solar Cycle Changes in Inner-Zone Protons," J. Geophys. Res. 69, 3927, 1964.

Bostrom, C. O. and D. J. Williams, "Time Decay of the Artificial Radiation Belt," J. Geophys. Res. 70, 240, 1965.

Chapman, M. C. and T. A. Farley, "Absolute Electron Fluxes and Energies in the Inner Radiation Zone in 1965," J. Geophys. Res. 73, 6825, 1968.

Evans, H. C. and E. H. Bellamy, "The Response of Plastic Scintillators to Protons," Phys. Soc. Proc. 74, 483, 1959.

Farley, T. A., "Radial Diffusion of Artificial Belt Electrons," Trans. Am. Geophys. Union 49, 719, 1968.

Freden, S. C. and R. S. White, "Trapped Proton and Cosmic-Ray Albedo Neutron Fluxes," J. Geophys. Res. 67(1), 25-29, 1962.

Freden, S. C. and G. A. Paulikas, "Trapped Protons at Low Altitudes in the South Atlantic Magnetic Anomaly," J. Geophys. Res. 69, 1257, 1964.

Gooding, T. J. and H. G. Pugh, "The Response of Plastic Scintillators to High-Energy Particles," Nucl. Instr. and Methods 7, 189, 1960.

Harris, I. and W. Priester, "Theoretical Model for the Solar Cycle Variation of the Upper Atmosphere," Goddard Space Flight Center, NASA, Report X-640-62-70, 1962.

Heckman, H. H. and G. H. Nakano, "East-West Asymmetry in the Flux of Mirroring Geomagnetically Trapped Protons," J. Geophys. Res. 68, 2117, 1963.

Hendricks, S. J. and J. C. Cain, "Magnetic Field Data for Trapped-Particle Evaluation," J. Geophys. Res. 71, 346, 1966.

Imhof, W. L., R. V. Smith and P. C. Fisher, "Particle Flux Measurements from an Atlas Pod in the Lower Van Allen Belt," Space Res. III, 438, 1963.

Imhof, W. L. and R. V. Smith, "Variation of Electron Spectrum and Intensity at Low Altitudes," Space Res. V, 360, 1965a.

Imhof, W. L and R. V. Smith, "Longitudinal Variations of High Energy Electrons at Low Altitudes," J. Geophys. Res. 70, 569, 1965b.

Imhof, W. L. and R. V. Smith, "Energy Spectrum of Electrons at Low Altitudes," J. Geophys. Res. 70, 2129, 1965c.

Imhof, W. L. and R. V. Smith, "Observation of Nearly Monoenergetic High-Energy Electrons in the Inner Radiation Belt," Phys. Rev. Letters 14, 885, 1965c.

REFERENCES - continued

Imhof, W. L., J. C. Bakke, E. E. Gaines, J. H. Rowland and R. V. Smith, "High Resolution Electron Measurements in the Outer Radiation Belt," _Trans. Am. Geophys. U._ 47, 135, 1966.

Jensen, D. C. and J. C. Cain, "An Interim Geomagnetic Field," _J. Geophys. Res._ 67, 3568, 1962.

Lenchek, A. M. and S. F. Singer, "Effects of the Finite Gyroradii of Geomagnetically Trapped Protons," _J. Geophys. Res._ 67, 4073, 1962.

Lenchek, A. M. and S. F. Singer, "The Albedo Neutron Theory of Geomagnetically Trapped Protons," _Planet. Space. Sci._ 11, 1151, 1963.

Lin, W. C., D. Venkatesan and J. A. Van Allen, "Latitude Survey of Cosmic-Ray Intensities by Explorer 7, October 1959 to February 1961," _J. Geophys. Res._ 68, 4885, 1963.

Lindstrom, P. J. and H. H. Heckman, "B-L Space and Geomagnetic Field Models," _J. Geophys. Res._ 73, 3441, 1968.

Mann, L. G., S. D. Bloom and H. I. West, Jr., "The Electron Spectrum from 90 to 1200 keV as Observed on Discoverer Satellites 29 and 31," Space Res. III, 447, 1963.

Marbach, J. R., C. S. Warren and R. S. Lindsey, "Evidence of Nonfission Electrons in the South Atlantic Anomaly," _J. Geophys. Res._ 73, 3477, 1968.

McIlwain, C. E., "Coordinates for Mapping the Distribution of Magnetically Trapped Particles," _J. Geophys. Res._ 66, 3681, 1961.

McIlwain, C. E., "The Radiation Belts, Natural and Artificial," _Science_ 142, 355-361, 1963.

Mozer, F. S., D. D. Elliott, J. D. Mihalov, G. A. Paulikas, A. L. Vampola and S. C. Freden, "Preliminary Analysis of the Fluxes and Spectrums of Trapped Particles after the Nuclear Test of July 9, 1962," _J. Geophys. Res._ 68, 641, 1963.

Nelms, A. T., "Energy Loss and Range of Electrons and Positrons," National Bureau of Standards Circular 577, July 1956.

Newkirk, L. L. and M. Walt, "Radial Diffusion Corfficient for Electrons at Low L Values," _J. Geophys. Res._ 73, 1013, 1968.

Paulikas, G. A. and S. C. Freden, "Precipitation of Energetic Electrons into the Atmosphere," _J. Geophys. Res._ 69, 1239, 1964.

Pfitzer, K. A. and J. R. Winckler, "The Decay and Injection of Artificial and Natural Electrons in the Inner Zone," _Trans. Am. Geophys. U._ 49, 233, 1968.

Reagan, J. B., J. C. Bakke, W. L. Imhof and R. V. Smith, "Multichannel Spectrometer for the Measurement of Trapped Particles," _IEEE Trans._ NS-12, 83, 1965.

Reagan, J. B., "Proton-Electron Spectrometer Experiments on Gemini-4 and Gemini-7 (Final Report - Contract NAS 9-1587), Lockheed Missiles & Space Company, Report No. 2-44-66-1, 1966a.

Reagan, J. B., J. C. Bakke, M. A. Heinemann, W. L. Imhof and R. V. Smith, "Measurements of Trapped Particle Fluxes and Spectra at Low Altitudes from Gemini IV," _Trans. Am. Geophys. U._ 47, 130, 1966b.

REFERENCES - continued

Rich, M. and R. Madey, "Range-Energy Tables," University of California Radiation Laboratory Report 2301, March, 1954.

Rowland, J. H., J. C. Bakke, W. L. Imhof and R. V. Smith, "Instrumentation for Space Radiation Measurements," IEEE Trans. NS-10, 178, 1963.

Valerio, J., "Protons from 40 to 100 MeV Observed on Injun 3," J. Geophys. Res. 69, 4949, 1964.

Van Allen, J. A., "Lifetimes of Geomagnetically Trapped Electrons of Several MeV Energy," Nature 203, 1006, 1964.

Vernov, S. N., V. E. Nesterov, N. F. Pisarenko, I. A. Savenko, O. I. Savun, P. I. Shavrin and K. N. Sharvina, "Investigation of the Earth's Radiation Belts in the Vicinity of the Brazilian Magnetic Anomaly at Altitudes of 235-345 km," Planet. Space Sci. 13, 347, 1965.

Vette, J. I., "Models of the Trapped Radiation Environment. Vol. I: Inner Zone Protons and Electrons," NASA SP-3024, 1966. "Vol. II: Inner and Outer Zone Electrons," NASA SP-3024, 1966.

Walt, M. and W. M. MacDonald, "The Influence of the Earth's Atmosphere on Geomagnetically Trapped Particles," Rev. Geophys. 2, 543, 1964a.

Walt, M., "The Effects of Atmospheric Collisions on Geomagnetically-Trapped Electrons," J. Geophys. Res. 69, 3947, 1964b.

Welch, J. A., Jr., R. L. Kaufman and W. H. Hess, "Trapped Electron Time History for L = 1.18 to L = 1.30," J. Geophys. Res. 68, 685, 1963.

West, H. I., Jr., L. G. Mann and S. D. Bloom, "Some Electron Spectra in the Radiation Belts in the Fall of 1962," Space Res. V, 423, 1965.